
Transmission properties of the KATRIN main spectrometer (when operated) for a keV-scale sterile neutrino search

MASTER THESIS

Nuclear-, Particle- and Astrophysics

Pia Voigt

Physik-Department E47 - Dark Matter

Technische Universität München

Reviewer:	Prof. Dr. Susanne Mertens
Second Reviewer:	Prof. Dr. Stefan Schönert
Advisor:	Dr. Anthony O'Neill

München, 27. September 2023

Declaration of Authorship

Hereby, I declare that the submitted thesis

TRANSMISSION PROPERTIES OF THE KATRIN MAIN SPECTROMETER (WHEN OPERATED) FOR
A KEV-SCALE STERILE NEUTRINO SEARCH

is my independent work. All sources that I have used are explicitly indicated and are stated completely.

Munich, 18.07.2023

Pia Voigt

Introduction

Considering the standard cosmological Lambda-CDM (Lambda Cold Dark Matter) model, recent results from the Planck satellite show that the mass content of the present Universe consists besides of 15.65% ordinary matter also of 84.35% dark matter [1]. The ordinary matter includes all particles resembled in the Standard Model of Particle Physics (SM), while the nature of the dark matter is unknown so far. The undebated presence of dark matter is verified with experiments on all scales. Ranging from astrophysical and cosmological observation of the redshift of the 21cm hydrogen line, galaxy rotation curves, the cosmic microwave background and the early structure formation. The name 'dark' was given due to the fact, that this additional matter does not interact with any of the fundamental forces, such as the strong and weak or electromagnetic interaction but only via gravity. Important parameters such as its identity and production mechanism are still unknown and strongly depend on the assumed cosmological model. Many theoretical hypothesis assume a new particle. Extending the SM by a sterile neutrino in the keV-mass range is well motivated and would provide a viable dark matter candidate. The right-handed sterile neutrino would introduce new mass eigenstates and could in principle possess an arbitrary mass. Hence, the sterile neutrinos only interact gravitationally or via the active-sterile mixing with the known active SM neutrinos. Although cosmological observations have shown that the mixing amplitude is exiguous, $\sin^2 \theta < 10^{-7}$, the properties of a dark matter sterile neutrino can be accessed in a laboratory environment by exploiting the kinematics of the β -decay of e.g. tritium.

Currently, the renowned **K**arsruhe **T**ritium **N**eutrino (KATRIN) experiment is designed to determine, neutrino mass model independently, the absolute electron anti-neutrino mass with an unprecedented sensitivity of 0.2 eV at 90% confidence level. Via high-precision spectroscopy, where the applied retarding potential in the main spectrometer acts as a high-pass filter, the integrated electron energy spectrum of the molecular tritium β -decay is measured very close to the kinematic endpoint of $E_0 = 18.575$ keV, where the imprint of the electron anti-neutrino mass is the most prominent. The effective neutrino mass leads to a reduction of the maximum available kinetic energy of the β -electron and to a slight distortion of the spectral shape at $E_0 - m_{\bar{\nu}_e}$.

After the determination of KATRIN, the setup can be modified in order to extend the measured energy region. With the same approach as for the neutrino mass, the decay into a keV-scale sterile neutrino leads to a superposition of the spectra and produces a kink-like structure at

Introduction

$E_0 - m_{\nu_s}$. By lowering the retarding potential in the main spectrometer one is able to look deeper into the spectrum. However, this also bears technical challenges. In order to handle the exceedingly higher rates of up to 10^8 electrons per second a new detector and read-out system are essential. The novel Silicon Drift Detector (SDD) for **T**ritium **I**nvestigation on **S**terile (**A**) **N**eutrinos (TRISTAN), which is currently under development, consists of more than 1000 pixels and can not only handle such high rates but also provides an excellent energy resolution of 300 eV (FWHM) at 20 keV. In addition to higher rates and systematic effects, electrons with a high surplus energy will enter the main spectrometer. This can lead to an unfavorable transmission loss due to chaotic non-adiabatic electron motion. The focus of this thesis is the study of these non-adiabatic effects with the Monte Carlo simulation software KASSIOPEIA. Further, possible solutions how the magnetic field setting of the experiment can be optimized, such that the adiabatic transmission conditions are fulfilled at a sufficient level, are presented.

This thesis is structured as follows: Chapter 1 gives a brief introduction into the key aspects of neutrino physics. Chapter 2 describes the working principle and setup of the KATRIN experiment. The extension of the KATRIN experiment, the TRISTAN project, is outlined in Chapter 3. The subject of this thesis is the investigation of the optimum magnetic field setting, ensuring adiabatic electron transmission with the help of the KASSIOPEIA simulation framework, which structure is explained in Chapter 4. The basic principles and simulation results of the transmission study are shown and discussed in Chapter 5. Furthermore, a measurement with condensed krypton ($^{83\text{m}}\text{Kr}$) was performed, in order to study the non-adiabatic effect on the electron transmission with the current KATRIN setup. The measurement results are shown in Chapter 6. Finally, the krypton measurement was also simulated with KASSIOPEIA and the simulation results as well as the comparison to the measured data are presented in Chapter 6.

Contents

1. Neutrino Physics	1
1.1. Standard Model of Particle Physics	1
1.2. Postulation and Discovery of the Neutrino	3
1.3. Number of Active Neutrino Flavors	5
1.3.1. Z0-Resonance	5
1.3.2. Neutrino-to-Photon Ratio	6
1.4. Neutrino Flavor Oscillation	7
1.4.1. Solar Neutrino Problem	7
1.4.2. Theoretical description	9
1.4.3. Experimental Determination of the Oscillation Parameters	10
1.5. Neutrino Mass	11
1.5.1. See-Saw Mechanism	12
1.5.2. Determination of Neutrino Mass	13
1.6. Sterile Neutrinos	15
2. The KATRIN Experiment	19
2.1. Experimental Setup	20
2.1.1. Source Section	21
2.1.2. Transport Section	22
2.1.3. Spectrometer Section	22
2.1.4. Detector Section	27
2.2. Neutrino Mass Measurement	28
2.3. keV Sterile Neutrino Search	29
3. The TRISTAN Project	31
3.1. Silicon Drift Detectors	33
3.2. TRISTAN Detector	34
4. KASSIOPEIA	37
4.1. Geometry	37
4.2. Electromagnetic Fields	37
4.3. Generation	39
4.4. Propagation	39

Contents

4.5. General Structure	40
5. Transmission Study	43
5.1. Adiabatic Electron Transport	48
5.2. Simulation Setting	50
5.2.1. Generation	52
5.2.2. Terminators	54
5.2.3. Zonal Harmonic Solver	57
5.2.4. Decreased Detector Magnetic Field	61
5.2.5. Increased Main Spectrometer Magnetic Field	64
5.3. Results	67
5.3.1. Reference KATRIN Setting	67
5.3.2. Decreased Detector Magnetic Field	70
5.3.3. Increased Main Spectrometer Magnetic Field	73
5.4. Conclusion	78
6. Condensed 83m-Kr Measurement & Simulation	81
6.1. Condensed 83m-Kr Source	81
6.2. Measurement	84
6.3. Pile Up Estimation	92
6.3.1. Correction Formula	93
6.3.2. 2D Pile-Up Map	93
6.3.3. Monte Carlo Estimation	95
6.4. Simulation with KASSIOPEIA	99
A. Appendix	103
A.1. Total Transmission Probability	103
A.2. Slow Control Parameters	104
A.3. Polar Angle Correction - Cut Functions	106
A.4. Run Numbers - CKrS Measurement	107

1. Neutrino Physics

Numerous fundamental discoveries in elementary particle physics have been achieved in the last decades. Successively the particles resembled in the Standard Model (SM) have been discovered experimentally. Most recently, the Higgs boson has been ascertained at the Large Hadron Collider (LHC) at CERN in 2012 [2]. Although the SM is a very reliable superposition of elementary particle physics, it is not able to explain all phenomena observed. In the following, the SM will be explained briefly and the neutrinos from the fermionic sector introduced in more detail. Furthermore, as especially observations from neutrino experiments hint towards physics beyond the standard model, some of these inconsistencies will be stated.

1.1. Standard Model of Particle Physics

The Standard Model (Fig. 1.1) is classified into two sectors: the fermionic and bosonic sector. The integer spin elementary particles are assembled in the bosonic sector. It consists of the four gauge and the Higgs boson. Each gauge boson carries a fundamental force, the gluon the strong, photon the electromagnetic, W- and Z bosons the weak force. Via the exchange of a gauge boson fermions take part in the corresponding interaction. The scalar Higgs boson gives mass to some elementary particles via the Higgs mechanism.

The fermionic part comprises half-integer spin elementary particles and can be sub-grouped into quarks and leptons. Quarks take part in the small-range strong force via the interaction with gluons and build half-integer spin nucleons, i.e. neutrons and protons and integer spin mesons. They also interact with the gauge bosons of the weak interaction, e.g. in the β -decay. Leptons on the other hand only interact with photons and the W- and Z-bosons. Associated to the electrically charged electron, muon and tau lepton are the neutrinos of the respective flavor. One special feature of the neutrinos is their helicity. In contrast to all other particles in the SM, neutrinos only exist with left-handed and anti-neutrinos with right-handed helicity. Furthermore, in the SM neutrinos are assumed to be massless, whereas neutrino flavor oscillation experiments have shown that at least two non-zero propagating neutrino mass eigenstates have to exist. In the following the specific features of neutrinos will be the main focus.

1. Neutrino Physics

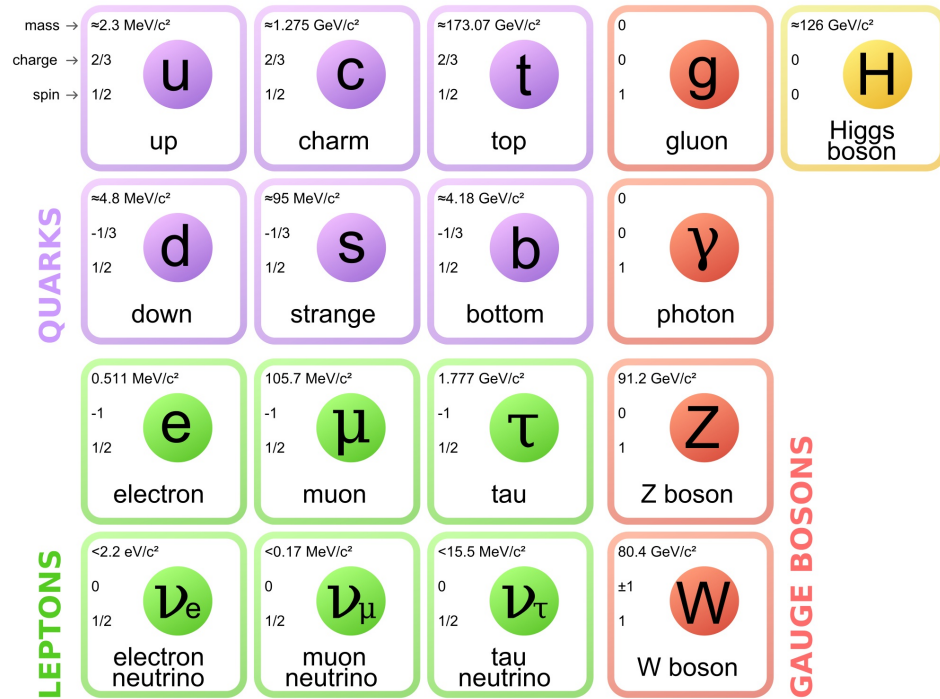


Figure 1.1: Illustration of the Standard Model of Particles [3]. It gives key information of the elementary particle's properties, such as their spin, electric charge and mass. The elementary particles are divided into a fermionic and bosonic part. Via the gauge bosons the fermionic elementary particles can take part in fundamental interactions, i.e. electromagnetic (photon), strong (gluon) and weak (W-, Z-boson) interaction. The interaction with the scalar Higgs boson results in a particle's mass.

1.2. Postulation and Discovery of the Neutrino

Many years after its theoretical prediction by W.Pauli in 1930, the neutrino was detected in 1956. In contrast to previous measurements of the α - and γ -decay that were in agreement with the assumed kinematics of a two-body decay, in the year 1914 J.Chadwick found a continuous energy spectrum of the emitted electrons in β -decays [4]. In the following Pauli's postulate and the experimental discovery of all three neutrino flavors will be outlined.

Postulation

The final state of the β -decay was first assumed to be a two-body state, where a nucleus decays into a daughter nucleus and an electron, see Eq. 1.1. Simple kinematics of the two-body state predict a monoenergetic electron spectrum, whereas the spectrum was found to be continuous by J.Chadwick in 1914. Moreover it was found that for the assumed two-body decay the spin conservation is violated, known as the spin statistic problem. The initial state of the β^\mp -decay is of half-integer in contrast to the integer final state, which equals either 0 or ± 1 .

$$\beta^- - \text{decay} : \quad (Z, A) \rightarrow (Z, A + 1) + e^- \quad (1.1)$$

$$\beta^+ - \text{decay} : \quad (Z, A) \rightarrow (Z, A - 1) + e^+ \quad (1.2)$$

Both experimental disagreements with the assumed theory pointed towards a new explanation. In 1930 W.Pauli postulated in his famous letter a new electrically neutral spin- $\frac{1}{2}$ particle that is emitted alongside the charged electron, which he called 'neutron'. By implementing the new particle, the β -decay is defined as a three-body decay (Eq. 1.3), and the inconsistencies with the measurements are resolved.

$$n \rightarrow p + e^- + \bar{\nu}_e \quad (1.3)$$

$$p \rightarrow n + e^+ + \nu_e \quad (1.4)$$

A few years later E.Fermi derived a theoretical description for the beta decay by an one-vertex decay, where all participating particles directly interact at this vertex. The calculation of the β -decay follows "Fermi's Golden Rule"

$$\Gamma = 2\pi \cdot G_F^2 \cdot |\langle f | M_{fi} | i \rangle|^2 \cdot \frac{dN}{dE} \quad (1.5)$$

with G_F the coupling constant, $|\langle f | M_{fi} | i \rangle|$ the transition matrix for $\langle f |, |i \rangle$ the wave functions of the final/initial state and M_{fi} the transition probability. The last term $\frac{dN}{dE}$ represents the final state density.

Due to the conclusion from comparisons between his theory and measured data he drew, that the hypothetical particle possesses either zero mass or many scales smaller than the electron. This lead to the renaming of Pauli's hypothetical neutron into 'neutrino' - little neutron.

1. Neutrino Physics

Discovery

The first experiment that gave evidence to the existence of the neutrino was part of the project Poltergeist by C.Cowan and F.Reines in 1953 [5]. Located at the Hanford reactor side, electron anti-neutrinos from the reactor hit a free proton in a Cadmium-loaded water ($\text{H}_2\text{O} + \text{CdCl}_2$) target producing a positron and neutron via the inverse beta-decay Eq. 1.6.



The tank holding the target is surrounded by a scintillating detector. The emitted positron in Eq. 1.6 annihilates with an electron thereby releasing two angular correlated gammas. These gammas produce a prompt signal in the detector. The neutron is first thermalized on a timescale of milliseconds and then captured by Cd. When the excited Cd-state decays into the ground state a delayed gamma signal is produced. Both, the prompt and delayed gammas, induce a response signal in the scintillating material, which then is detected by photo multipliers. A characteristic coincidence signal is created by the emitted photons from the positron annihilation and neutron capture thus allowing to identify the neutrino.

Discovery of ν_μ and ν_τ

The second neutrino flavor state ν_μ corresponding to the muon μ lepton was found by L.M.Ledermann, M.Schwary and J.Steinberger in 1962 at the Brookhaven Alternating Gradient Synchrotron (AGS) [6]. There, the pion decay was investigated and shown that the neutrinos coming from such a decay are different from the β -decay neutrinos. For this purpose a beryllium target was bombarded by a 15 GeV proton beam creating pions, which subsequently decay into muons and neutrinos.



The tracks from the decay products were detected in a 10 t aluminum spark chamber. If $\nu_e = \nu_\mu$ the following decay modes are possible and should have been observed.



However, only straight muon tracks were observed, easily distinguishable from electron tracks which generate an electromagnetic shower. Hence, the ν_μ as a second neutrino flavor was proven.

When in 1975 the τ -lepton was experimentally observed by M.L.Pperl at the SLAC accelerator [7], the existence of a third neutrino flavor completing the third lepton family - the tau

neutrino ν_τ was anticipated due to symmetry reasons. Finally, in 2000 the DONUT (Direct Observation of Nu Tau) experiment at Fermilab observed the ν_τ experimentally [8] via the inverse decay channel

$$\nu_\tau + n \rightarrow \tau^- + p. \quad (1.11)$$

The ν_τ -beam was generated by 800 GeV protons colliding with a tungsten target. With the help of emulsion plates the decay of Eq. 1.11 was observed. As a result of the short mean life-time of τ -leptons ($\tau = 3 \times 10^{-13}$ s) the corresponding decay signature in the form of a kink was expected at 2 mm for the neutrino energies in this experiment. For 203 neutrino interactions analyzed four tau neutrino interactions were observed [8] and the SM completed with three lepton families, each consisting of a charged lepton (e, μ, τ) and its neutrino counterpart (ν_e, ν_μ, ν_τ).

1.3. Number of Active Neutrino Flavors

The effective number of active neutrino species N_{eff} is a very interesting topic for particle physics as well as cosmology. The observed symmetry for the elementary particles resembled in the SM somehow "predicts" a neutrino to each corresponding lepton family. Indirect laboratory and cosmological measurements favor $N_{\text{eff}} \approx 3$, whereas especially cosmological boundaries strongly depend on the assumed underlying model.

1.3.1. Z0-Resonance

Already in 1989 the ALEPH experiment at the LEP collider at CERN determined the number of active SM neutrinos to

$$N_\nu = 2.9840 \pm 0.0082 [9]. \quad (1.12)$$

The measured cross-section of the Z boson resonance at 91 GeV is inverse proportional to the decay width. Further, the total decay width is defined by the sum of the visible decay width of the final states (leptons, hadrons) Γ_l, Γ_{had} and the invisible width $\Gamma_{inv} = N_\nu \Gamma_\nu$ to neutrinos, where N_ν is the number of light active SM neutrinos [9].

$$\Gamma_Z = 3\Gamma_l + \Gamma_{had} + N_\nu \Gamma_\nu \quad (1.13)$$

Assuming that the invisible Z decay incorporates only SM neutrinos, N_ν can be determined by comparing the ratio of the visible decay width with the SM prediction for the total width.

$$R_{inv}^0 = \frac{\Gamma_{inv}}{\Gamma_l} = N_\nu \left(\frac{\Gamma_\nu}{\Gamma_l} \right)_{\text{SM}}. \quad (1.14)$$

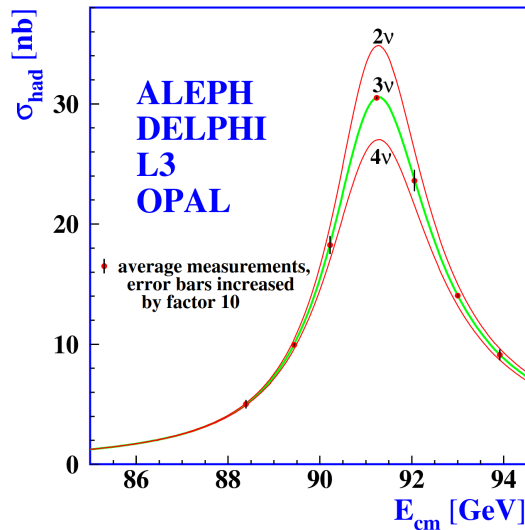


Figure 1.2: The measured hadron production cross-section around the Z-resonance. Assuming SM couplings and negligible neutrino mass, the curves show different presumptions for N_ν for the predicted cross-section. The measured data is in well agreement for $N_\nu \approx 3$. This figure is taken from [9].

1.3.2. Neutrino-to-Photon Ratio

The hot big bang model after inflation predicts the existence of relic neutrinos, forming the cosmic neutrino background (C ν B). Observations of the primordial abundance of light elements from the Big Bang Nucleosynthesis (BBN), anisotropies of the Cosmic Microwave Background (CMB) and the distribution of Large Scale Structures (LSS) confirm the assumption of relic neutrinos.

Apart from photons, neutrinos were still relativistic in the radiation dominated era of the Universe after they have decoupled from the primordial thermal plasma. Hence, the energy content of the radiation dominated epoch constitutes of relativistic photons and SM neutrinos. After the electron-positron annihilation, the relation between the different energy contents defines the number of effective SM neutrino species

$$N_{\text{eff}} = \frac{8}{7} \left(\frac{11}{4} \right)^{4/3} \left[\frac{\rho_r}{\rho_\gamma} - 1 \right]. \quad (1.15)$$

The Planck satellite set the constrain on the effective number of active SM neutrinos with 95%C.L. to

$$N_{\text{eff}} = 2.99_{-0.33}^{+0.34} [10, 11] \quad (1.16)$$

where small non-thermal corrections and the consideration of a non-instantaneous decoupling results in a small increase from $N_{\text{eff}} = 3$. Taking neutrino flavor oscillation and primordial nucleosynthesis into account and further including the most recent results on plasma thermodynamics QED corrections the effective number of neutrinos equals

$$N_{\text{eff}} = 3.0440 [12]. \quad (1.17)$$

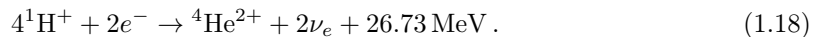
1.4. Neutrino Flavor Oscillation

The discovery of neutrino flavor oscillations was a huge milestone in neutrino physics. As this entails a non-zero neutrino mass, it has observable imprints in particle physics and cosmology. The latter mainly due to its huge abundance in the universe. Additionally, many open questions in neutrino physics can be explained by neutrinos oscillating between the three flavors, e.g. the solar neutrino problem.

In this section first the discovery of the neutrino oscillation and then the standard theoretical description will be outlined.

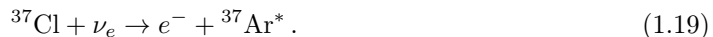
1.4.1. Solar Neutrino Problem

In nuclear fusion reactions suns convert hydrogen to helium. Whereas heavier stars are dominated by the CNO-cycle, our sun mostly generates helium via the pp-chain



In this process exclusively electron-neutrinos ν_e are produced. However, when the Homestake Solar Neutrino Experiment started taking data in 1970 of the solar neutrino flux, the measured data was not in agreement with theoretical standard solar model. With the measured solar neutrino flux being approximately $\Phi_\nu^{\text{sol}} \sim 6.6 \times 10^{10} \text{ cm}^{-2} \text{ s}^{-1}$, only a third of the expected rate was observed [13].

The Homestake experiment consists of a tank filled with 600 t perchloroethylene, containing ^{37}Cl . Solar neutrinos interact with the ^{37}Cl -nucleus via the inverse β -decay of chlorine to the excited state of argon



After a measuring interval of 60 days the argon gets separated. Via electron capture the excited argon state de-excited to the excited state of chlorine, subsequently decaying via Auger electron emission to the chlorine ground state. The Auger electrons are counted with a proportional counter.

1. Neutrino Physics

The measured deficiency was confirmed by other solar neutrino experiment such as GALLEX [14] and SAGE [15], leading to the so-called *solar neutrino problem*. Besides new theories for the solar model, Bruno Pontecorvo proposed in 1957 a neutrino-antineutrino mixing analog to the kaon meson oscillation [16]. Later, after some development of his theory, the foundation of neutrino flavor-mixing (*neutrino oscillation*) was introduced [17].

In 2001 the Sudbury Neutrino Observation (SNO) experiment, designed to measure neutrinos of all flavors, verified the neutrino oscillation hypothesis. The D₂O target allows neutral (NC) and charged current (CC) interactions as well as elastic electron scattering (ES) on deuterium:

$$\nu_e + d \rightarrow p + p + e^- \quad \text{CC - only for } \nu_e \quad (1.20)$$

$$\nu_\alpha + d \rightarrow p + n + \nu_\alpha \quad \text{NC - all flavors } \nu_\alpha \quad (1.21)$$

$$\nu_\alpha + e^- \rightarrow \nu_\alpha + e^- \quad \text{ES - all flavors } \nu_\alpha \quad (1.22)$$

Hence, it could be shown, that the solar neutrino flux is conserved when consisting of all three flavors ($\alpha = e, \mu, \tau$) [18]. Simultaneously, the Super-Kamiokande experiment proved the neutrino oscillation hypothesis for atmospheric neutrinos mainly coming from π -decays, assuming neutrinos change their flavor eigenstate while traveling through space [19].

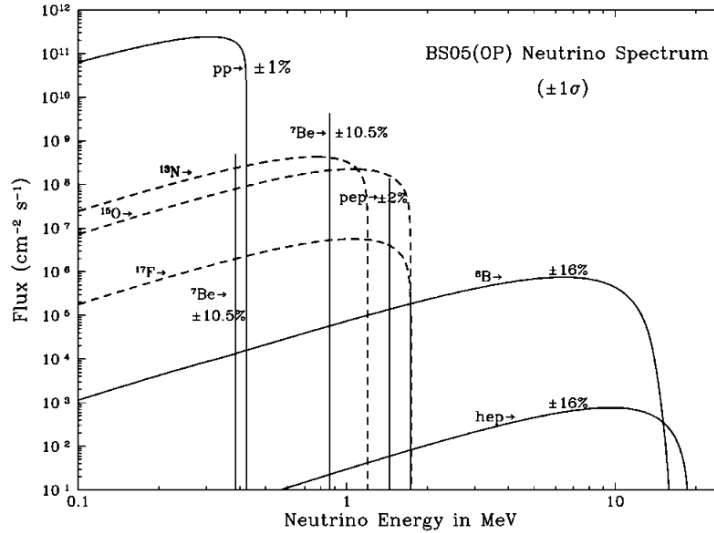


Figure 1.3: Representation of the solar neutrino flux as a function of energy, taken from [20]. The dashed lines correspond to the neutrino flux originating from the CNO-cycle, while the solid lines originate from the pp-chain. Corresponding to the decay the neutrinos are monoenergetic or have a continuous energy spectrum.

1.4.2. Theoretical description

Analogous to the mixing in the quark sector and the strong interaction, the phenomenon of neutrino oscillation emerges from the fact that the neutrino mass eigenstates are not identical to the flavor eigenstates, i.e. the neutrino state coupling to the weak interactions is not equal to the state they are propagating. Hence, the neutrino flavor eigenstate $|\nu_\alpha\rangle$ with $\alpha = e, \mu, \tau$ is a superposition of the neutrino mass eigenstates $|\nu_i\rangle$ where $i = 1, 2, 3$. The portion of the superposition is defined by the Pontecorvo-Maki-Nakagawa-Sakata (PMNS) matrix U .

$$|\nu_\alpha\rangle = \sum_i U_{\alpha i} |\nu_i\rangle \quad (1.23)$$

$$|\nu_i\rangle = \sum_\alpha U_{\alpha i}^* |\nu_\alpha\rangle \quad (1.24)$$

The 3×3 unitary matrix can be pictured as a rotation matrix, transforming by rotation the mass/flavor eigenstate, that are spanned in a three dimensional space, into each other.

$$\begin{bmatrix} \nu_e \\ \nu_\mu \\ \nu_\tau \end{bmatrix} = \begin{bmatrix} U_{e1} & U_{e2} & U_{e3} \\ U_{\mu1} & U_{\mu2} & U_{\mu3} \\ U_{\tau1} & U_{\tau2} & U_{\tau3} \end{bmatrix} \begin{bmatrix} \nu_1 \\ \nu_2 \\ \nu_3 \end{bmatrix} \quad (1.25)$$

The PMNS matrix contains all mixing parameters: the three mixing angles θ_{ij} , the CP-violating complex Dirac-phase δ_D and if neutrinos are Majorana particles the two complex Majorana-phases δ_M .

$$U = \begin{bmatrix} 1 & 0 & 0 \\ 0 & c_{23} & s_{23} \\ 0 & -s_{23} & c_{23} \end{bmatrix} \begin{bmatrix} c_{13} & 0 & s_{13}e^{-i\delta_D} \\ 0 & 1 & 0 \\ -s_{13}e^{-i\delta_D} & 0 & c_{13} \end{bmatrix} \begin{bmatrix} c_{12} & s_{12} & 0 \\ -s_{12} & c_{12} & 0 \\ 0 & 0 & 1 \end{bmatrix} \begin{bmatrix} e^{i\delta_{M1}} & 0 & 0 \\ 0 & e^{i\delta_{M2}} & 0 \\ 0 & 0 & 1 \end{bmatrix} \quad (1.26)$$

where $s_{ij} = \sin(\theta_{ij})$ and $c_{ij} = \cos(\theta_{ij})$.

The oscillation probability $P_{\alpha\beta}$ to find an initial flavor eigenstate $|\nu_\alpha\rangle(t)$ after some time t in another flavor eigenstate $|\nu_\beta\rangle$ is given by the projection of the time evolution of the initial state onto the final state $|\nu_\beta\rangle$

$$P(\nu_\alpha \rightarrow \nu_\beta) = |\langle \nu_\beta | \nu_\alpha(t) \rangle|^2 = \left| \sum_i U_{\alpha i}^* U_{\beta i} \cdot \exp(-iE_i t) \right| \quad (1.27)$$

with E_i the energy of the propagating mass eigenstate i . For ultra-relativistic neutrinos with $p_i \approx E_i$ the energy can be written as

$$E_i = \sqrt{p^2 + m_i^2} \approx E + \frac{m_i^2}{2E}. \quad (1.28)$$

1. Neutrino Physics

The final expression for the oscillation probability reads as

$$P_{\alpha\beta}(L, E) = \sum_{i,j} U_{\alpha i}^* U_{\beta i} U_{\alpha j} U_{\beta j}^* \cdot \exp\left(-i \frac{\Delta m_{ij}^2 L}{2E}\right) \quad (1.29)$$

with $\Delta m_{ij}^2 = m_i^2 - m_j^2$ the mass difference, L the distance of propagation and E the energy of the neutrino. If only two neutrinos participate significantly, the formula further reduces to (in natural units)

$$P_{\alpha\beta}(L, E) = \sin^2(2\theta) \sin^2\left(\frac{\Delta m^2 L}{2E}\right). \quad (1.30)$$

This equation illustrates that the mixing amplitude is dominated by the mixing angle θ and the mixing frequency by the mass splitting Δm^2 .

1.4.3. Experimental Determination of the Oscillation Parameters

The mixing angles θ_{ij} and mass splittings Δm_{ij} are accessible by different experiments. Solar neutrino experiments are sensitive to $ij = 12$, whereas $ij = 23$ is determined by atmospheric neutrino measurements. Reactor and accelerator experiments provide access to the mixing parameter $ij = 13$. Tuning the ratio L/E , the respective experiment is able to measure the oscillatory nature of the flavor transitions precisely. As neutrino oscillation experiments are only sensitive to the squared mass splitting Δm_{ij}^2 , there exist two possible scenarios for the neutrino mass ordering

$$\text{Normal ordering :} \quad m_1 < m_2 \ll m_3 \quad (1.31)$$

$$\text{Inverted ordering :} \quad m_3 \ll m_1 < m_2 \quad (1.32)$$

whereas global analysis of all experimental data favors the normal ordering by 3σ [21]. All mixing parameters are summarized in the PDG [22].

1.5. Neutrino Mass

As the observed neutrino flavor oscillation inevitably requires neutrinos to be massive, the SM has to be extended. Due to the smallness of their mass, i.e. five orders of magnitude less than the charged leptons, illustrated in Fig. 1.4, neutrinos gain their mass differently in contrast to all other elementary particles in the SM which acquire mass via the interaction with the Higgs field. One possibility to introduce a neutrino mass is the see-saw mechanism by adding right-handed *sterile neutrinos* to the SM. More details can be found in [23].

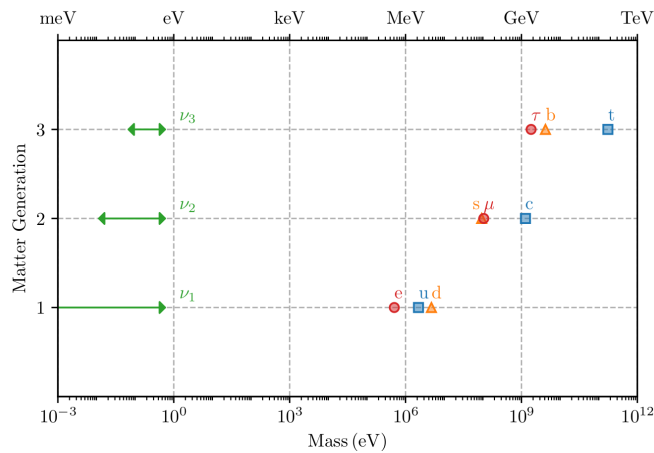


Figure 1.4: Illustration of the mass distribution for the fermion masses. Neutrinos possess a mass at least five orders of magnitude smaller than the charged fermions. The plot is taken from [24] with the data from [25].

First, SU(2) singlet ($T_3 = 0$, $Y_W = 0$) right-handed neutrinos, that cannot take part in the weak interaction, are introduced to formulate a neutrino mass term

$$(\nu_e)_R \quad (\nu_\mu)_R \quad (\nu_\tau)_R. \quad (1.33)$$

Via the Yukawa-coupling to the Higgs doublet the Dirac mass term is defined as

$$\mathcal{L}_D = -m_D (\bar{\nu}_L \nu_R + \bar{\nu}_R \nu_L) \quad (1.34)$$

$$m_D = y_D \frac{v}{\sqrt{2}} \quad (1.35)$$

where $v = 246$ GeV is the Higgs vacuum expectation value (vev) and $y_D \leq 10^{-10}$ the Dirac-Yukawa coupling.

1. Neutrino Physics

Assuming neutrinos to be Majorana particles, i.e. neutrinos are their own CP-conjugate, the Majorana mass term can be written as

$$\mathcal{L}_M = -\frac{1}{2}M_L(\bar{\nu}_L\nu_R^c + \bar{\nu}_R^c\nu_L) - \frac{1}{2}M_R(\bar{\nu}_R\nu_L^c + \bar{\nu}_L^c\nu_R). \quad (1.36)$$

This coupling of neutrinos and anti-neutrinos violates the lepton number conservation and needs therefore a different explanation than the SM Higgs mechanism. The Dirac and Majorana mass term for neutrinos can be combined to

$$\mathcal{L}_\nu = -\frac{1}{2} \begin{bmatrix} \bar{\nu}_L & \bar{\nu}_L^c \end{bmatrix} \begin{bmatrix} M_L & m_D \\ m_D & M_R \end{bmatrix} \begin{bmatrix} \nu_R^c \\ \nu_R \end{bmatrix} + h.c.. \quad (1.37)$$

Addressing the nature of the neutrino mass while avoiding an unphysically small Yukawa coupling the minimal type-I see-saw mechanism is introduced in the following.

1.5.1. See-Saw Mechanism

By implementing n right-handed sterile neutrinos to the SM, the see-saw mechanism provides an explanation of the small neutrino mass. Due to symmetry arguments $n = 3$ (Neutrino Minimal Standard Model ν MSM) would fit perfectly into the SM, whereas there are no theoretical limitations on n . For the sake of simplicity the case for $n = 1$ is considered. The minimal type-I see-saw mechanism represents a special case of Eq. 1.37 where $M_L = 0$ and $M_R \gg m_D$. By diagonalizing Eq. 1.37 the mass eigenvalue for the active m_{ν_a} and sterile m_{ν_s} neutrino can be extracted.

$$m_{\nu_a} \sim \frac{m_D^2}{M_R}, \quad m_{\nu_s} \sim M_R \quad (1.38)$$

The relation $m_{\nu_a} \propto m_{\nu_s}^{-1}$ shows that the heavier the additional sterile mass, the lighter the active SM neutrino. The main benefit of the type-I see saw mechanism is the natural mixing between the active and sterile state with the amplitude

$$|\theta| \sim \frac{m_D}{M_R} \sim \sqrt{\frac{m_{\nu_a}}{m_{\nu_s}}}. \quad (1.39)$$

As sterile neutrinos do not take part in any of the fundamental interactions but only via the active-to-sterile mixing, this mechanism would make the sterile state observable. Lastly, the problem with the too small Yukawa-coupling

$$y_D = \frac{\sqrt{m_{\nu_a} m_{\nu_s}}}{v} \quad (1.40)$$

can be avoided by large sterile neutrino masses.

It should be mentioned that there are different theories for the introduction of a neutrino mass. When considering the addition of right-handed sterile neutrinos via the see-saw mechanism, there exist no limitations on both the number of sterile neutrinos as well as on the sterile neutrino mass. Different sterile mass ranges can address certain open questions in physics, see Sec. 1.6.

1.5.2. Determination of Neutrino Mass

The determination of the neutrino mass is of great interest in modern physics. From the perspective of particle physics the knowledge about the neutrino mass provides a better understanding of the mass generation mechanism and helps to improve the theory of the SM. For cosmology, the neutrino mass enables the view on the early universe and its evolution. Due to the high neutrino abundance the neutrino mass had a huge impact when the structure formation took place. In the following three approaches to measure the neutrino mass are stated: the kinematics of the single β -decay, the neutrinoless double β -decay ($0\nu\beta\beta$) and cosmological surveys. All methods rely on different models. Hence, each approach is sensitive to a different effective neutrino mass.

Single β -decay

In a β^- -decay a neutron decays into a proton emitting an electron and an electron anti-neutrino

$$(A, Z) \rightarrow (A, Z + 1) + e^- + \bar{\nu}_e. \quad (1.41)$$

The released energy is mainly shared between the electron and the neutrino since the mass of the daughter nucleus is very large in comparison. As the neutrino has a non-vanishing rest mass, the maximal kinetic energy of the electron is given by

$$E_e^{\max} = E_0 - E_\nu(p_\nu = 0) \quad (1.42)$$

where E_0 is the kinematic endpoint. Investigating the spectral shape of the β -electron in the region close to the kinematic endpoint, the effective electron anti-neutrino mass is imprinted as the incoherent sum of the three neutrino mass eigenstates

$$m_{\bar{\nu}_e}^2 = \sum_i |U_{ei}|^2 m_{\nu_i}^2. \quad (1.43)$$

The current limit on the effective electron anti-neutrino mass is obtained by the combination of the first two measurement campaigns of the KATRIN experiment. KATRIN uses high precision β -spectroscopy of molecular tritium together with the MAC-E filter principle.

$$\langle m_\beta \rangle < 0.8 \text{ eV} \quad (90\% \text{ C.L.}) [26]. \quad (1.44)$$

This thesis is based on the kinematic principles of the β -decay in the KATRIN experiment. More details are explained in the following Chapter 2.

1. Neutrino Physics

Neutrinoless Double β -decay

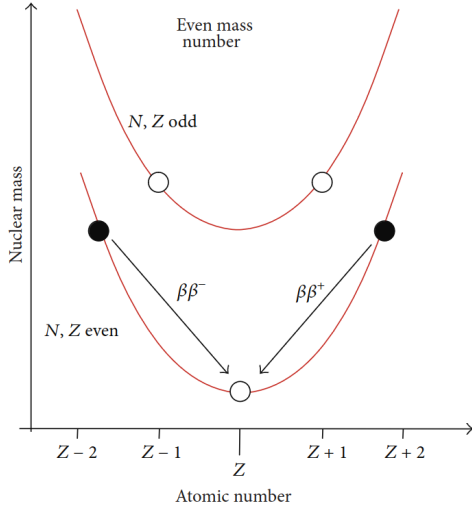
The binding energy of atomic nuclei and their decay schemes can be described by the Bethe-Weizsäcker formula. A β^- -decay converts an even-even in an energetically favored odd-odd state by transforming a neutron into a proton. For some cases, the daughter nucleus possesses a higher binding energy. Hence, the transition is energetically forbidden. The double β -decay ($2\nu\beta\beta$) as a second order weak process becomes observable in these cases, see Fig. 1.5a.

$$2n \rightarrow 2p + 2e^- + 2\bar{\nu}_e \quad (1.45)$$

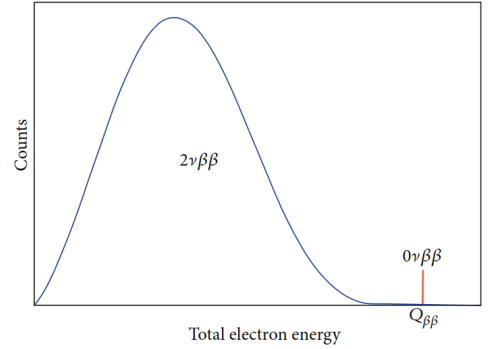
If the neutrino is a Majorana particle, i.e. its own anti-particle, the neutrino produced in one of the β -decays can be absorbed at the other vertex and therefore no neutrino final state is present. This process is called the neutrinoless double β -decay ($0\nu\beta\beta$)

$$2n \rightarrow 2p + 2e^- . \quad (1.46)$$

In this decay the lepton number is not conserved thus it is excluded in the SM. In contrast to the $2\nu\beta\beta$, in the $0\nu\beta\beta$ decay the sum of the energy is solely carried away by the electrons, leading to a monoenergetic line at the Q -value, see Fig. 1.5b.



(a) The binding energy of different nuclei as a function of the atomic number. In some scenarios the single β -decay is energetically forbidden and the double β -decay is necessary to reach the favored lowest energetic level while ensuring the energy conservation [27].



(b) Energy spectra for the double β -decay and the neutrinoless double β -decay. If neutrinos are of Majorana nature the electron solely carries the sum of the energy released in the decay. This results in a monoenergetic peak, whereas for $2\nu\beta\beta$ the energy is shared between the electron and neutrino leading to a continuous spectrum [27]

The Germanium Detector Array (GERDA) utilized high purity germanium detectors on the search for the experimental signature for $0\nu\beta\beta$ [28]. The combined analysis of Phase I and II

data provides a lower limit on the decay half-life of $T_{1/2}^{0\nu} > 1.8 \times 10^{26}$ yr (90% C.L.). This result can be converted into an upper limit for the effective Majorana neutrino mass with 90% C.L. of

$$\langle m_{\beta\beta} \rangle = \left| \sum_i U_{ei}^2 m_{\nu_i} \right| < (79 - 180) \text{ meV}. \quad (1.47)$$

The next generation experiment LEGEND requires a detector in the ton-scale with excellent energy resolution and extremely low background in the region of the signal. Besides covering the inverted ordering region, LEGEND is designed to probe the effective Majorana neutrino mass of 15 – 50 meV [29].

Cosmology

As a consequence of the vast neutrino abundance (336 relic neutrinos/cm³ in the present Universe), neutrinos play a significant role in the structure formation and the expansion of the early Universe. Hence, the imprint of the neutrino mass is experimentally accessible e.g. via the Cosmic Microwave Background (CMB), the large-scale structure distribution, weak-lensing and the Lyman- α -forest. Assuming the standard cosmological model, the Λ CDM-model, the Planck collaboration measured the CMB temperature fluctuations, constraining the absolute sum of neutrino masses to

$$\sum_i m_i < 0.12 \text{ eV} \quad (95\% \text{C.L.}) [1]. \quad (1.48)$$

1.6. Sterile Neutrinos

In the SM, only left-handed neutrinos ν_L and right-handed anti-neutrinos $\bar{\nu}_R$ exist. However, all other fermions exist in both left- and right-handed helicity. Consequently, the introduction of right-handed neutrinos is a natural and well-motivated extension to the SM. Since ν_R would not take part in any of the fundamental interaction the hypothesized 'sterile' neutrino is in accordance to existing theories [30]. These neutrinos would only participate via the mixing with the active SM neutrinos. Due to symmetry arguments three additional sterile neutrinos are a minimal extension of the SM, called the Neutrino Minimal Standard Model (ν MSM) [31].

For the sake of simplicity the extension of only one sterile neutrino is shown in the following. Analog to the active neutrino flavor oscillation, one additional sterile state and fourth mass eigenstate can be implemented in the PMNS matrix.

$$\begin{bmatrix} \nu_e \\ \nu_\mu \\ \nu_\tau \\ \nu_s \end{bmatrix} = \begin{bmatrix} U_{e1} & U_{e2} & U_{e3} & U_{e4} \\ U_{\mu1} & U_{\mu2} & U_{\mu3} & U_{\mu4} \\ U_{\tau1} & U_{\tau2} & U_{\tau3} & U_{\tau4} \\ U_{s1} & U_{s2} & U_{s3} & U_{s4} \end{bmatrix} \begin{bmatrix} \nu_1 \\ \nu_2 \\ \nu_3 \\ \nu_4 \end{bmatrix} \quad (1.49)$$

1. Neutrino Physics

Thus, all active neutrino flavor eigenstates possess a tiny fraction of the fourth mass eigenstate. The mixing strength is defined by the mixing amplitude $\sin^2(2\theta_{i4})$ and the frequency of occurrence by the respective mass splitting Δm_{i4}^2 .

However, the number of sterile neutrinos is not fixed. Further, since the sterile neutrino mass is not constrained from particle physics, it covers several orders of magnitude. Based on the mass scale, the mixing angle and the underlying production mechanism different open questions of modern particle physics can be addressed:

- **eV-scale** [32]

With a light eV-scale sterile neutrino experimental anomalies like the short baseline reactor anomalies (RAA) of the Liquid Scintillator Neutrino Detector (LSND) experiment could be explained. LSND found an excess of $\bar{\nu}_e$ in a $\bar{\nu}_\mu$ -beam which can be explained by the decay of a sterile neutrino into a scalar particle and a light neutrino of electron type [33]. The most recent Baksan Experiment on Sterile Transitions (BEST) probes the gallium anomaly (deficit of ν_e) of previous experiments and its possible connection to oscillations between active and sterile neutrinos. It claims that the deficit of ν_e from ^{51}Ce is consistent with a sterile neutrino in the eV-range with a significance of 4σ [34].

In contrast to oscillation experiment, the KATRIN experiment is also sensitive to eV-scale sterile neutrinos via a direct measurement [35].

- **keV-scale** [23]

Apart from Weakly Interacting Massive Particles (WIMPS) and axions, sterile neutrinos in the keV-mass range provide an elementary dark matter candidate. It could be warm or cold DM depending on its production mechanism. Observations of small-scale structures favor keV-scale sterile neutrinos as warm DM. However, these sterile neutrinos would not be stable but decay by mixing into a photon and light neutrino with a cosmologically-long lifetime. The space observatory X-ray Multi-Mirror (XMM)-Newton observed an unidentified emission line at $3.55 - 3.57 \pm 0.03$ keV which could originate from a sterile neutrino decay [36].

- **GeV-scale**

The ν MSM introduces a heavy sterile neutrino in the GeV-range in order to explain the smallness of the active neutrino masses via the see-saw mechanism. Furthermore, the baryon asymmetry in the Universe can be explained by oscillation-induced leptogenesis by implementing two heavy GeV-sterile neutrinos. To not interfere with the abundance of light elements in the Universe, these GeV-sterile neutrinos have to decay before the Big Bang Nucleosynthesis (BBN) [37].

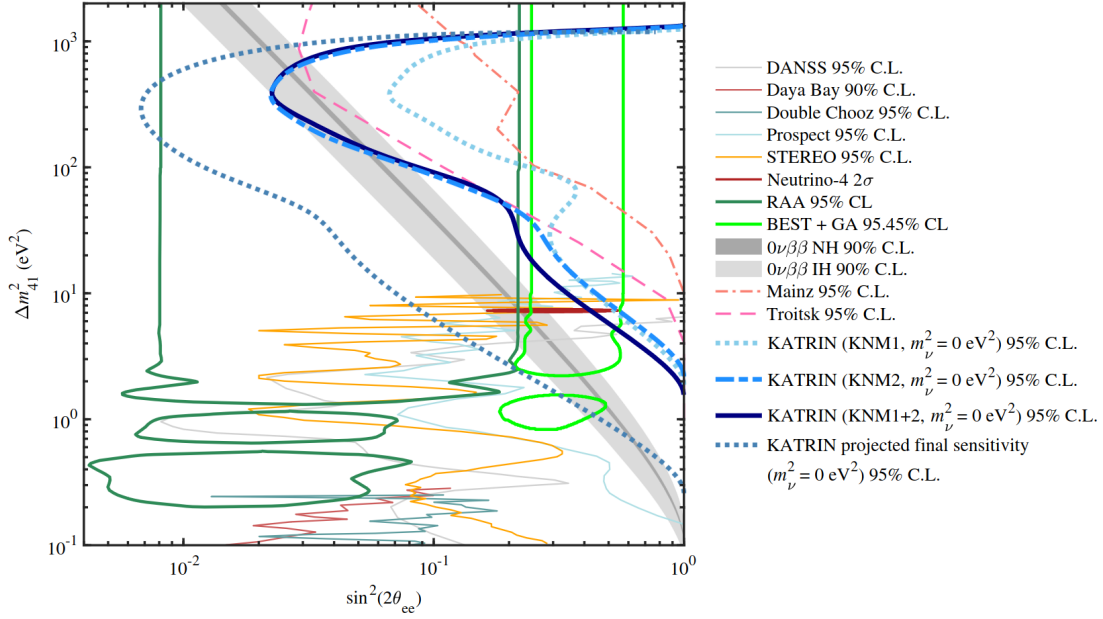


Figure 1.6: The current parameter space of a sterile neutrino with exclusions from various experiments. The allowed parameter space found by experiments as BEST+GA, Neutrino-4 and STEREO are enclosed by the solid contours. The dashed lines represent the excluded parameter space by all the other experiments. The results of KATRIN's predecessor experiments are shown as well as the current limits by the KATRIN experiment. Moreover, the projected future sensitivity of the KATRIN experiment is included, which will probe most of the BEST+GA allowed parameter space. This Figure is taken from [35].

2. The KATRIN Experiment

The **K**Arlsruhe **T**RItium Neutrino (KATRIN) experiment aims to measure the mass of the electron anti-neutrino in a direct and model-independent way with a sensitivity of 0.2 eV at 90 % confidence after 1,000 days of total measurement days [26]. Via high-precision spectroscopy the spectrum of the tritium β -decay



is measured close to its kinematic endpoint. The low atomic number of tritium coupled with the super-allowed nature of its β -transitions, allows a simple theoretical description of the β -decay. In addition its low Q-value of 18.6 keV and short half-life $\tau = 12.3$ yr make tritium a well suited isotope for the absolute neutrino mass measurement.

The effective neutrino mass leads to a reduction of the maximal available kinetic energy of the β -electron and thus to a distortion of the spectral shape compared to the theoretical prediction. For neutrinos with small mass differences, the distortion of the β -decay spectrum can be written as

$$\frac{dN}{dE} \simeq R(E) \sum_i |U_{ei}|^2 \sqrt{(E_0 - E)^2 - m_{\bar{\nu}_e}^2} \quad (2.2)$$

with $R(E)$ an energy dependent factor that contains all m_ν -independent parameters, $|U_{ei}|^2$ the respective elements of the Pontecorvo-Maki-Nakagawa-Sakata (PMNS) matrix describing the mixing between the electron flavor and the neutrino state i , and the endpoint energy $E_0 = 18.574$ keV [26]. The effective electron anti-neutrino mass $m_{\bar{\nu}_e}$ is given by the incoherent sum of neutrino mass eigenstates

$$m_{\bar{\nu}_e}^2 = \sum_{i=1}^3 |U_{ei}|^2 m_{\nu_i}^2. \quad (2.3)$$

In Fig. 2.1, the impact of a massive electron anti-neutrino close to the endpoint of the β -spectrum is illustrated for two non-physically large masses compared to the case of a massless neutrino. The decreasing amplitude of the distortion with the mass of the electron anti-neutrino combined with the small number of events expected around the endpoint energy make the experimental observation of such effect challenging. In order to deal with the experimental constraints, a high-luminosity source and a high energy resolution on the eV-scale are essential.

2. The KATRIN Experiment

This chapter gives a brief introduction of the neutrino mass measurement principle followed by a description of the current experimental setup with its main components. Further, the principles for the search of a keV-scale sterile neutrino will be explained.

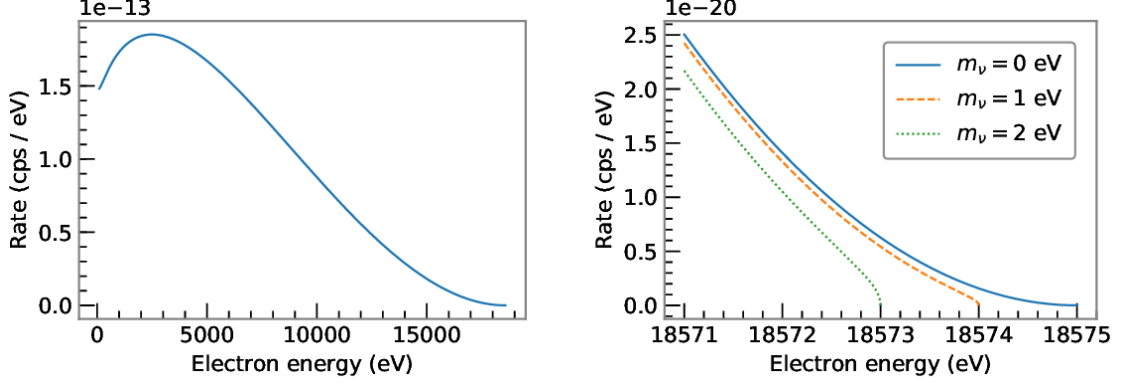


Figure 2.1: Illustration of the impact of a massive neutrino on the differential β -electron spectrum close to the endpoint [38]. As a reference, the blue lines show the β -spectrum for the case of a neutrino with zero mass where no reduction of the maximal available kinematic energy nor a spectral distortion are present. For the purpose of clarification, the impact of two unphysically large effective electron anti-neutrino masses are depicted by the green and orange lines.

2.1. Experimental Setup

The KATRIN experiment is located at the Karlsruhe Institute of Technology (KIT) and started measuring the β -electrons from the tritium decay in 2018 [39]. It consists of a 70 m long beamtube from the rear section to the focal plane detector as shown in detail in Fig. 2.2. The beamtube is composed of four sections: the source, the transport, the spectrometer and the detector section. In the following the sections will be described and the working principles explained. More details can be found in the KATRIN design report of 2021 [40].

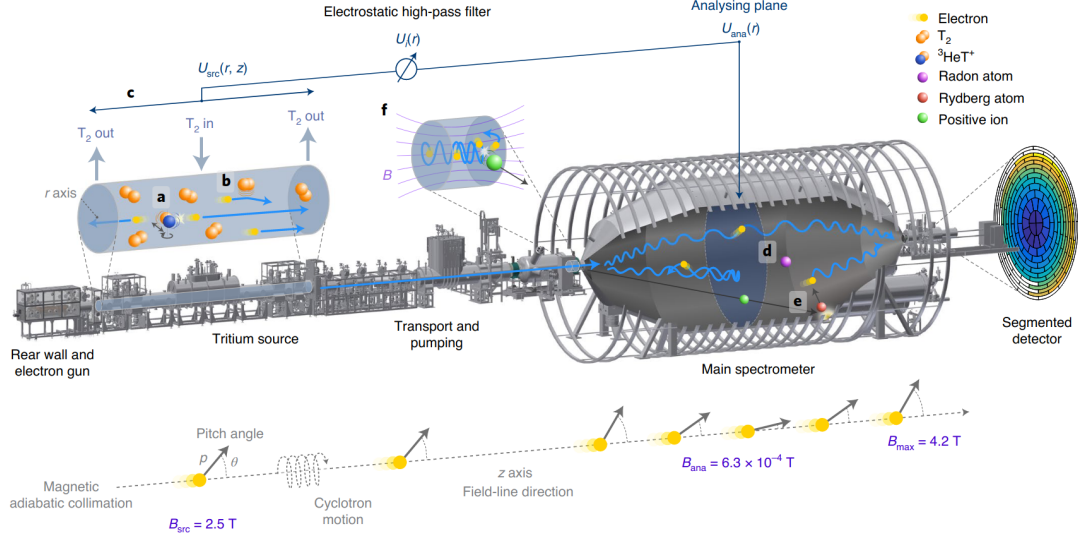


Figure 2.2: Illustration of the KATRIN beamline [26]. The 70 m beamline starts at the rear section, followed by the source section where the tritium decay takes place. The electrons are guided magnetically through the transport section in which the tritium gas and helium ions are removed by the differential and cryogenic pumping units. After the transport section starts the spectrometer section consisting of a pre and main spectrometer. Both spectrometers act as high-pass filters (MAC-E filters), setting a lower energy threshold for the electrons. Electrons transmitted through the main spectrometer are counted at the focal plane detector as a function of the retarding potential.

2.1.1. Source Section

Windowless Gaseous Tritium Source (WGTS)

Electrons are produced in the 10 m WGTS where highly purified molecular tritium gas is continuously injected. The tritium gas diffused towards both ends of the tube where it is then pumped out and fed into the tritium loop system. The tritium loop purifies the gas and re-injects it to the WGTS. Due to the short half-life of $\tau = 12.3$ yr tritium provides a source with high activity of up to 10^{11} Bq. In order to ensure a stable source at the 0.1 % level [26] and avoid Doppler effects caused by thermal gas motion, the WGTS is operated at a temperature of 80 K. The β -electrons are guided magnetically through the transport to the spectrometer section. The required magnetic field is induced by three super-conducting magnets and a solenoid surrounding the source. In addition, at each the back and front end of the WGTS two solenoids provide a magnetic field at the rear section and a homogeneous transition field towards the transport section.

On the back end of the WGTS the rear section is located. It is composed of a gold-plated rear wall disc which provides a constant source potential and absorbs the non-transmitted electrons. By measuring the x-rays generated by the absorption of the β -electrons in the gold coating of the rear wall, the stability of the source activity can be monitored [41]. Furthermore, an angular

2. The KATRIN Experiment

selective electron gun (e-gun) sits in the rear section, producing mono-energetic electrons which are employed for calibration measurements such as e.g. the determination of the gas density.

2.1.2. Transport Section

The purpose of the transport section is to first guide the β -electrons adiabatically towards the spectrometer section while also reducing neutral tritium gas by more than 14 orders of magnitude with respect to the WGTS with a combination of differential (DPS) and cryogenic pumping sections (CPS). The information presented in this section was taken and summarized from [42].

Differential Pumping Section (DPS)

At the end of the source section, the tritium flux is reduced by seven orders of magnitude by the DPS. Five super-conduction solenoids surrounding the beam tube are each tilted by 20° . In contrast to the electrically charged electrons which follow the guiding field lines, neutral tritium molecules scatter with the walls in the DPS and are then pumped out. The positive helium ions that are generated alongside in the β -decay, are charged particles that are also guided by the magnetic field and can potentially produce an unwanted background in the main spectrometer. Three dipole electrodes ensure the removal of ions by an induced $E \times B$ -drift. Electrons are 10^4 times lighter than the helium ions and hence remain unaffected by the dipoles.

Cryogenic Pumping Section (CPS)

The CPS reduced the tritium flux by more than seven orders of magnitude. The inner surface of the CPS is operated at 3 K and the tritium molecules are frozen onto an argon frost layer. As described for the DPS, the CPS elements containing the argon frost layer are tilted by 15° , absorbing the tritium molecules while the β -electrons are guided magnetically to the spectrometer section.

2.1.3. Spectrometer Section

The two spectrometers act as high-pass filters based on the MAC-E filter principle by applying magnetic adiabatic collimation together with an electrostatic filter. Only electrons with a higher kinetic energy than the applied retarding potential qU are transmitted through the respective spectrometer.

MAC-E Filter Principle

In a MAC-E filter, electrons are guided by the magnetic field through the spectrometer. Only electrons that possess enough energy to overcome the retarding potential qU , parallel to the magnetic field lines, are further transmitted (high pass filter). The total kinetic energy of an

electron can be divided into a transversal and longitudinal component

$$E_{tot} = E_{\perp} + E_{\parallel}. \quad (2.4)$$

However, only the longitudinal part E_{\parallel} can be analyzed by the electrostatic filter at the analyzing plane. At the analyzing plane, where the magnetic field is the weakest, the kinetic energy of the signal electrons is determined via the longitudinal retarding potential. In order to achieve both the highest possible count rate at the detector and a good energy resolution, the transversal component E_{\perp} has to be transformed almost entirely into the longitudinal component E_{\parallel} before the signal electrons reach the analyzing plane. This is realized via the Magnetic Adiabatic Collimation (MAC) principle. The polar angle of the electron's trajectory, the angle between the transversal and longitudinal components, is proportional to the magnetic field strength. By lowering the magnetic field inside the main spectrometer the polar angle is decreased, therefore transforming the energy mostly into the longitudinal component. The magnetic field strength drops by four orders of magnitude between the source and the analyzing plane. In order to keep the electron trajectories controllable, the particle motion has to be kept adiabatic. To ensure the adiabatic electron transmission the field gradient needs to be small within one cyclotron length. Details on the adiabatic transmission conditions can be found in Chapter 5.

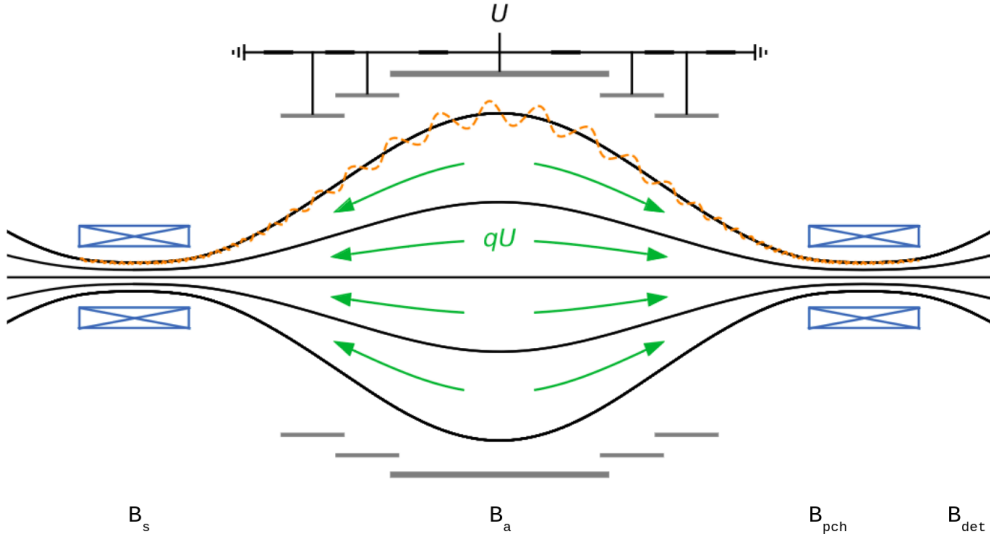


Figure 2.3: Illustration of the working principle of the MAC-E filter. The electrons (orange line) follow the guiding magnetic field lines in cyclotron motion represented by the black lines and have to overcome the retarding potential indicated by the green arrows. Further, the present magnetic field strengths, induced by the respective beamline magnets, are included. The magnets are operated with the 70 % KATRIN beamline setting, i.e. $B_s = 3.2$ T, $B_{pch} = 4.2$ T and $B_{det} = 2.5$ T. Because of the MAC principle the magnetic field strength inside the MS is lower, namely $B_a \propto 10^{-4}$ T. This figure was adopted from [43].

2. The KATRIN Experiment

Two important parameters associated to a MAC-E filter are the maximum acceptance angle θ_{max} and the energy resolution ΔE at the analyzing plane.

Maximum Acceptance Angle

As mentioned, the polar angle of the electron is proportional to the magnetic field strength. If the electron experiences an increasing magnetic field, the polar angle also increases until a maximum angle of $\theta = 90^\circ$ is reached and the electron gets magnetically reflected. The strongest magnetic field is close to the detector, the pinch magnet B_{pch} . This implies a maximum angle with which electrons can start at the source S without being magnetically reflected. If the transmission is fully adiabatic, the orbital magnetic moment μ is conserved.

$$\mu \approx \frac{E_\perp}{|\vec{B}|} = \frac{E_{kin}^{tot} \cdot \sin^2(\theta)}{|\vec{B}|} \approx \text{const.} \quad (2.5)$$

Due to energy conservation and assuming that the electron gets reflected at the pinch magnet ($\sin^2(\theta_{pch}) = 1$) this leads to the following relation:

$$\sin(\theta_{max}) = \sqrt{\frac{|\vec{B}_s|}{|\vec{B}_{pch}|}} \quad (2.6)$$

$$\theta_{max} = 60.79 \text{ deg} \quad (2.7)$$

Energy Resolution

Although the magnetic field at the analyzing plane is very small ($B_a \propto 10^{-4} \text{ T}$), some of the electron's energy remains in the longitudinal component thus leading to the energy resolution of the MAC-E filter

$$\Delta E = E_{a,\perp}^{min}. \quad (2.8)$$

The minimal transversal kinetic energy at the analyzing plane corresponds to the maximal transversal kinetic energy at the pinch magnet, i.e $E_0 = 18.574 \text{ keV}$.

$$\Delta E = E_0 \cdot \frac{B_a}{B_{pch}} \approx 0.37 \text{ eV} \quad (2.9)$$

This also implies that electrons with a polar angle $\theta > 0$ need more kinetic energy to overcome the retarding potential than an electron starting with $\theta = 0$ only possessing longitudinal kinetic energy.

Pre-Spectrometer (PS)

The PS acts as a pre-filter to reduce the electron flux in the main spectrometer (MS) and therefore to minimize the background and ionization processes in the MS. The retarding potential inside the PS was set to 18.3 kV only transmitting electrons with an energy of 300 meV below the endpoint of the spectrum or higher [40]. However, after some operation time it was observed that Penning traps at both ends of the PS largely contributed to the background [44]. Therefore, since the fifth neutrino mass measurement campaign, the retarding potential of the PS was set to zero.

Main-Spectrometer (MS)

Along the full beamline the magnetic flux is conserved

$$\Phi = \int_A \vec{B} \cdot d\vec{A} = \text{const.} \quad (2.10)$$

Due to the large dimensions of the MS with a total length of 23.3 m and a radius of 5 m, the possibilities of background processes also increase. To reduce the background resulting from scattering processes with residual gas molecules in the spectrometer volume, the MS is operated at an ultra high vacuum of 10^{-10} mbar. Additionally, to decrease the number of secondary electrons induced by cosmic muons, the spectrometer vessel wall is lined with an electrode system operated at $U_{\text{offset}} = -200$ V. Hence, electrons generated at the wall of the MS are reflected back and do not contribute to the background. In order to induce the low magnetic field ($\propto 10^{-4}$ T) in the center of the MS, required for the MAC-E filter principle, the MS is coaxially surrounded by large air coils (12.6 m of diameter) forming the *Low Field Coil System* (LFCS), depicted in Fig. 2.4. Due to the small magnetic field strength, the impact of the earth magnetic field ($\propto 10^{-6}$ T) cannot be neglected. Its impact as well as the fine-shaping of the small magnetic field is compensated and ensured by a second Air Coil System the *Earth Magnetic Compensation System* (EMCS), consisting of 16 vertical and 10 horizontal cosine coils [45].

Low Field Coil System (LFCS)

The main purpose of the LFCS is to provide a weak magnetic field at the analyzing plane for the neutrino mass measurement. Precision fine-tuning of the shape of the magnetic field inside the MS and hence the adjustment of the total field strength is also achieved by the LFCS. Different magnetic field profiles can be set as each coil's current is independently tunable [45]. Three superconducting coils close to the MS, the pre-spectrometer magnet 2 (PS2), pinch (PCH) and detector (DET) coils contribute to the magnetic field inside the MS. As a consequence of their larger magnetic moment, the coils at the detector side (PCH, DET) contribute to the magnetic field inside the MS more. This leads to an asymmetric MS magnetic field configuration [45]. To ensure adiabatic electron transmission, the field gradient has to be kept very small. The transmission condition can be best satisfied if the superconducting stray field is smaller than the LFCS field. In 2019, when the LFCS was upgraded, 5 additional coils were installed and all single layer

2. The KATRIN Experiment

extended to double layer coils. All 20 coils can be operated with a maximum current of 120 A [46]. This upgrade helps to compensate the magnetic field asymmetries resulting from the larger stray fields more accurately and provides the possibility to set a larger overall magnetic field strength inside the MS. For the search of a keV-scale sterile neutrino, the maximal technically feasible LFCS setting also enlarges the accessible energy range of the β -spectrum without an unacceptable transmission loss. This effect is studied in detail in chapter 5.

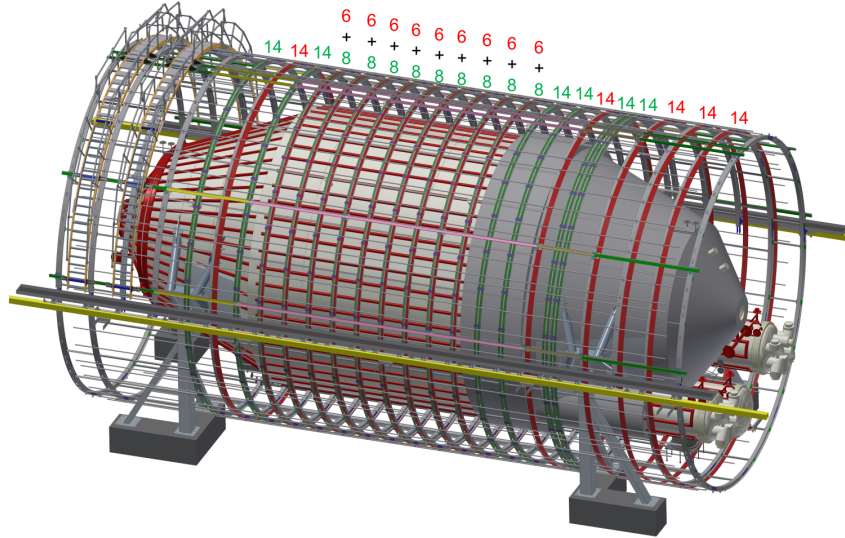


Figure 2.4: Schematic view of the upgraded KATRIN main spectrometer and the air coil system. The 15 air coils before the LFCS upgrade are shown in green, and the 5 additional coils in red. All coils currents can be set independently with an maximal current of 120 A. This figure is taken from [46].

2.1.4. Detector Section

Electrons that are transmitted through the main spectrometer are re-accelerated by the post acceleration electrode (PAE) currently set to $U_{PAE} = 10\text{ keV}$ and focused onto the focal plane detector (FPD). With the help of the PAE signal electrons possess a higher incident energy at the FPD allowing to discriminate them from low energy background events. Further, the longitudinal kinetic energy increases and therefore the incident angle is decreased, reducing electron back scattering at the detector [47].

FPD

The FPD is a multi-pixel silicon PIN diode detector with a radius of 45 mm and segmented in 148 pixels, each of the equal surface area of 44 mm^2 as shown in Fig. 2.5. The detector wafer is surrounded by the detector magnet currently operated with a field strength of 2.52 T. As the KATRIN experiment is operated in the integral mode the energy resolution is determined by the retarding potential in the MS and the electrons are only counted at the FPD with a detection efficiency of approximately 93%. Nevertheless, the detector has a mean energy resolution of about $\Delta E = 1.5\text{ keV}$ at full width half maximum at $E = 18.6\text{ keV}$ [48] in order to discriminate detector systematic uncertainties.

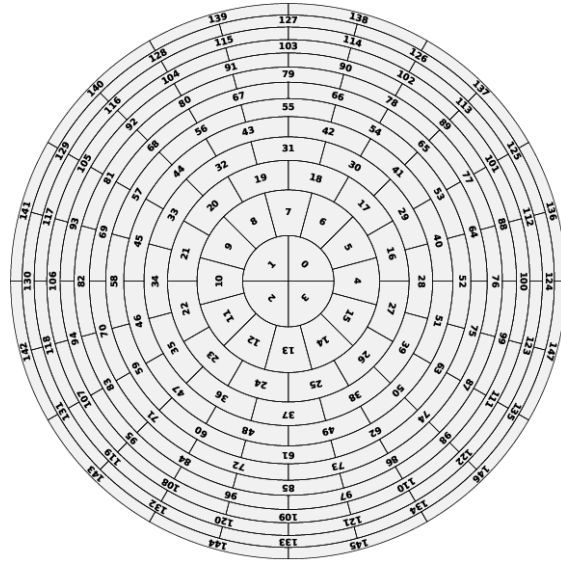


Figure 2.5: Schematic depiction of the focal plane detector (FPD) of the KATRIN experiment. The 148 pixels exhibit the same size of 44 mm^2 . This figure is taken from [38].

2.2. Neutrino Mass Measurement

The neutrino mass is determined by comparing the theoretically expected spectrum with the measured integral spectrum. Four free parameters are taken into account in the analysis: the signal amplitude, the endpoint, the background rate and the neutrino mass. The most recent published results of the KATRIN experiment based on the data of the first two measurement campaigns (KNM1, KNM2) of 2019 provide the most stringent constrain on the upper mass limit for the effective electron anti-neutrino mass. With a total number of 1.48×10^6 (3.68×10^6) collected β -electrons in the range of interest and a 521.7 h (743.7 h) period of data taking for KNM1 (KNM2), the simultaneous fit of both data sets yield $m_{\bar{\nu}_e}^2 = (0.1 \pm 0.3) \text{eV}^2$, setting $m_\nu < 0.8 \text{eV}$ (90% C.L.) [26]. In Fig. 2.6 the best-fit models for both KNM1 and KNM2 are shown as well as the best-fit results from previous experiments. The neutrino mass result is dominated by statistical uncertainty and the most impactful systematic uncertainties are due to background properties and source electric potential [26].

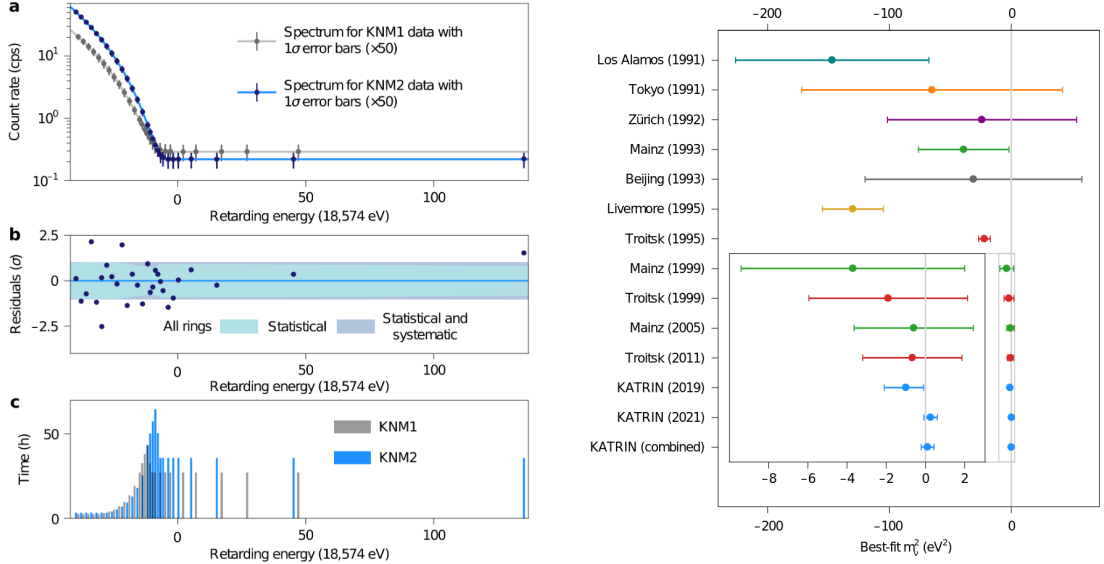


Figure 2.6: (Left): Measured count rate for each retarding potential for the first two KATRIN measurement campaigns KNM1 and KNM2. (a) Count rate over all detector rings for each retarding energy. The error bars represent the statistical uncertainties, multiplied by a factor of 50. The colored lines show the best-fit models for both KNM1 and KNM2. For the second campaign a higher statistic can be seen together with a lower background rate. (b) Normalized residuals for the KNM2 data fit. The shaded areas indicate the statistical and total uncertainty. (c) The measurement time distribution for the two campaigns. (Right): Results for the neutrino mass of past experiments and the KATRIN experiment. The error bars show the combined statistical and systematic uncertainties. Both figures are taken from [26].

2.3. keV Sterile Neutrino Search

Previous studies [49] have shown that a high statistical sensitivity on keV-scale sterile neutrinos can be achieved with the KATRIN experiment. As neutrino oscillation experiments have shown a very small mass difference between the active neutrino flavors ($10^{-3} - 10^{-5}$ eV) the resolution in a β -spectrum of such is impossible with current technology. However, assuming a heavy sterile mass eigenstate m_4 would lead to an observable distortion in the β -spectrum

$$\frac{d\Gamma}{dE} = \cos^2 \theta \frac{d\Gamma}{dE}(m_\beta) + \sin^2 \theta \frac{d\Gamma}{dE}(m_{\nu_4}) \quad (2.11)$$

with the effective electron neutrino mass m_β and the fourth mass eigenstate m_4 . The amplitude $|U_{e4}|^2 = \sin^2 \theta$ characterizes the mixing between the active and sterile eigenstate. Fig. 2.7 shows the observable spectral distortion in the β -spectrum of tritium. The kink-like signal would manifest itself at $E_0 - m_4$ as the measured signal is a superposition of the active and sterile branch, where the signal extends over the full energy range. In contrast to the neutrino mass measurement, where a narrow energy range very close to the endpoint is considered, the energy range has to be much wider for a keV-scale sterile neutrino search. The tritium β -decay enables a study of the sterile neutrino mass up to the kinematic endpoint of 18.574 keV. In order to increase the sensitivity on the active-to-sterile mixing parameter, the KATRIN experimental set-up together with the new TRISTAN detector system is needed.

The novel detector system, under development for the keV-scale sterile neutrino search with tritium, is presented in the following chapter. Challenges associated to scanning a wider energy region by lowering the retarding potential in the MS are described and studied in detail in Chapter 5.

2. The KATRIN Experiment

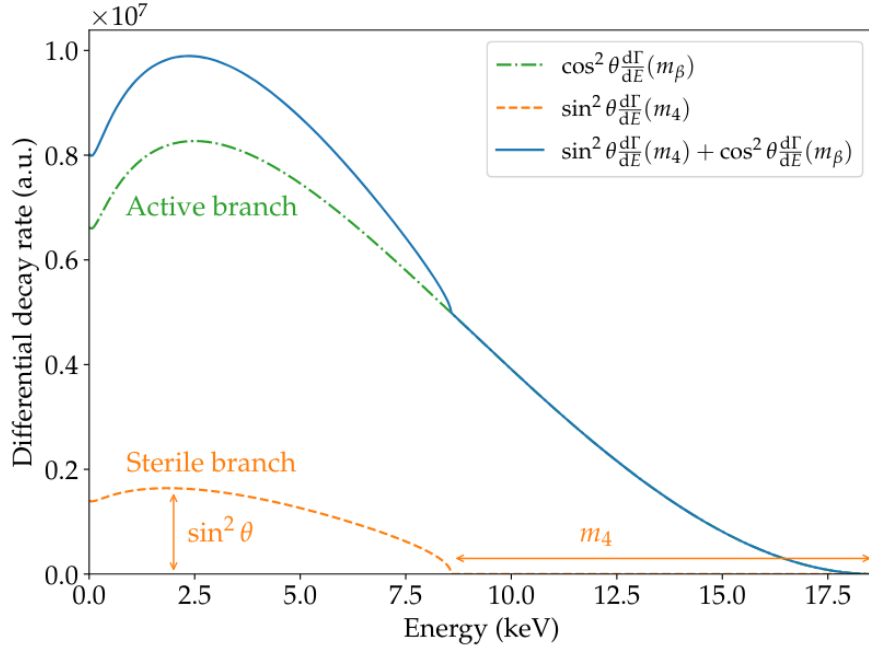


Figure 2.7: Tritium decay spectrum without and with the presence of a sterile neutrino with a mass of $m_4 = 10$ keV and an unphysical large mixing angle. The green dash-dotted line shows the beta spectrum without a sterile neutrino. The orange dotted line shows the decay branch into a sterile neutrino, the red dashed-dotted decay branch into an active neutrino. The superposition of these two spectra is shown by the red solid line, demonstrating the kink-like distortion at $E_0 - m_s$ [50].

3. The TRISTAN Project

After the completion of the neutrino mass measurement campaign in 2025, the KATRIN experiment is planned to be extended with a new multi-pixel silicon drift detector (SDD) system to search for a keV-scale sterile neutrino signal in the β -decay spectrum of tritium. The so-called **T**ritium **I**nvestigation on **S**terile-to-**A**ctive **N**eutrinos (TRISTAN) project will study the entire tritium β -decay spectrum by lowering the filter voltage to much lower values than in the current KATRIN operation. A combination of a lower source strength and a modified magnetic field setting allows to probe the sterile neutrino phase space with mixing amplitudes down to $\sin^2 \theta \sim 10^{-6}$, see Fig. 3.1. The main challenge of a keV-scale sterile neutrino search is to resolve precisely very small spectral distortions on the parts-per-million (ppm) level while handling very high count rates of 10^8 cps [51]. With the intention to reduce systematic uncertainties, a combination of an integral and differential measurement mode is also considered. The energy determination for the integral mode is based on the MAC-E filter principle in the MS together with a counting detector, as for the current KATRIN experiment. In the case of the differential mode, a low constant retarding voltage is applied and the energy of the incident electrons is determined by the detector. Consequently, this demands an excellent energy resolution and accurate understanding of the detector response.

The TRISTAN detector relies on the Silicon Drift Detector (SDD) technology. Therefore, the working principle of SDDs is explained briefly before the TRISTAN detector is introduced.

3. The TRISTAN Project

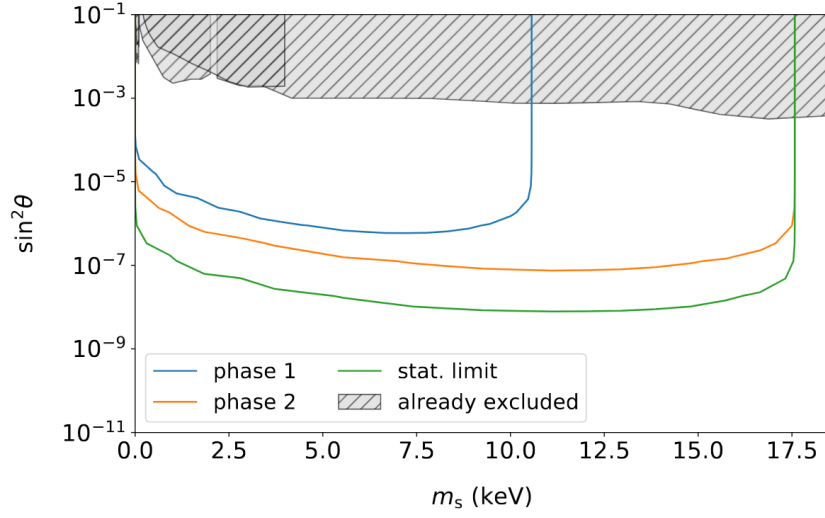


Figure 3.1: Sensitivity of KATRIN equipped with TRISTAN modules to the sterile neutrino parameter space. The statistical limit is reached with a statistics of 10^{18} electrons over the full energy range (green line). This would correspond to a measurement time of 3 years at the KATRIN full source strength. Phase-1 and Phase-2 consider different source strength and analysis windows in order to control systematic uncertainties. The targeted sensitivity of $\sin^2 \theta = 10^{-6}$ is foreseen to be reached by Phase-2, [52].

3.1. Silicon Drift Detectors

Semiconductor Detectors

Semiconductors consist of a negative n-doped (electron donor) and a positive p-doped (electron acceptor) material. Electrons from the n-doped material diffuse into the p-doped material recombining with the electron acceptor ions. Vice versa, holes recombine with electron donor ions in the n-doped side. The remaining donor and acceptor ions close to the p-n-junction induce an electric field which leads to a charge carrier free depletion zone. When a voltage is applied in a reverse bias configuration, the electrons and holes are attracted to the other side. Thereby, the size of the depletion zone is increased. The voltage necessary to deplete the full detector volume is called depletion voltage. The fully depleted volume of a semiconductor can be used for the detection of charged particles and photons. When such a particle enters the detector material, valence electrons from the donor material are excited into the conductor band. With this process, electron-hole pairs are created. The number of pairs depends on the incident particle's energy and on the material dependent average energy required to generate one electron-hole pair. Due to the opposite charge, electrons and holes move towards the negative n-doped (anode) or positive p-doped (cathode), creating an electric current that can be read out. Semiconductor detectors are operated at low temperatures to reduce the leakage current caused by thermal effects.

PIN Diode Detectors

Positive, intrinsic and negative (PIN) diode detectors are based on the semiconductor detector principle. They consist of thin layers of n- and p-doped silicon with a high acceptor and donor density, separated by an intrinsic n-type silicon layer of very low donor density. By applying a voltage, the detector volume can be fully depleted. In order to reduce the capacity of the detector the size of the anode is small with respect to the cathode.

Silicon Drift Detectors (SDD)

Silicon Drift Detectors (SDD) comprise an intrinsic n-type silicon substrate, framed on both sides by a p-doped silicon layer. The negative bias voltage is applied to the p-doped back contact, i.e. the entrance window of the detector. The other side consists of p-doped drift rings around the n-doped anode at the center, and is connected to the front-end electronics for the read out. The negative voltage of the drift rings decreases towards the anode, causing incident electrons to drift towards the anode. Holes are collected at the back contact or drift rings. Hence, the SDD technology adds sideways depletion to the PIN diode detector and enables a high rate operation with low electronic noise. SDDs meet the requirements of TRISTAN as they exhibit an excellent energy resolution (300 eV FWHM at 20 keV) while exhibiting low energy threshold (< 2 keV) for high count rates ($\sim 10^5$ cps for 3 mm pixel [51]).

3.2. TRISTAN Detector

The TRISTAN detector is based on the SDD technology for the search of a keV-scale sterile neutrino. Multiple hexagonal SDD cells are combined to a gapless arrangement with a common voltage supply and entrance window but an individual read-out. In Fig. 3.2 a TRISTAN SDD cell is shown schematically. Detailed information can be found in [51, 53, 54].

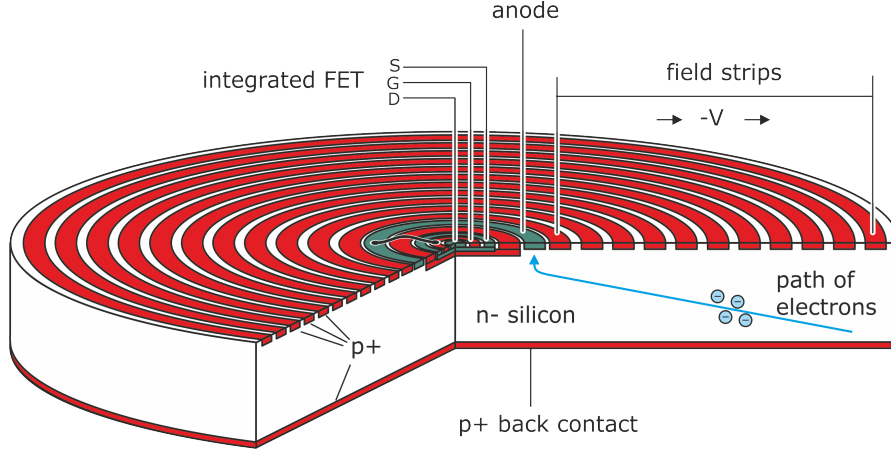


Figure 3.2: Schematic drawing of a SDD TRISTAN detector cell. The p-doped back contact and drift rings are shown in red. The n-doped anode at the read-out side of the cell is shown in green. Electrons can only enter the detector volume through the back contact side. An exemplary electron path in the fully depleted intrinsic silicon layer is shown in blue. Due to the negative voltage at the back contact and the to the center decreasing negative voltage of the drift rings, electrons drift towards the anode in the center. This figure is adapted from [53].

In order to mitigate the impact of systematic effects such as e.g. pile-up and charge sharing, a maximal count rate of 10^5 cps is foreseen. Ideally, the beamtube is mapped onto the full detector surface. As the magnetic flux $\Phi = B \cdot A$ is conserved along the full beam line, the size and location of the detector can be optimized. Based on the magnetic field configuration at the detector, the optimum of pixel and detector size depends on systematic effects such as charge-sharing, energy resolution, charge collection time and backscattering probability.

The development of the TRISTAN detector follows a stage approach. Beginning with a 7-pixel detector prototype, the general detector properties were studied. The pixel number per module was increased to 47 and 166. Extensive characterization and tests have been performed successfully [55]. The final detector system, consisting of 9 modules, with the option of 21 modules, each consisting of 166 pixels, is planned to be integrated in the KATRIN beamline in 2026 after the completion of the neutrino mass measurement campaign. In Fig. 3.3 a depiction of the TRISTAN module and the assembly of 21 modules to form the detector is shown.

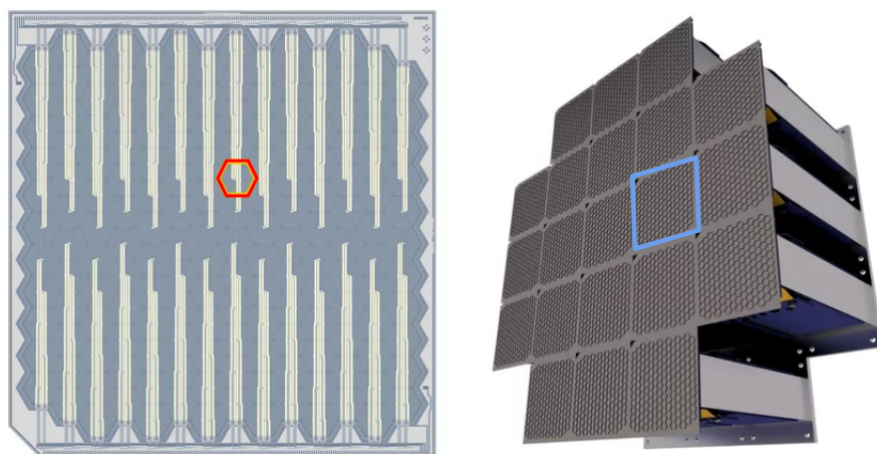


Figure 3.3: (Left) Depiction of a TRISTAN module consisting of 166 detector pixels, indicated by the red hexagon. (Right) The final TRISTAN detector comprises of 9 modules, with the option of 21 modules. A TRISTAN module is marked by the blue square. The figures are taken from [56].

4. KASSIOPEIA



KASSIOPEIA is a C++ based object-oriented software package designed for particle tracking simulations, developed by the KATRIN collaboration. Complicated physical processes and particle trajectories can be simulated efficiently while also considering complex geometries and electromagnetic fields. The KASSIOPEIA simulation framework provides reliable modules for the generation, tracking and termination of particles. Furthermore, it comes with precise electric and magnetic field calculation methods as well as different particle tracking options. All parts of the experimental set-up of the KATRIN experiment are included in the code and can be implemented in order to model various configurations to help understand physical processes and verify optimized settings for future experiments.

Besides the geometry and electromagnetic fields of the experimental set-up, the initial parameters of the particle and its termination conditions, are written in a XML configuration file. When the XML file is executed by KASSIOPEIA the output values are stored in a ROOT-file for further analysis.

In this chapter first the modules of KASSIOPEIA used in this work will be outlined. Then, the general structure of a simulation is explained.

4.1. Geometry

The `KGeoBag` package provides the geometrical components of the KATRIN experiment, important for the field computation, particle creation, tracking and interaction.

4.2. Electromagnetic Fields

`KEMField` [57, 58] provides a comprehensive number of field solving algorithms to calculate the complex electromagnetic fields at KATRIN. Axially symmetric normal conducting and superconducting coils induce, as a superposed total stray field, the main part of the magnetic fields. However, the earth magnetic compensation system (EMCS) is non-axially symmetric and has to be calculated differently.

4. KASSIOPEIA

Axially symmetric magnetic fields can be calculated by two different methods. The more accurate elliptic integral mode is applicable over a large spatial range but needs long calculation times. For small volumes, such as electrons propagating only inside the magnetic fluxtube, the faster Legendre polynomial expansion method is valid. The so-called zonal-harmonic expansion, calculates the field at any point inside the allowed volume as an expansion in Legendre polynomials P_n . The coefficients, or source points B_n^{cen} , are defined before and are valid as long the coil setup is unchanged. All field points within the allowed volume can be calculated by these source points. The magnetic field expressed by Legendre polynomials is defines as

$$B_r = -s \sum_{n=1}^{\infty} \frac{B_n^{cen}}{n+1} \left(\frac{\rho}{\rho_{cen}} \right)^n P_n'(u) \quad (4.1)$$

$$B_\varphi = 0 \quad (4.2)$$

$$B_z = \sum_{n=0}^{\infty} B_n^{cen} \left(\frac{\rho}{\rho_{cen}} \right)^n P_n(u) \quad (4.3)$$

with $u = \cos \theta$, $s = \sin \theta$ and ρ_{cen} the smallest distance between the source point and the coil. The important regions and parameters for the zonal-harmonic expansion method are illustrated in Fig. 4.1. In order to maximize the volume of validation, a high number of source points is used. A high number of source points entails a small ration ρ/ρ_{cen} and a faster convergence of the expansion, i.e. smaller computation time.

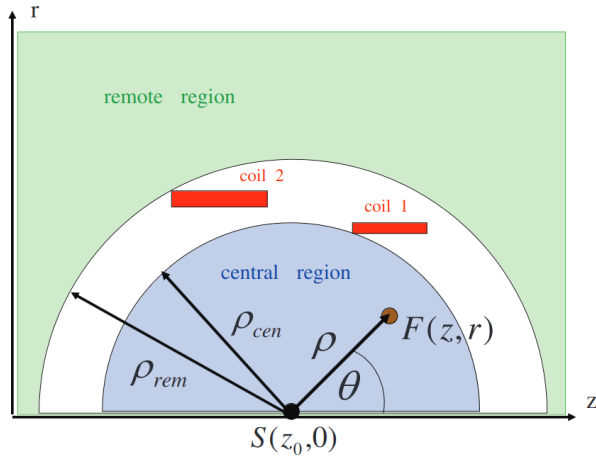


Figure 4.1: Depiction of the parameters for the zonal harmonic expansion. The induced magnetic field by coil 1 and coil 2 is approximated by the source point $S(z_0, 0)$. For any point $F(z, r)$ within the central region (blue) the magnetic field can be calculated accurately. For the zonal harmonic expansion the ratio between the smallest distance between the source point and the coil and the respective point to the source point is important. Points in the remote region can only be calculated by the remote Legendre polynomial expansion. This figure is taken from [58]

If the zonal harmonic expansion method is not applicable, as for non-axial symmetric magnetic fields, a three dimensional magnetic field calculation is necessary. This relies e.g. on the principles of the integrated Biot Savart law.

Electric Field Calculation

For the case of the electric field computation, only the electric potentials are defined at the beginning of the simulation. However, electric charge densities induce an electric field and therefore have to be computed first. Like for the magnetic field calculation, axially symmetric electric fields can be computed by the zonal harmonic expansion method.

4.3. Generation

The module `KAssiopeia PArticle GEnerator KPage` defines the input parameters for the generated particles. `KPage` comprises the starting energy, position, direction and time. Each input parameter can be defined individually. Particles can be created at a fixed position, homogeneously or isotropically distributed in a volume or on a surface. The energy of the generated particles can be fixed, uniformly or Gaussian distributed within a given range. There exist predefined generators, e.g. the krypton event generator, where the decay energies are defined with the corresponding intensity. The starting direction may be fixed or follow an isotropic emission from the surface. Lastly, particles can be created at a fixed time, with a constant rate or with a distribution following an exponential decay.

4.4. Propagation

The trajectory of any type of particle can be tracked with the package `KTrack`. It provides two main computation modes, shown schematically in Fig. 4.2. The first tracking mode calculates the exact trajectory of the particle by solving the Lorentz equation

$$\vec{p} = \gamma m \vec{v} \quad (4.4)$$

$$\vec{F} = \dot{\vec{p}} = q \left(\vec{E} + \vec{v} \times \vec{B} \right) . \quad (4.5)$$

The second tracking mode assumes adiabatic particle propagation and computes the guiding center motion of the particle

$$\dot{\vec{r}}_c = \frac{p_{\parallel}}{m\gamma} \cdot \hat{B}_c \quad (4.6)$$

$$\dot{p}_{\parallel} = -\frac{p_{\perp}^2}{2\gamma m |\vec{B}_c|} \left(\vec{\nabla} |\vec{B}_c| \right) + q \vec{E} \cdot \hat{B}_c \quad (4.7)$$

$$\dot{p}_{\perp} = \frac{p_{\perp} p_{\parallel}}{2\gamma m |\vec{B}_c|} \left(\vec{\nabla} |\vec{B}_c| \right) \cdot \hat{B}_c \quad (4.8)$$

4. KASSIOPEIA

with $\hat{B}_c = \vec{B}_c/|\vec{B}_c|$. Additionally, terms for the gyration and drift caused by the magnetron motion have to be included to the propagation terms. The approximated tracking mode has the advantage of being much faster than the exact tracking. Although its viable for most cases, the goal of this thesis is to study the non-adiabatic particle propagation in the MS, therefore demanding the exact tracking of the generated electrons. The particle trajectories of both tracking modes form ordinary differential equations and can be integrated numerically by Runge-Kutta integrators. For the presented work, the Runge-Kutta integrator with solution order 8 was chosen. Further, the number of calculated steps for the particle tracking can be defined with a fixed time control step, the step size, limits on the scattering probability, etc.. Finally, `KTrack` provides termination criteria for the particle track, like specific points reached along the KATRIN beamline, maximal number of steps, maximal path length, surface hit, etc.

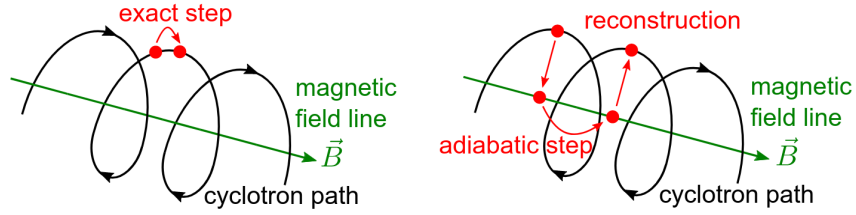


Figure 4.2: The two computation modes for the particle tracking. Left: The exact step is computed by solving the Lorentz equation. Right: The step is approximated by calculating the guiding center motion. This figure is taken from [59].

4.5. General Structure

Each simulations follows the same general structure. The simulation output is organized in four consecutive levels: step, track, event and run, shown schematically in Fig.4.3.

- **Step**

The lowest level of each simulation is a step. It calculates the transformation from an initial to a final state of the simulated particle over a small period of time and space. By solving the equation of motion and considering interactions between the particle and electromagnetic fields the particle's propagation is achieved in the defined geometry. For each step it is also checked whether the particle's parameters fulfill the set boundary and termination conditions, such as crossing specific positions in space, the maximum path length covered in the main spectrometer or the number of maximal allowed steps and/or turns.

- **Track**

All combined steps of a particle from its point of creation to its point of termination form a track. The track output stores only initial and final parameters, besides e.g. the total

number of steps and total length of the track. The particles are initialized with an events generator, following defined sets of parameters, such as the particle's position, angular distribution and energy. If one termination conditions is met the particle track is stopped and stored. Several termination conditions can be included in the configuration file. Most commonly, these are spacial boundary conditions or a maximum amount of steps, length or turns.

- **Event**

Causally connected tracks are summarized as an event. Each event starts with a primary track corresponding to the primary particle created by the generator. Via interactions or decays new particles can be created, forming secondary tracks. Additionally specific generators which create particles from a radioactive decay sequence produce causally related tracks that form one event.

- **Run** Lastly, a run is composed of all events that were simulated and represents one execution of a fixed experimental set-up.

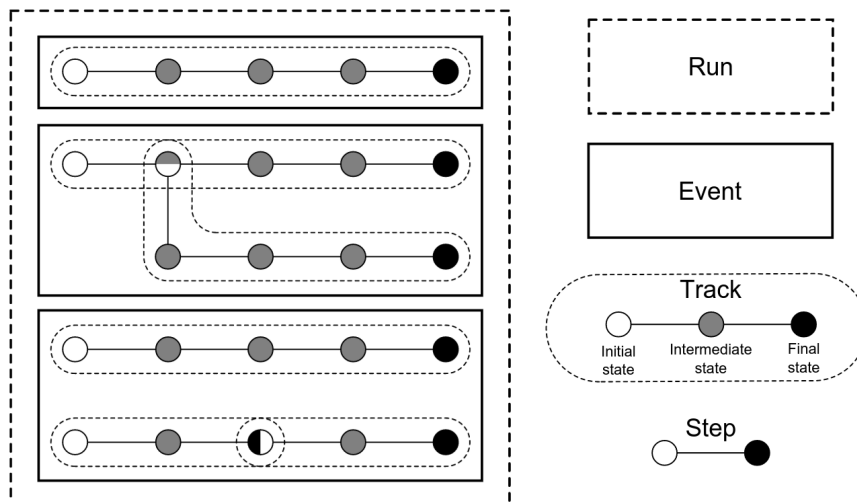


Figure 4.3: Schematic depiction of the constituents for a simulated run with 3 events and 6 tracks. Each track starts with an initial state (white) and ends with a final state (black). During the propagation new tracks can be formed via interaction processes (event 2) or a radioactive decay (event 3). All simulated tracks are combined to an event. This figure is taken from [59].

5. Transmission Study

Sterile neutrinos, as right-handed counterparts to the left-handed 'active' SM neutrinos, do not interact with any of the SM fundamental forces. However, it is assumed that active-to-sterile mixing occurs, enabling the experimental access to the sterile neutrino parameters indirectly via the kinematics of the β -decay. As explained in Ch. 2, the sterile neutrino would manifest itself in a kink-like signal in the β -electron energy spectrum, located at $E_0 - m_{\nu_s}$ with an amplitude that scales with the mixing parameter $\sin^2 \theta$.

A previous study in 2015 has shown that for the current KATRIN setup and the full KATRIN source strength together with the new TRISTAN detector system, the targeted sensitivity on the active-to-sterile mixing parameter of $\sin^2 \theta < 10^{-6}$ can be achieved after three years of data taking [49]. On this grounds, the TRISTAN project aims to search for a sterile neutrino in the keV-mass range with a high sensitivity. This is achieved by extending the measured energy range by lowering the retarding potential (qU) in the MS.

As the qU stops all electrons with less energy, it sets a limit to how deep one can look into the electron energy spectrum, $E_0 - qU$. Remembering that the position of the sterile neutrino kink is located at $E_0 - m_{\nu_s}$, the accessible sterile neutrino mass range is defined as

$$m_{\nu_s} \in [0, E_0 - qU]. \quad (5.1)$$

The impact of the retarding potential on the keV-scale sterile sensitivity is illustrated in Fig. 5.1. For a high retarding voltage of 13.5 kV, indicated by the black arrow, the accessible mass range is limited to $m_{\nu_s} \in [0, 5.074]$ keV. When decreasing the retarding voltage, one is able to scan deeper into the β -electrons energy spectrum, which is highlighted by the red and blue arrows. Thus, this translates into a wider accessible mass range on the sterile neutrino mass. For consistency, the column density for each of the three settings was chosen such that the rate of 100 kcps at the detector is constant. It can be inferred, that minimizing the retarding potential, maximizes the accessible parameter space for the sterile neutrino mass parameter m_{ν_s} , and is therefore favored.

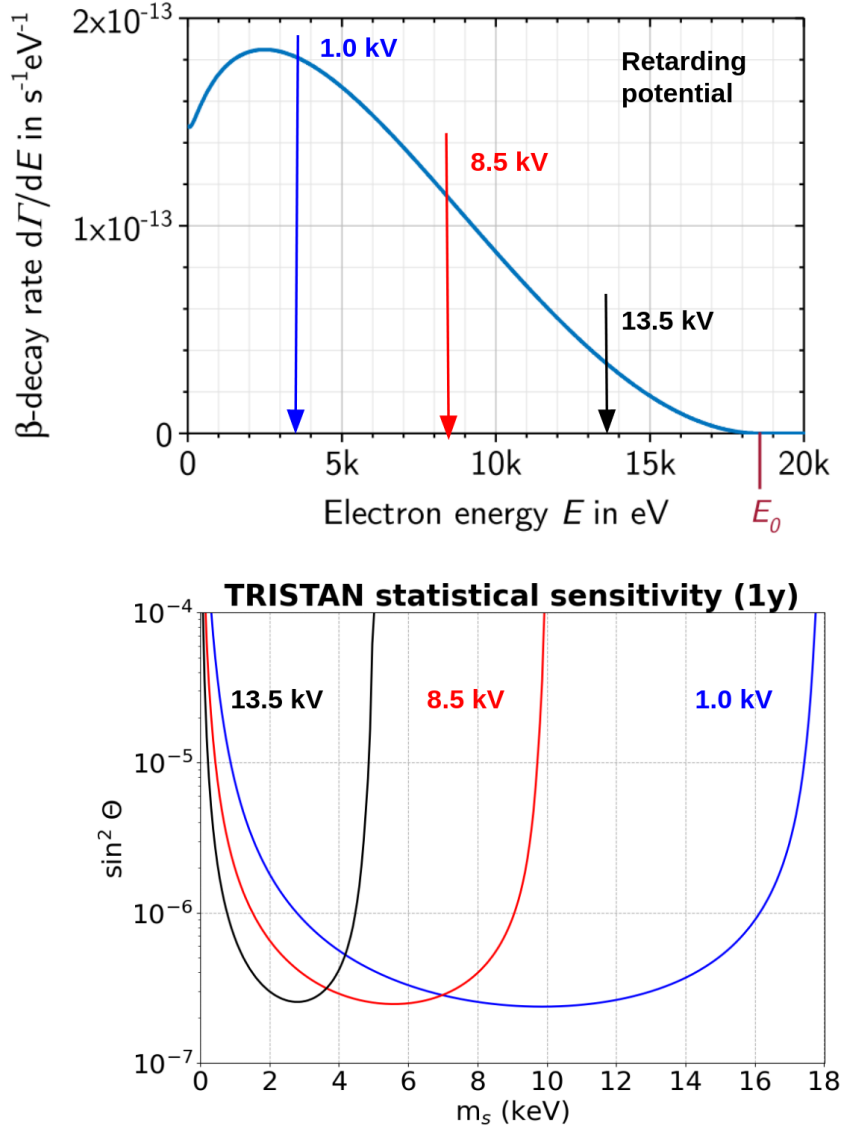


Figure 5.1: (Top) Differential β -electron energy spectrum corresponding to the decay rate of a single tritium nucleus [60]. Indicated are the endpoint energy of $E_0 = 18.574$ keV and the retarding potentials of $qU = 13.5, 8.5, 1.0$ kV.

(Bottom) Sensitivity for the sterile neutrino parameter space considering the three respective retarding voltages. For lower retarding potentials, one is able to look deeper into the β -electrons energy spectrum. Thus, the accessible sterile mass range is larger. For consistency, the constant rate at the detector of 100 kcps was chosen for all three cases. Therefore, only the impact of the retarding potential is shown. Figure courtesy of A.Onillon.

However, lowering the retarding potential also comes with new challenges, mainly:

1. The rate at the detector increases drastically when the retarding potential is lowered and exceeds the current limit of the FPD. To handle the high rates the new detector system TRISTAN is currently under development, designed for a maximum rate of 100 kcps per pixel [52].
2. Lowering the retarding potential leads to electrons with higher energy surplus with respect to the retarding potential inside the MS.

$$E_{surplus} = E_e - qU_{ret} \quad (5.2)$$

High energy surplus potentially leads to chaotic - non-adiabtic, electron propagation in the MS, resulting in an uncontrollable transmission loss. Due to the very small active-to-sterile mixing amplitude ($< \text{ppm}$), a very high control of systematic effects and associated uncertainties is mandatory [52]. A transmission loss of up to a few percent would be unacceptable.

The transmission probability of the electron as a function of the (surplus-)energy for the 70% KATRIN beamline setting together with the current maximal LFCS setting is shown in Fig. 5.2. At approximately 0 keV, the transmission starts to deviate from 100%, with up to 97.9% of transmission loss at $E = 18.6 \text{ keV}$. Consequently, this sets a lower limit to qU and hence an upper limit to the accessible sterile neutrino mass of $m_{\nu_s} < 5.8 \text{ keV}$.

5. Transmission Study

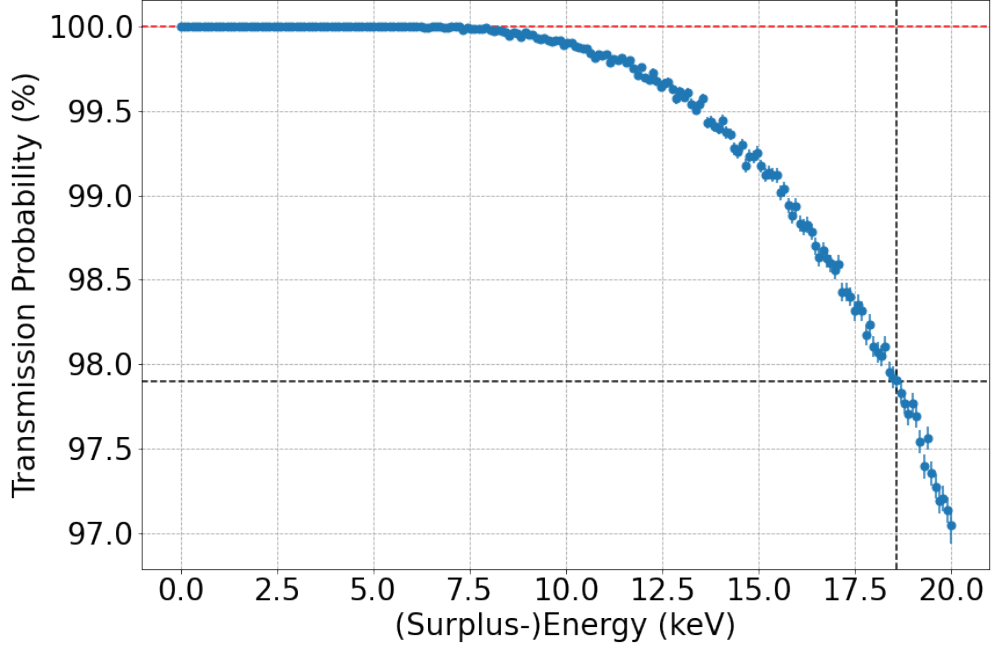


Figure 5.2: Simulated transmission probability for electrons of $E = 0–20$ keV with the KATRIN 70% beamline setting together with the current maximal LFCS setting. A total of 10 million electrons were generated at the PS2 magnet with an uniform distribution of the initial kinetic energy between $0 – 20$ keV. The initial polar radius is distributed uniformly in r^2 between 0 and r_{max} . To mimic the isotropic source distribution, the initial polar angle towards the guiding magnetic field line θ is uniformly distributed in $\cos(\theta)$ between 0 and θ_{max} . The error bars represent the statistical uncertainty. The transmission loss starts to manifest itself at ~ 5.8 keV and reach 97.9% at 18.6 keV.

The statistical uncertainty of the expected transmission probability $T = t/n$ follows a binomial distribution, and is defined as [61]:

$$\sigma_T = \sqrt{\frac{(t+1)(t+2)}{(n+2)(n+3)} - \frac{(t+1)^2}{(n+2)^2}}. \quad (5.3)$$

with n the total number of electrons and t the amount of transmitted electrons.

The statistical uncertainty σ_T associated to the transmission probability T according to Eq. 5.3, as a function of the total number of generated electrons, is shown in Fig. 5.3. It shows, that the required total number of electrons increases by a few orders of magnitude for a transmission probability of only $T = 97.0\%$ with respect to the full transmission, to achieve the same statistical uncertainty. Even for an almost full transmission of 99.999%, at least 10 times more electrons are needed to obtain a better statistical uncertainty. The total number of required electrons in order to reach a statistical uncertainty for a specific transmission probability is shown in Fig. 5.4.

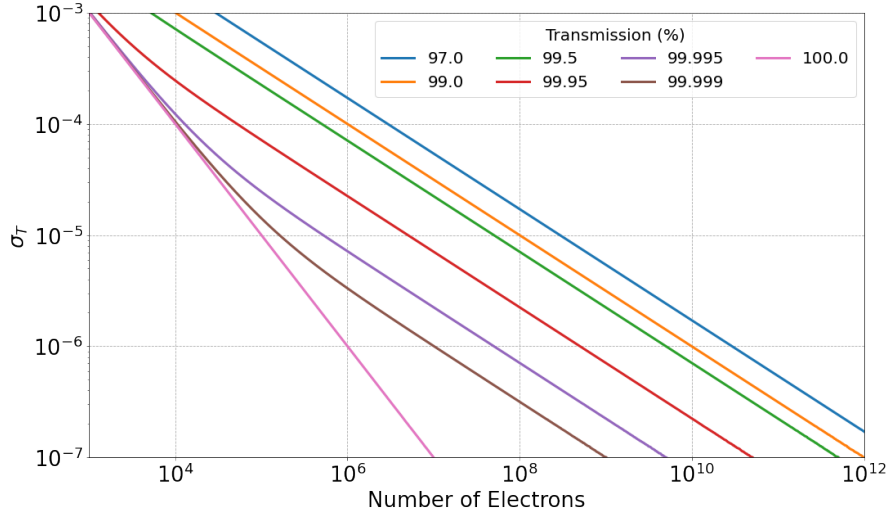


Figure 5.3: Statistical uncertainty in relation to the total number of electrons for different transmission probabilities.

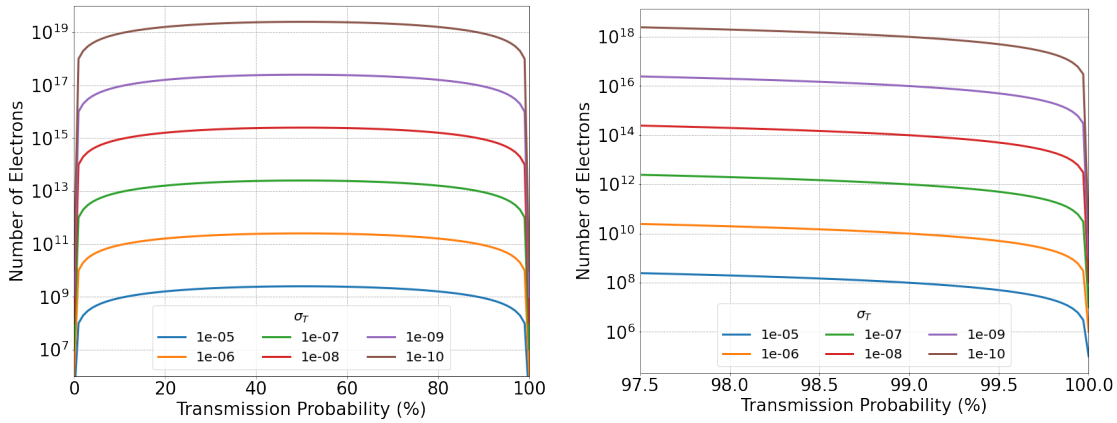


Figure 5.4: The total number of electrons required to achieve a statistical uncertainty for a specific transmission probability. (Right) Zoom into the relevant range of the transmission probability for this study.

This chapter deals with the transmission study for electrons with energy surplus of several keV and the impact of non-adiabatic behavior by employing the simulation framework KASSIOPEIA. Important initial parameters of the electrons, when entering the MS, are studied in order to conclude the transmission probability. Further, the influence of the applied magnetic fields are studied and different settings for the LFCS and detector magnet are tested. Possible settings for the setup will be outlined, so that the retarding potential can be lowered as much as possible by keeping the non-adiabatic effect subdominant.

5.1. Adiabatic Electron Transport

Electrons, as charged particles, propagate in the presence of electromagnetic fields (\vec{E}, \vec{B}) in cyclotron motion around the guiding magnetic field line caused by the Lorenz force

$$\vec{F}_L = e \cdot (\vec{E} + \vec{v} \times \vec{B}) \quad (5.4)$$

with e the electron's electric charge and \vec{v} its velocity. The radius of the cyclotron motion is defined as

$$r_{cyc} = \frac{\gamma_0 m_e v_{\perp}}{eB} \quad (5.5)$$

with $B = |\vec{B}|$ the magnetic field strength, $\gamma_0 = 1 + \frac{E_{\perp}}{m_e c^2}$ the relativistic correction factor with $E_{\perp} = E \cdot \sin \theta$ the transversal component of the kinetic energy. Eq. 5.5 shows the direct relation between the size of the cyclotron radius and the kinetic energy E as well as the polar angle θ of the electron. The higher the kinetic energy and/or the polar angle, the larger the cyclotron radius. This dependence becomes important for the adiabatic electron transmission. In order to ensure the adiabatic motion, the field gradients must satisfy

$$\vec{\nabla} B = \frac{\Delta B}{B} \ll 1 \quad \text{and} \quad \vec{\nabla} E = \frac{\Delta E}{E} \ll 1. \quad (5.6)$$

has to be small within one cyclotron length

$$l_{cyc} = 2\pi \frac{v_{\parallel}}{\omega_{cyc}} = 2\pi \frac{\gamma_0 m_e}{eB} v_{\parallel}. \quad (5.7)$$

The second condition for adiabatic electron transmission is the transformation between the transversal and longitudinal component of the kinematic energy. The ratio of the transversal kinetic energy and the magnetic field strength has to stay constant at any point along the electrons trajectory

$$\frac{E_{\perp}^i}{B^i} = \frac{E_{\perp}^j}{B^j}. \quad (5.8)$$

If the before mentioned conditions are fulfilled, to first order the magnetic moment is a good measure of the adiabaticity.

$$\gamma_0 \mu = \frac{\gamma_0 + 1}{2\gamma_0} \cdot \frac{E_{\perp}}{B} \quad (5.9)$$

With the non-relativistic approximation ($\gamma_0 = 1$)

$$\mu \approx \frac{E_{\perp}}{B}. \quad (5.10)$$

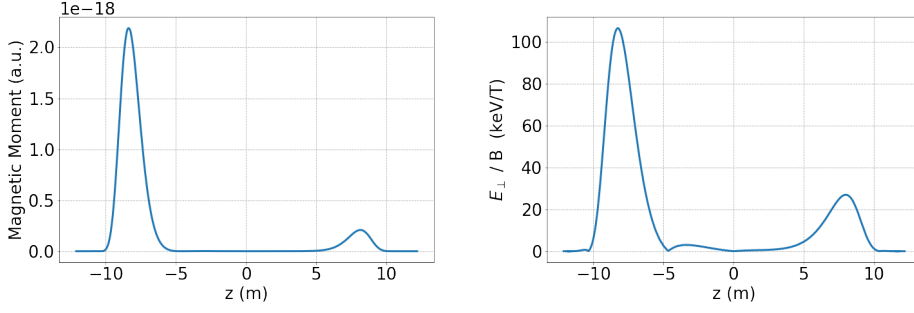


Figure 5.5: The exact and approximated orbital magnetic moment of an electron created with a kinetic energy $E_{\text{kin}} = 0.5 \text{ keV}$, an initial radial position $r_i = 39.93 \text{ mm}$ and an initial polar angle of $\theta = 0 \text{ deg}$, obtained with a dedicated KASSIOPEIA simulation.

Fig. 5.5 shows that the orbital magnetic moment increases where the magnetic field strength changes rapidly, i.e. at the entrance and exit of the MS. At first order, the exact and approximated magnetic moment exhibit close shapes and the approximation is valid.

Along an adiabatic electron track, the change of the polar angle to the guiding magnetic field line is defined as

$$\frac{\sin^2 \theta_1}{B_1} = \frac{\sin^2 \theta_2}{B_2}. \quad (5.11)$$

According to Eq. 5.11 the polar angle towards the guiding magnetic field line is proportional to the magnetic field strength. This relation is shown on Fig. 5.6. The polar angle increases much faster and greater for a larger initial value for an increasing magnetic field strength.

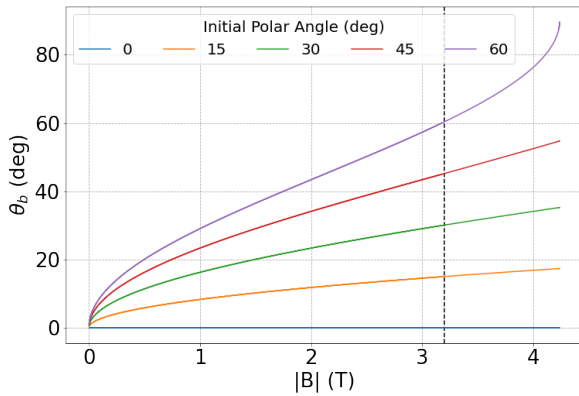


Figure 5.6: Increase of the polar angle versus the magnetic field strength for different initial polar angles. The higher the initial value the faster and greater the increase. All electrons are created at the PS2 magnet with $B_{PS2} = 3.2 \text{ T}$, indicated by the vertical dashed line. The result was obtained for electrons starting with the same kinetic energy and with no radial distance to the symmetry axis.

Besides the high energy surplus and the high field gradient, the adiabatic transport depends on the propagation path, the curvature of the magnetic field line and the length of the low magnetic field region. It shows clearly, that the higher the energy surplus, the more sensitive the particle transmission gets towards the other parameters.

5.2. Simulation Setting

The aim of the simulations, presented in this thesis, is to study the impact of several parameters on the electron transmission. Therefore, different initial parameters: radial position, angular and energy distribution as well as the magnetic field settings for the detector magnet and inside the MS, have been tested. The geometry of the DPS, CPS, PS, MS and detector are included in the configuration file. Magnetic fields strengths are defined for: RW, WGTS, DPS coils, CPS, PS1/2, PCH. Further, the inhomogeneities of the magnetic field in the MS, caused by the earth's magnetic field, are compensated by the EMCS. In the simulations only its z-component was included.

The electrons were exactly tracked with a cyclotron step size of $1/40$. If the magnetic field strength gets small, the cyclotron radius increases, see Eq. 5.5. Hence, the cyclotron step size is increased as well, as it scales with $\propto 1/B$. The same dependence holds for an increasing magnetic field. In Fig. 5.7 this relation is shown for the 70 % KATRIN beamline setting with the max LFCS setting of 20G.

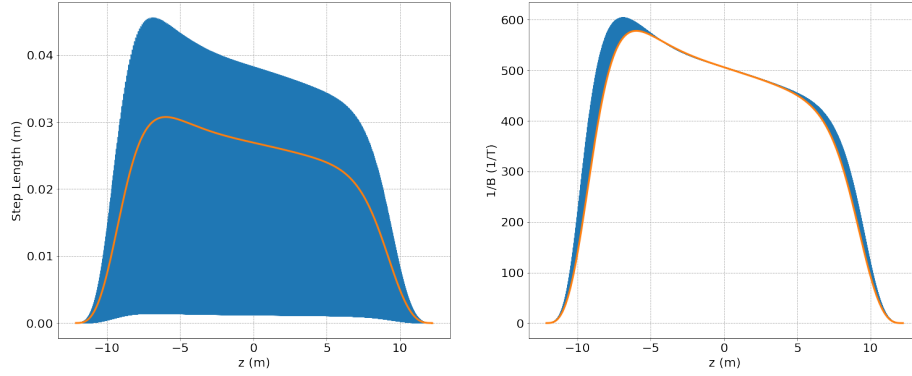


Figure 5.7: Illustration of the relation between the magnetic field strength and the step size controlled via the cyclotron radius. The blue shaded are correspond to simulated electrons created with an energy uniformly distributed between 0 – 20 keV and within the visible fluxtube radius at the source 0 – 39.93 mm with angles between 0 – θ_{\max} . The orange line represents a specific electron, generated on-axis with $E_{\text{kin}} = 10$ keV and $\theta = 0$.

5.2. Simulation Setting

In total 15 different magnetic field configurations were simulated. The influence of the detector magnet B_{det} was tested for 5 different settings: $B_{\text{det}} = 2.52, 1.70, 1.00, 0.70, 0.50$ T. Further, the impact of the magnetic field strength inside the MS, B_{MS} , was tested. The current max LFCS setting of 20 G was chosen as reference setting. The field strength was increased by implementing a scale factor, the so-called turnfactor. For each of the settings 10 million electrons were generated. The initial parameters for the respective setting are summarized in Tab. 5.1. Detailed information for all implemented slow control parameters can be found in Tab. A.2.

Parameter	Value	Dependent Parameter	Distribution
B_{PS2}	3.2 T		
B_{pch}	4.2 T		
B_{MS}	20 G		linear, turnfactor = 1, 1.5, 2
B_{det}	2.52 T	0 - r_{max} (mm) 0 - 39.93	uniform in r^2
	1.70 T	0 - 32.79	
	1.00 T	0 - 25.15	
	0.70 T	0 - 21.05	
	0.50 T	0 - 17.78	
$E_{\text{kin},i}$	0 - 20 keV		uniform
θ_i	0 - 60.79 deg		uniform in $\cos(\theta_i)$

Table 5.1: Summary of the important initial simulation parameters for the studied scenarios.

5. Transmission Study

5.2.1. Generation

For the transmission study, the electrons are generated in front of the MS at the position of the pre-spectrometer magnet 2 (PS2) at $z_{\text{start}} = -12.104$ m. The electron's initial kinetic energy is distributed uniformly between 0–20 keV. Other parameters which are defined at the generation are the radial distribution and the polar angle to the guiding magnetic field line θ . To satisfy the physical nature of the source the radial position is uniformly distributed in r^2 , i.e. uniform in the circular area of the source.

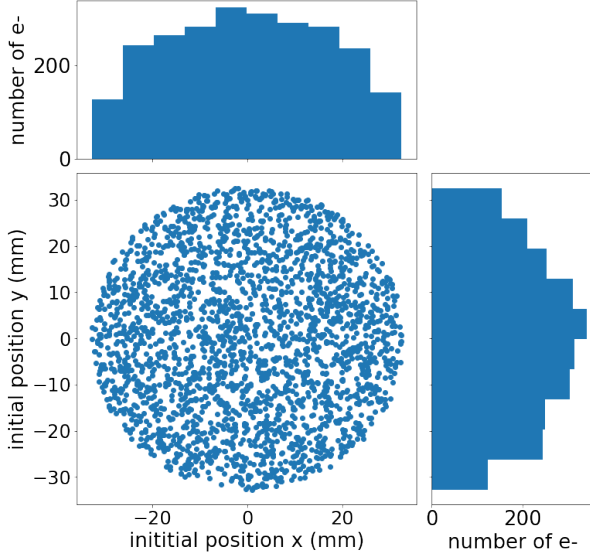


Figure 5.8: Illustration of the position distribution of the electrons along the x-y axis for a small survey of 0.5 million electrons. The electrons are generated at the PS2 magnet position using a uniform distribution in r^2 , i.e. uniform in the circular area at the source.

The polar angle θ is distributed uniformly in $\cos(\theta)$ as the electrons leave the source isotropically

$$\frac{\Delta\Omega}{4\pi} = \frac{1 - \cos(\theta)}{2}. \quad (5.12)$$

Due to the magnetic mirror effect resulting from the strong magnetic field of the pinch magnet, only electrons with an angle smaller than θ_{max} are generated. A further cut on the θ -angle has been applied in the analysis to take into account the radial dependence of the magnetic fields $B(r)$ and therefore the radial dependent maximal $\theta_{\text{max}}(r)$.

Considering the physical nature of the radial and angular parameters in the generation, results in a statistical bias. More electrons for larger radii and polar angle are generated. This bias is incorporated in the following analysis.

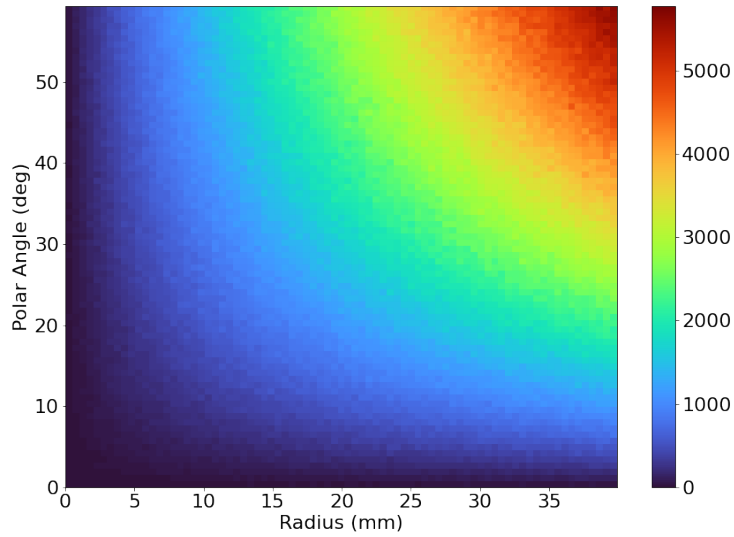


Figure 5.9: Illustration of the source distribution radial-angular plane for the 70 % KATRIN beamline setting together with the max LFCS configuration and 10 million electrons. Electrons with large radius and polar angle exhibit a higher probability as the electrons are generated following a uniform distribution in r^2 and isotropic distribution in θ .

5.2.2. Terminators

Along the propagation of the electrons, several termination condition are checked for each step. If one of these conditions is met, the track is terminated. Four different terminators were included for this study and are illustrated in Fig. 5.10.

1. **transmitted:** the electron is successfully transmitted from the source, through the MS, to the detector at $z_{max} = 12.2$ m. Most electrons are propagated from the source to the detector directly, although electrons can also go back and forth inside the MS until they reach the determination condition.
2. **reflected:** the electron entered the MS but underwent at least one sign change of it's momentum with respect to the propagation direction. This can happen due to the random change of the polar angle towards the guiding magnetic field line when the track becomes non-adiabatic. If the electron passes $z_{min} = -12.11$ m, it is terminated and labeled as reflected back to the source.
3. **trapped:** the polar angle towards the guiding magnetic field line changed randomly and the electron transverses the MS back and forth non-adiabatically. For the simulations the track of an electron is terminated after a maximum path length of $MPL = 500$ km is reached.
4. **scattered:** the electron left the guiding magnetic field line and hit the MS wall, i.e. the radial position of the electron track reached $r_{max} = 5$ m with respect to the symmetry axis z .

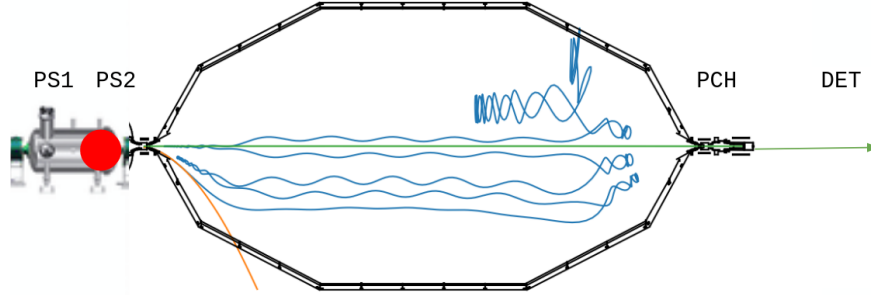


Figure 5.10: Depiction of four different electron paths inside the MS. All electrons are generated at the position of the PS2 magnet, indicated by the red circle. They are then propagated through the MS, where there are different possibilities how the electron track can be terminated. The perfect transmission is shown in green, where the electron is transmitted straight to the detector. Due to a non-adiabatic change of the polar angle, the direction of the electron can be flipped. Hence, the electron is reflected back to the source. Electrons can also leave the guiding magnetic field line and scatter with the MS walls and are then absorbed. Shown in blue is the scenario where the electron goes back and forth and eventually moves chaotically through the MS.

The transmitted and reflected electrons possess different total length. As the reflected electrons enter the MS, and return to the source, they cover more distance than the electrons that are directly transmitted to the detector. Fig. 5.11 displays that the electrons get reflected close to the pinch magnet, where the impact of the stray field is also the greatest. While the magnetic field strength increases by a few orders of magnitude, the polar angle also becomes greater. This can lead to the reflection of the electrons.

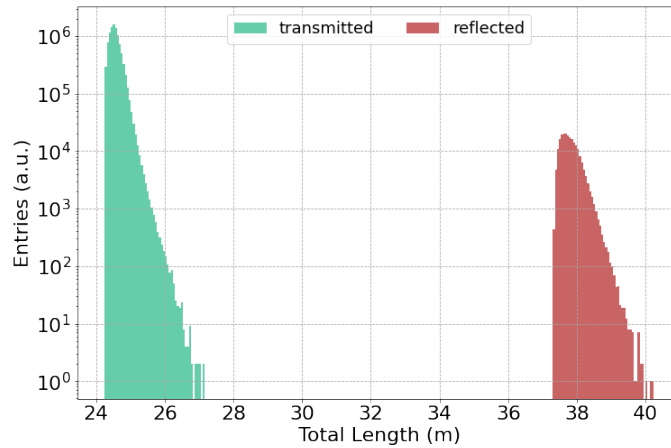


Figure 5.11: Total length distribution for transmitted and reflected electrons for the 70% KA-TRIN beamline setting together with the max LFCS configuration. Reflected electrons cover a greater distance than directly transmitted electrons.

In principle, the total length covered by electrons can be used as a cut for sorting transmitted and reflected electrons. However, if the setup becomes more complicated and the electron reflection due to non-adiabatic motion becomes more dominant throughout the MS, a small value of the total length is not sufficient to determine whether an electron was transmitted or not.

5. Transmission Study

As the scattering probability is negligibly small, scattering between electrons and residual gas atoms (e.g. hydrogen, H₂) is not taken into account in the simulations. The energy-dependent inelastic scattering cross section of electrons and H₂ is defined as

$$\sigma_{inel} = \frac{4\pi a_0^2}{k_0^2} \left[1.5487 \cdot \ln(k_0^2) + 2.4036 + \frac{\gamma_{tot}}{k_0^2} \right] \quad (5.13)$$

with a_0 the Bohr radius, k_0^2 the incident electron energy in rydbergs and γ_{tot} the relativistic correction [62]. Together with the equation for the scattering probability

$$P_{scattering} = 1 - \exp \left[- \left(l \cdot \frac{p}{k_B T} \sigma_{inel} \right) \right] \quad (5.14)$$

this results in a $4.22 \times 10^{-5} \%$ chance of scattering for an electron possessing an initial kinetic energy of $E_{kin,i} = 20 \text{ keV}$ and $2.64 \times 10^{-3} \%$ for a low energetic electron of $E_{kin,i} = 0.1 \text{ keV}$.

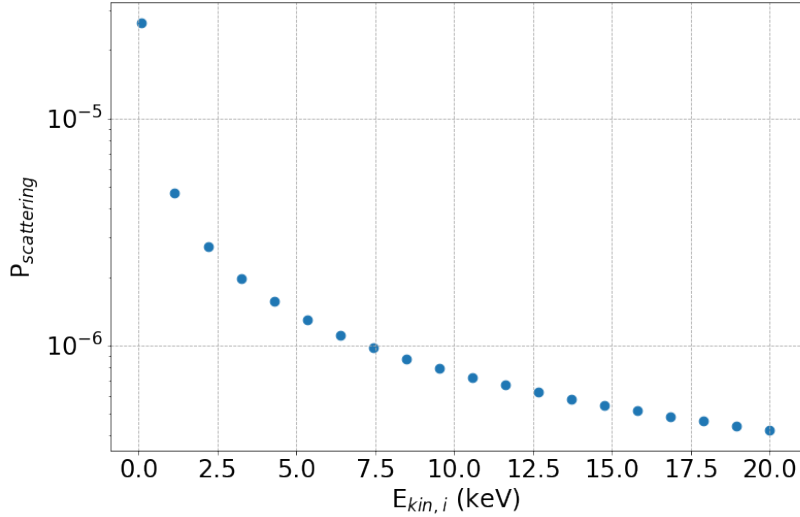


Figure 5.12: Inelastic scattering probability for electrons with residual gas atoms inside the MS. It shows, the higher the initial kinetic energy of the electron entering the MS, the lower the scattering probability. Nevertheless, the scattering probability for the considered energy range of the electrons is in the order of $10^{-3} - 10^{-5} \%$ and hence can be neglected in the study.

5.2.3. Zonal Harmonic Solver

At the beginning of this transmission study, only the zonal harmonic solver (ZH 1) for the magnetic field calculation was available in the KASSIOPEIA code. For ZH 1, the field is calculated by central and remote points defined for the zonal-harmonic expansion, and directly by the elliptic integral mode (see Ch. 4). Due to the large computation time, two new zonal harmonic solvers (ZH 2, ZH 3) have been implemented by KASSIOPEIA developers. As the distance of the electron's trajectories to the central source points is considered to be small for the studied settings, the magnetic field calculation conducted entirely via central points is assumed to be valid. Therefore, ZH 2 and ZH 3 are defined as such and the CPU time was improved drastically. For ZH 3, additional upgrades in the KEMField part were included. During the study, I participated in benchmarking the new ZH solvers.

All three ZH solvers can be included in the XML-file by defining the number of the respective zonal harmonic solver which should be used for the field calculation by:

```
<external_define name="use_zh_magnetic" value=" "/>
<!-- value = 1, 2, 3 -->
```

The new zonal harmonic solvers have been tested for several scenarios to evaluate their impact on the computing time and on the calculated transmission probability. For this benchmark four scenarios have been defined as listed in Tab. 5.2. Identical simulation settings, except for the initial parameters of the source have been used. For each setting, a total of $N = 5 \times 10^6$ electrons with a kinetic energy of $E_{\text{kin}} = 18 \text{ keV}$ were generated. All four settings were divided into the same number simulation batches with identical seed, containing the identical number of generated electrons. The statistical uncertainties are thus fully correlated and any difference obtained on the computed transmission probability between two solvers are a systematic effect.

Scenario	Radius (mm)	Radius Distribution	Polar Angle (deg)	Polar Angle Distribution
1	36.7	fix	59	fix
2	36.7	fix	59	spherical
3	30.0	fix	59	spherical
4	36.7	uniform	59	fix

Table 5.2: Initial source parameters and their distribution for the four scenarios.

The electron motion strongly depends on the magnetic field gradient. In Fig. 5.13 the magnetic field strength, the relative ratio and the field gradient for ZH 1, 2 and 3 for scenario 1 is shown. The approximated magnetic field of ZH 3 is by a factor of 3.6 closer to the exact field calculation of ZH 1, then ZH 2. Although, the small difference of the magnetic field strength of up to 2.2×10^{-4} (ZH 1 - 2) and 6.1×10^{-5} (ZH 1 - 3), the transmission probability is not affected, as the field gradient stays constant along the symmetry axis. This enables the use of the much faster magnetic ZH solvers 2, 3 by still obtaining equal simulation results.

5. Transmission Study

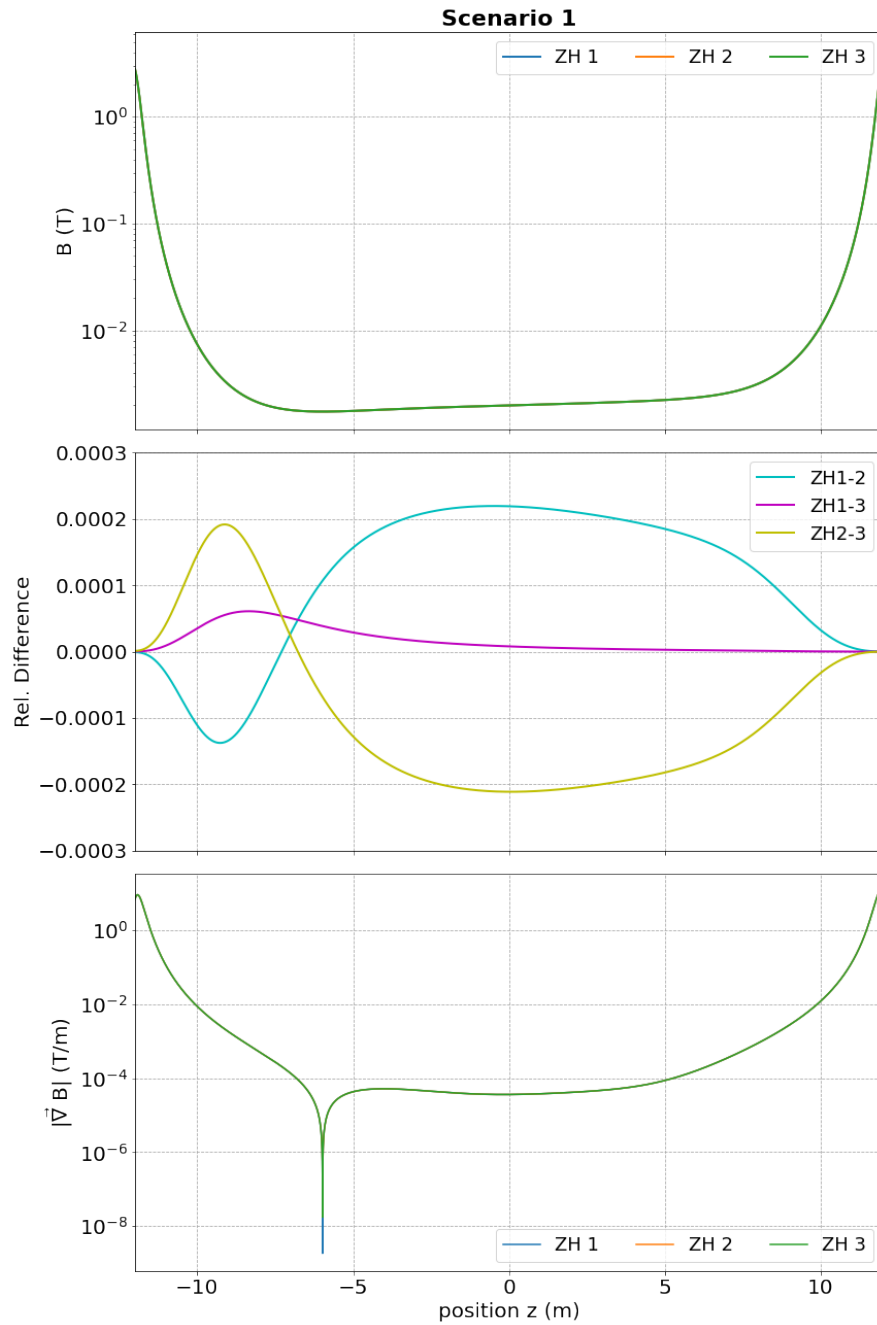


Figure 5.13: Illustration of the magnetic field strength inside the MS for ZH 1,2 and 3 for the scenario 1. The relative difference between the ZH solvers is less than 2.2×10^{-4} . More importantly, the magnetic field gradient does not change along the symmetry axis inside the MS. Therefore, small differences in the magnetic fields are expected to have a minor impact on the transmission probability.

Indeed, the results for ZH solver 1, 2 and 3 for all four scenarios are in good agreement. The transmission probability with the statistical uncertainty in percent is listed in Tab 5.3.

	Scenario 1	Scenario 2	Scenario 3	Scenario 4
ZH 1	64.97 ± 0.02	98.14 ± 0.01	99.53 ± 0.003	89.36 ± 0.01
ZH 2	65.09 ± 0.02	98.15 ± 0.01	99.54 ± 0.003	89.42 ± 0.01
ZH 3	64.96 ± 0.07	98.14 ± 0.02	99.55 ± 0.01	89.37 ± 0.04

Table 5.3: Transmission probability with the statistical uncertainty in percent for ZH 1, ZH 2 and ZH 3 for all four scenarios. The results are in good agreement. For each scenario and ZH solver, the 5×10^6 electrons were generated and the same seed was used. The statistical uncertainties are thus fully correlated and any differences obtained on the computed transmission probability between two solvers are a systematic effect.

The CPU time between ZH 1 and 2 is improved approximately by a factor of 25. However, ZH 2 and 3 have been compared in more detail. In Fig. 5.14, the CPU time per electron is shown for all four scenarios for the new ZH solvers. ZH 2 is constantly 11.25 times faster than ZH 3. In the simulation profile it became obvious that this difference results from parts of the KEMField calculation.

Interestingly, in the CPU time per electron one can see the time distribution for the transmitted and reflected electrons. In each case, the first peak incorporates the directly transmitted electrons. The tail corresponds to electrons that follow outer magnetic field lines as well as electrons that underwent a turn in the MS and are then transmitted to the detector. The second peak shows all electrons that were reflected inside the MS and transverse a greater length. The tail of the reflected electrons stems from the same arguments.

Based on this analysis, the use of ZH 2 and ZH 3 is valid for the considered scenarios in this thesis. Therefore, for all following simulations the magnetic fields were calculated with the ZH 2 solver, obtaining the fastest simulations.

5. Transmission Study

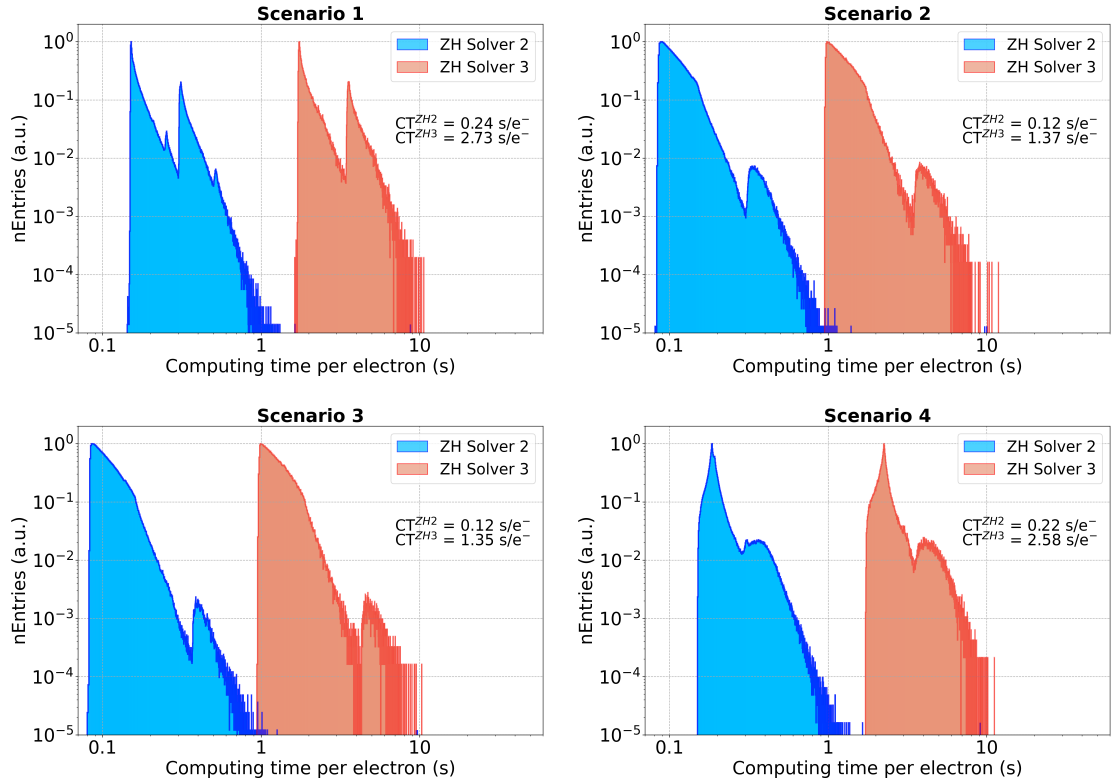


Figure 5.14: Computation time per electron for ZH 2 and ZH 3 for each of the four scenarios. For all scenarios, the ZH 2 solver is found to be 11.25 times faster than ZH 3. As the same but shifted shape indicates, the transmission probabilities are in good agreement for all scenarios within the statistical uncertainty as shown in Tab. 5.3.

5.2.4. Decreased Detector Magnetic Field

For a fixed detector wafer radius r_{det} and a constant magnetic field at the point of generation B_i , a lower magnetic field at the detector decreases the initial radius r_i of the electrons entering the MS, through the conservation of the magnetic flux (see Eq. 2.10).

$$r_i = \sqrt{\frac{B_{\text{det}}}{B_i}} \cdot r_{\text{det}} \quad (5.15)$$

For this study a detector magnetic field strength of the current setting of $B_{\text{det}} = 2.52$ T as well as $B_{\text{det}} = 1.70, 1.00, 0.70, 0.50$ T are investigated.

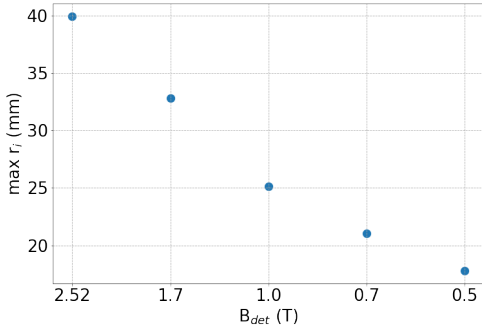


Figure 5.15: Maximal initial radii for the different detector magnetic field settings considered. The detector wafer radius is constant (45mm), same as the initial magnetic field strength at the PS2 magnet ($B_i = 3.2$ T).

The alternative B_{det} considered for this study, also decreases the radius of the visible fluxtube inside the MS, as shown in Fig. 5.17, effectively reducing the distance of the signal electron trajectories to the MS symmetry axis, which improves the adiabatic transmission. Lowering the detector magnetic field also effects the polar angle, due to the radial dependence of the magnetic field strength $B(r)$ at the point of generation B_i , and the maximal magnetic field strength at the pinch magnet B_{pch} .

$$\theta_{\max}(r_i, r_f) = \sin^{-1} \left(\sqrt{\frac{B_i(r_i)}{B_{\text{pch}}(r_f)}} \right) \quad (5.16)$$

With a dedicated KASSIOPEIA simulation of 10.000 electrons uniformly distributed between $r_i = 0$ and the respective maximal initial radius $r_{i,\max}$, the radial dependence for the initial and maximal magnetic field strength was determined for each scenario, as shown in Fig. 5.16. With Eq. 5.16, the maximal value for the polar angle, before the electrons get magnetically reflected at the pinch magnet, was calculated. In order to correct for the radial dependence of the maximal polar angle $\theta_{\max} = f(r)$ a cut for all simulated electrons was performed. By taking every tenth initial radial position into account, the cut is based on a second order polynomial fit

$$f(r) = a \cdot r^2 + b \cdot r + c. \quad (5.17)$$

5. Transmission Study

To account for the uncertainties associated with the fit parameters, a correction factor is introduced. The correction factor depends on the residual obtained by the ratio of the true and fitted value for $\theta_{max}(r)$. By multiplying the fit function with the minimum residual value, the cut for the simulated electrons is further improved. The fit parameters for all scenarios can be found in Tab. A.4.

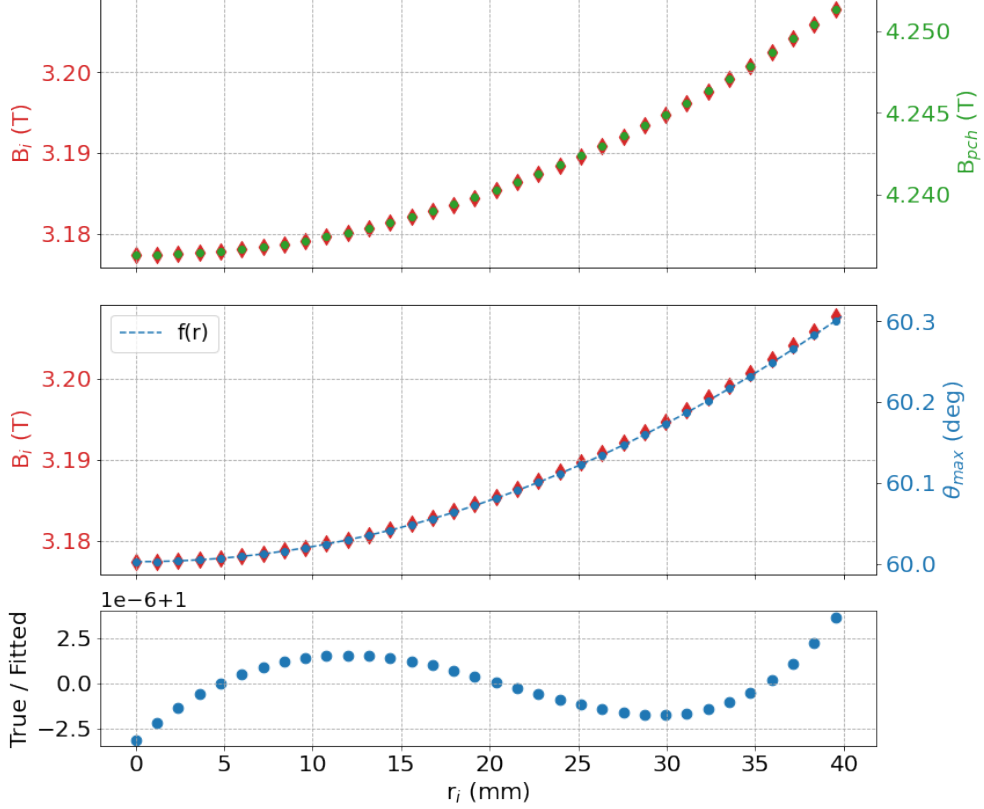


Figure 5.16: This figure shows the determination of the radial dependence of the magnetic field strength and the resulting cut function for $\theta_{max}(r)$ for the simulated electrons for the reference KATRIN setting, i.e. 70 % beamline setting together with the max LFCS setting.

(Top) Through the use of a dedicated KASSIOPEIA simulation, the radial dependence of the initial and maximal magnetic field strength is determined. In total 10.000 electrons are uniformly generated between $r_i = 0$ and the respective maximal initial radius $r_{i,max}$.

(Middle) With Eq. 5.16 the maximum angle $\theta_{max}(r)$, where the electrons are not reflected by the pinch magnet, is calculated. Considering every tenth initial radial position, a second order polynomial fit has been applied to obtain a cut function for the radial dependence for the simulated electrons.

(Bottom) In order to account for the uncertainties associated with the fit parameters, a correction factor is introduced. This correction factor equals the minimum value of the residuals obtained by taking the ratio between the true and fitted value for $\theta_{max}(r)$. By further multiplying the cut function by this correction factor the cut on the simulated electrons is further improved.

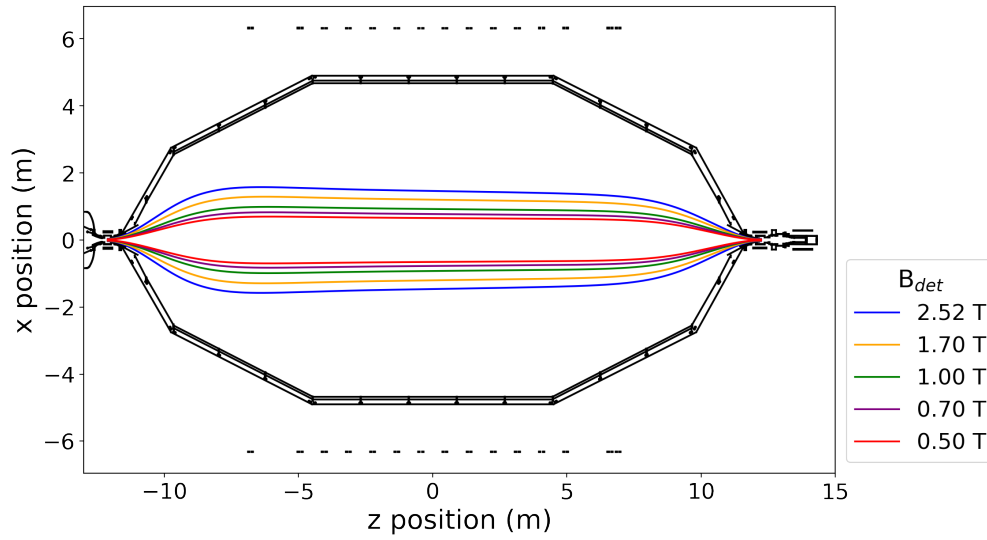


Figure 5.17: Illustration of the visible fluxtube inside the MS for different magnetic field settings at the detector. The lower the detector magnetic field, the smaller the visible fluxtube inside the MS. Thereby, the distance of the signal electrons to the symmetry axis is reduced, and the possibility of non-adiabatic motion decreased.

Limitations of Reducing B_{det}

A reduced detector magnetic field causes a larger cyclotron radius within the detector section, see Eq. 5.5. Therefore, this relation limits the minimal setting of the magnetic field strength at the detector. If the cyclotron radius get too large, the magnetic field gradient within one cyclotron length increases, which in turn violates the adiabatic transmission condition and further enhances the possibility of electrons being backreflected.

5.2.5. Increased Main Spectrometer Magnetic Field

Another approach to improve the electron transmission is to increase the magnetic field inside the MS. This not only results in a smaller field gradient inside the MS, but also in a smaller distance between the electron trajectories and the MS symmetry axis. As explained in Ch. 2, the MS is surrounded by 20 aircoils from the LFCS. These aircoils induce a axially symmetric magnetic field inside the MS. For the sake of simplicity, consider the LFCS aircoils as a number of loops N with radius R , each carrying an equal current I . The magnetic field strength, produced by a current flowing through these loops, can be expressed by the Biot-Savart law. In the center of the loop system along the central axis the magnetic field strength can be written as

$$B = \frac{\mu_0 N I}{2R} \quad (5.18)$$

with μ_0 the permeability of air. Consequently, the magnetic field strength inside the coils can be increased by a higher number of loops, smaller radius or a stronger current. To achieve a higher magnetic field strength inside the MS a scale factor was implemented in the simulations for this study. This scale factor (turnfactor) increases the coil current of the current maximal setting of the LFCS, i.e. 20 G at the center of the MS. A turnfactor of $TF = 1, 1.5, 2$ was chosen. Eq. 5.18 shows that this scaling factor is the same for either increasing the coil current or increasing the number of turns.

In Fig 5.18, the magnetic field strength along the z -axis inside and close to the MS is shown. One can see a steep increase for the operated magnets; the PS2 magnet in front of the MS and at the detector section, the pinch and detector magnet. In the zoom window the magnetic field strength inside the MS is shown. For higher scale factors a small increase of the magnetic field inside the MS is observed.

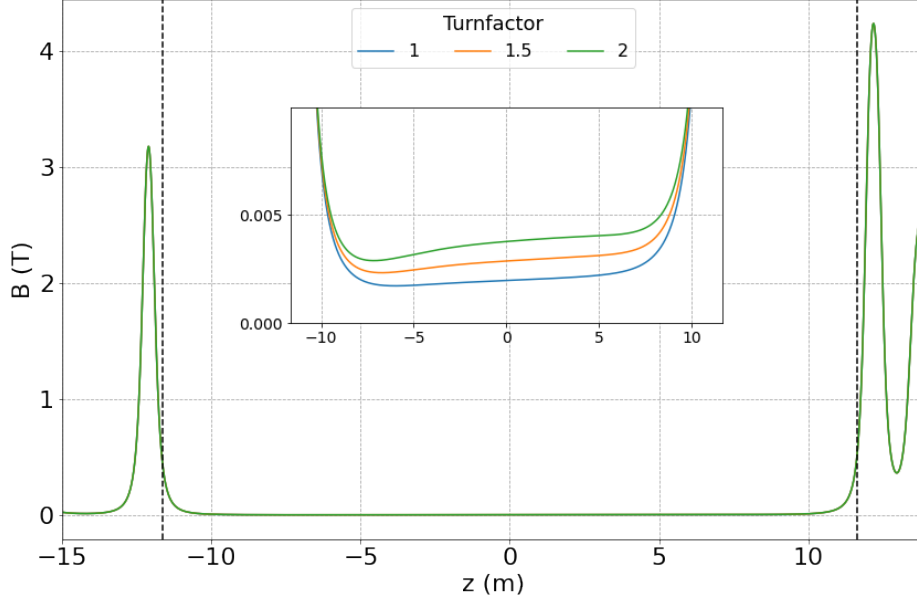


Figure 5.18: KASSIOPEIA simulation showing the magnetic field strength along the z -axis inside and close to the MS for different turnfactors of the LFCS coil current. The vertical dashed lines indicate the boundaries of the MS. Further one can see a steep increase of the magnetic field strength for the operated magnets; PS2 in front of the MS and at the detector section, the pinch and detector magnet. In the zoom window the much weaker magnetic field strength inside the MS is shown for different turnfactors. For a higher turnfactor a small increase of the magnetic field is observed.

For electron trajectories along the symmetry axis the magnetic field in the MS can be considered to be uniform. However, for off-axis electrons, following e.g. an outer magnetic field line, the cyclotron motion results in an asymmetric field. Which in turn has an impact on the curvature of the electrons trajectory. The asymmetry leads to an azimuthal drift [63]

$$\vec{v}_{\perp} = \frac{1}{qB} (E_{\perp} + 2 \cdot E_{\parallel}) \cdot \frac{\vec{B} \times \vec{\nabla}_{\perp} B}{B^2} \quad (5.19)$$

which depends on the electrons energy, the polar angle, and the radial distance to the MS symmetry axis. In order to avoid a large azimuthal drift depending on the gradient of the non-uniform magnetic field, the entrance radius of electrons r_i can be reduced, e.g. by decreasing the detector magnetic field strength besides increasing the magnetic field strength inside the MS.

5. Transmission Study

Limitations of Increasing B_{MS}

1. When increasing the coils current, more energy is emitted due to coil resistance in the form of heat. Expressed by Joule's first law the produced heat scales with the squared coil current.

$$P = I^2 R \quad (5.20)$$

Besides, technical limitations by the coils, an additional cooling system in the MS hall is needed. Which effects other component of the experiment and raises the operation costs.

2. The number of coils is limited by the static weight of the MS hull. For the same reason, additional coils at the entrance and exit would increase the weight and would require a new MS hull. Both approaches have an impact on the existing components. Further, the magnetic field strength has to be calculated and measured anew.
3. For a new coil system with smaller radii a new LFCS geometry would be needed. This not only rises the costs but also has an impact on other components of the experimental setup.

5.3. Results

The transmission study was performed for a total of 15 settings where the magnetic field strength in the MS and at the detector were varied. An increased magnetic field inside the MS is achieved by increasing the electric current of the large KATRIN LFCS air-coil system by implementing a scale factor. For each setting 10 million electrons were simulated. The dependence of the initial parameters of the signal electrons on the transmission is studied in the following analysis. The results for all studied settings can be found in Tab. A.1.

5.3.1. Reference KATRIN Setting

As a reference setting the current 70% beamline setting together with the max LFCS setting (20 G at the center of the MS) was chosen. The transmission probability for the reference setting is shown separately for the three initial parameters; kinetic energy, entrance radius and polar angle towards the guiding magnetic field line, in Fig. 5.19. The transmission probability for each of the three parameters shows clearly, the higher the respective value, the more electrons are not transmitted through the MS. Here should be emphasized, that the other two parameters are integrated over their full range. However, one can see a clear onset of the transmission loss for electrons possessing a energy surplus of around 5.8 keV. For electrons with a larger initial distance to the symmetry axis r_i , the transmission loss manifests itself at around 5 mm. When focusing on electrons with a polar angle very close to the maximal acceptance angle $\theta \sim \theta_{\max}$, the transmission drops drastically.

For a given setting, electrons can only be filtered by their energy surplus with respect to the retarding voltage. To ensure a significant search for the sterile neutrino signal, the retarding voltage has to be set such that 100% of the electrons are transmitted to the detector. For the current setting, the voltage can be lowered up to 5.8 kV below the β -electrons kinetic energy endpoint E_0 , ensuring a full electron transmission.

5. Transmission Study

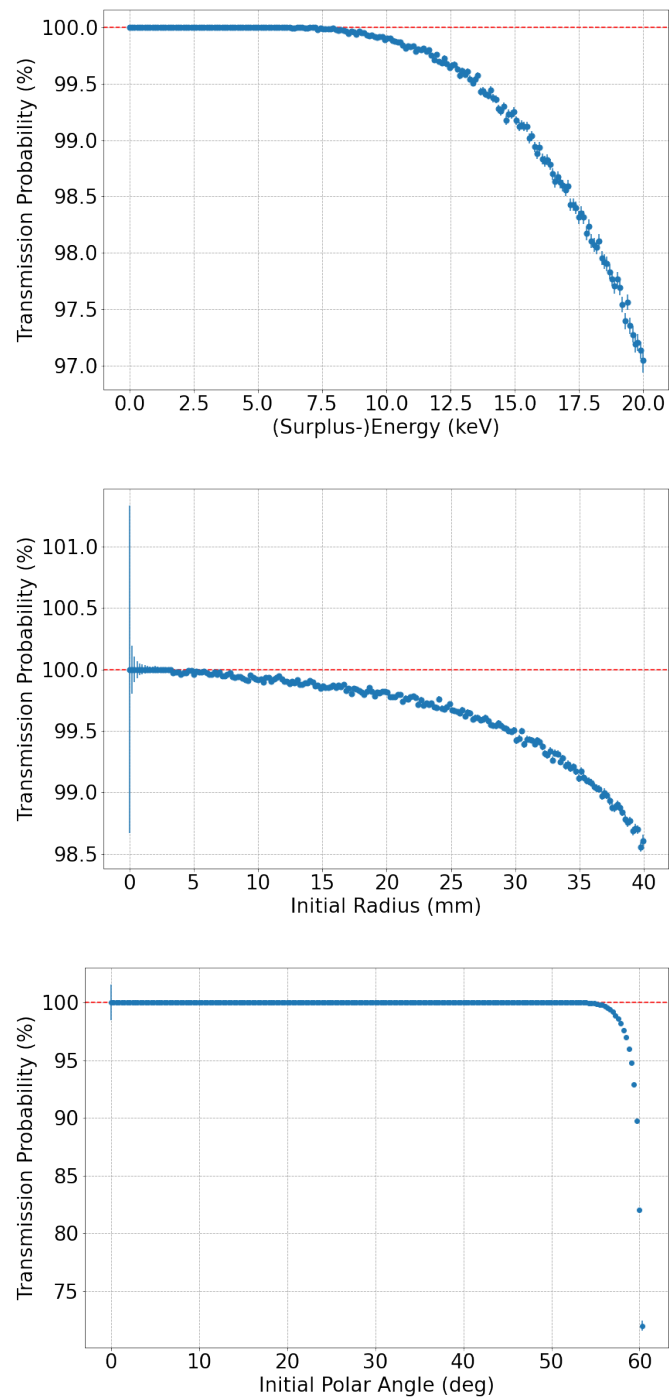


Figure 5.19: Transmission probability as a function of the three initial parameters; kinetic energy, entrance radius and polar angle, for the reference setting. While the considered parameter is varied, the other two initial parameters are integrated over their full range. Nevertheless, one can see a clear onset of the transmission loss for each of the initial parameters.

However, the initial parameters cannot be regarded independently. In Fig. 5.20, the combined effect of two initial parameters is shown. High energy electrons are much more sensitive to a high initial radius and/or large polar angle. Further, electrons that possess a large distance to the symmetry axis require a smaller polar angle, in order to be transmitted. The polar angle appears to be the most impactful parameter. A reduction from $\theta = 0^\circ$ to 53° would be sufficient to fully transmit electrons of all the energy considered in this study. Besides decreasing the energy surplus of the electrons, both the entrance radius and polar angle can be reduced by adjusting the magnetic field setting.

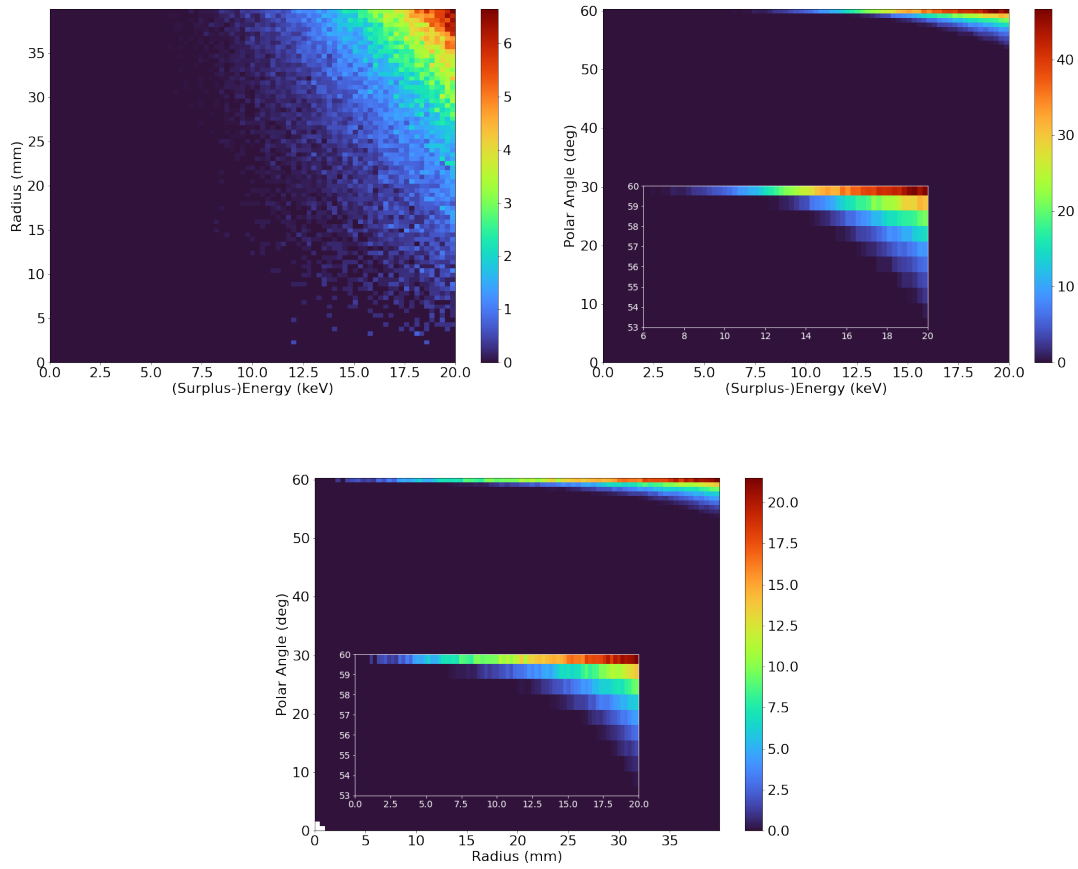


Figure 5.20: Transmission loss in percent depending on two of the three initial parameters: kinetic energy, entrance radius and polar angle. It shows clearly that the parameters are strongly interdependent. The higher one initial parameter, the more sensitive the electron transmission is on the other two parameters. The polar angle appears to be the most impactful parameter. A reduction from $\theta = 0^\circ$ to 53° would be sufficient to fully transmit electrons of all the energy considered in this study.

5.3.2. Decreased Detector Magnetic Field

When the detector magnetic field is decreased, the more inner part of the fluxtube is projected onto the detector wafer, expressed by Eq. 5.15 (Fig. 5.15). As the visible fluxtube is minimized, the radial distance of the signal electrons to the symmetry axis is effectively reduced. In Fig. 5.21, the transmission probability for the varied detector magnet setting is shown as a function of the initial kinetic energy. The visible area of the source is divided into radial sections. As expected, the transmission loss strongly depends on the initial kinetic energy and the initial radial position. Further, the plots show; the larger the initial distance to the symmetry axis, the more sensitive is the electron transmission to the initial kinetic energy. Whereas the transmission probability is just slightly increased for each respective radial range, the transmission is improved up to a few percent by decreasing the magnetic field strength at the detector. For a weaker magnetic field strength at the detector the size of the visible fluxtube is decreased. Hence, only electrons propagating close to the symmetry axis are projected onto the detector, for which the non-adiabatic impact on the transmission is subdominant.

The transmission probability as a function of the initial kinetic energy for different detector magnetic field settings is shown on the upper plot in Fig. 5.22. The transmission is integrated over the full respective initial radius and polar angle regions. By lowering the detector magnetic field strength the transmission for electrons, possessing a high kinetic energy with respect to the retarding potential E_{surplus} , can be improved significantly. At $E_{\text{surplus}} = 18.6 \text{ keV}$, the electron transmission can be increased approximately by 2% by lowering the detector magnetic field strength from $B_{\text{det}} = 2.5 \text{ T}$ to 0.5 T . More importantly, the onset of transmission loss gets shifted towards higher energies. Consequently, the retarding potential can be lowered when decreasing B_{det} for a full transmission. Therefore, electrons with a higher surplus energy can enter the MS. This in turn increases the accessible mass range m_s for the search of the sterile neutrino. The lower plot in Fig. 5.22 shows the impact of B_{det} on the maximum energy surplus of the electrons for a full transmission. As the maximum surplus energy equals the accessible mass range for the search of the sterile neutrino, reducing B_{det} from the nominal value of 2.52 T to 0.7 T enlarges the analyzable mass range m_s about 2.1 keV to 7.9 keV .

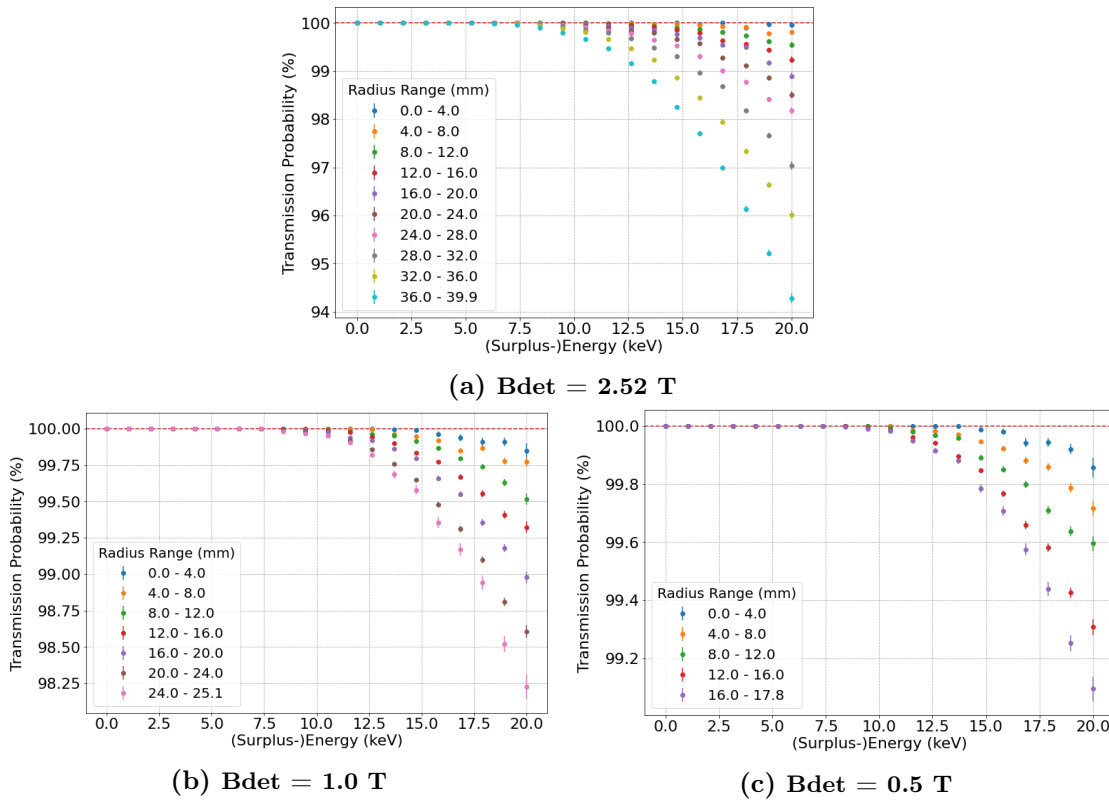


Figure 5.21: Transmission probability as a function of the initial kinetic energy for different magnetic field settings at the detector for the maximum LFCS setting ($TF=1$). The generated electrons are sorted into radial ranges. Whereas the transmission probability is just slightly increased for each respective radial range, the transmission can be improved up to a few percent by decreasing the detector magnetic field strength. A weaker detector magnetic field strength results in a smaller size of the visible fluxtube. Therefore, only electrons propagating close to the symmetry axis are projected onto the detector.

5. Transmission Study

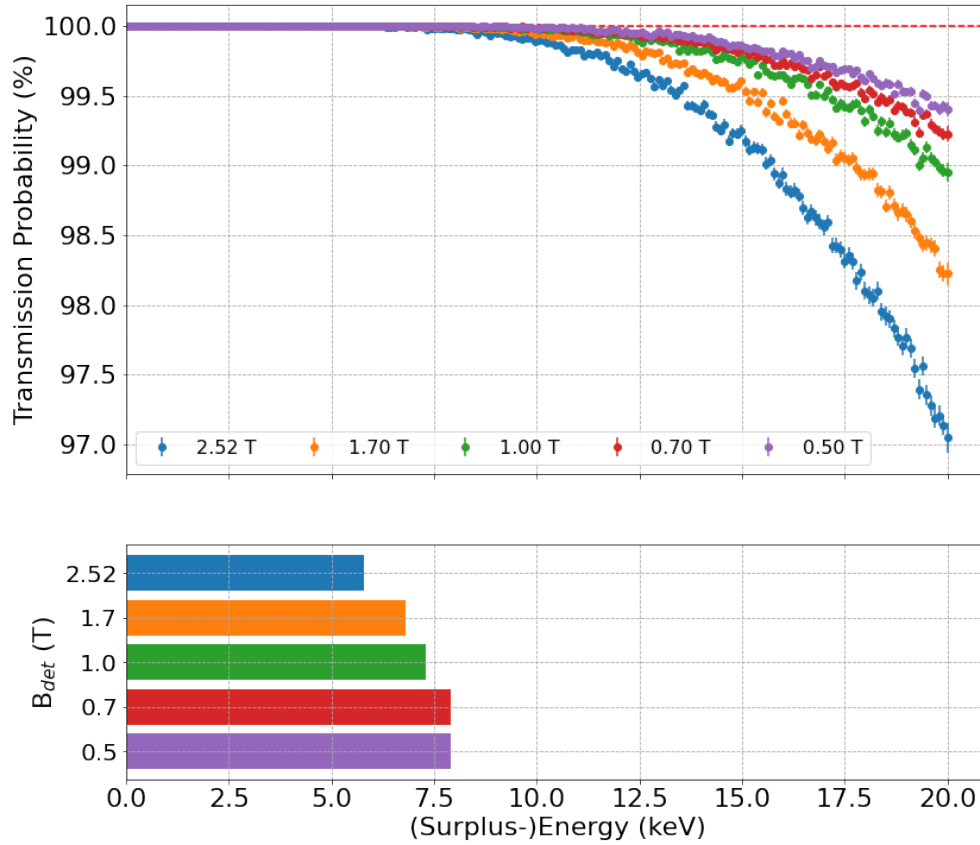


Figure 5.22: (Top) Transmission probability as a function of the initial kinetic energy for different detector magnetic field settings and constant maximum LFCS setting ($\mathbf{TF} = \mathbf{1}$). One can see a clear increase of the transmission probability for high surplus energy electrons when lowering the detector magnetic field strength. This allows to lower the retarding potential in the MS. Consequentially, the accessible mass range for the sterile neutrino search is increased. (Bottom) Allowed maximum surplus energy with respect to the retarding potential of electrons inside the MS for a full transmission. As the maximum allowed surplus energy equals the accessible mass range for the search of a sterile neutrino, a weaker detector magnetic field strength increases the range for the search of the sterile neutrino mass.

5.3.3. Increased Main Spectrometer Magnetic Field

As previously explained, a larger magnetic field strength in the MS results in a smaller magnetic field gradient and a smaller distance of the electron's trajectory to the symmetry axis in the MS. Hence, the on-set of the non-adiabatic motion is assumed to start for greater values of the initial parameters and the electron transmission is increased. In Fig. 5.23, the transmission probability as a function of the initial kinetic energy of the electrons is shown for the reference and the two enhanced settings, where the current of the LFCS aircoils was scaled by a factor of $TF = 1.5$ and 2. Here, the detector magnetic field strength, $B_{\text{det}} = 2.52 \text{ T}$, is constant. One can see a significant improvement of the electron transmission for high energies, when increasing the MS magnetic field strength. At $E_{\text{surplus}} = 18.6 \text{ keV}$, the transmission can be increased approximately by 2% (2.2%) for a scaling factor of $TF = 1.5$ ($TF = 2$). The onset of the transmission loss is again shifted towards higher energies, which is crucial for the keV sterile neutrino search.

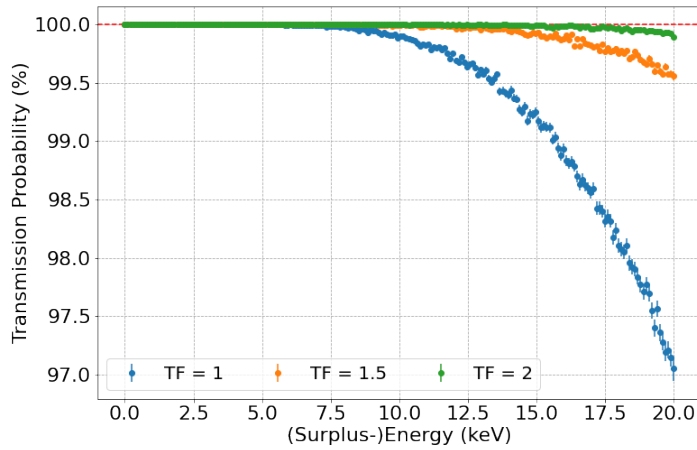


Figure 5.23: Transmission probability as a function of the initial kinetic energy of the electrons for different magnetic field strength inside the MS for the nominal detector magnetic field strength $B_{\text{det}} = 2.52 \text{ T}$. The transmission loss manifests itself at much weaker strength and at greater initial kinetic energies for an increased MS magnetic field strength.

In Fig. 5.24, the transmission probability as a function of the initial kinetic energy of the electrons and for different radial positions is shown. The upper plot shows the distribution for the reference setting. The enhanced settings, are shown in the two bottom plots. For a stronger MS magnetic field strength, B_{MS} , the transmission per radial section can be significantly enhanced. Further, a full electron transmission to the detector is achieved for a wider radial range around the symmetry axis at the source by increasing B_{MS} .

5. Transmission Study

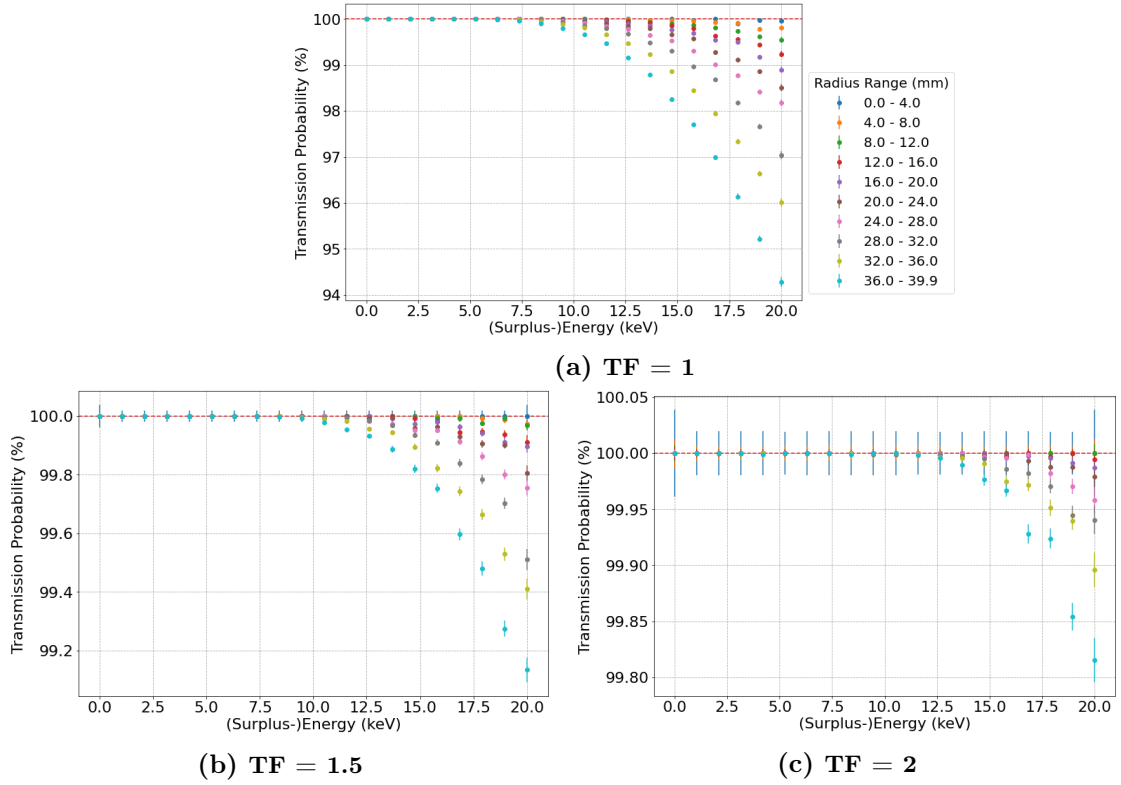


Figure 5.24: Transmission probability as a function of the initial kinetic energy for different magnetic field settings inside the MS and for the nominal detector magnetic field strength. The generated electrons are sorted into radial rings at the source. One can see a significant enhancement of the transmission per radial range for an increased B_{MS} . More importantly, a full electron transmission to the detector is achieved for a wider radial range around the symmetry axis at the source for a stronger B_{MS} .

The maximally allowed energy surplus per radial region is shown for each considered case of Fig. 5.24. The circles represent the fluxtube area at the source. Increasing the magnetic field strength inside the MS, clearly enlarges the initial radial area for which 100% of the generated electrons are transmitted to the detector. As a result, the retarding potential can be lowered to much smaller voltages, while still all electrons are transmitted from the source to the detector.

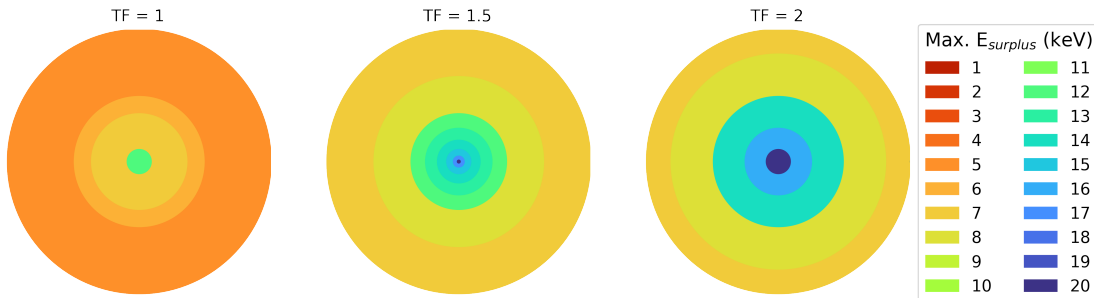


Figure 5.25: Depiction of the fluxtube area at the source for constant $B_{\text{det}} = 2.52$ T and different scaling factors of the magnetic field strength inside the MS. For an increased magnetic field inside the MS the transmission is improved for larger initial radial positions. The figure shows that for an increased magnetic field inside the MS, the retarding potential can be lowered to smaller voltages while all electrons are transmitted from the source to the detector.

In Fig. 5.26, 5.27 the transmission probability as a function of the initial kinetic energy for the studied values of B_{det} is shown for $\text{TF} = 1.5$ and 2. One can see a steady increase of the electron transmission for a weaker B_{det} , where the effect is magnified when B_{MS} is additionally increased. Considering the currently favored setting for the detector magnet for the future TRISTAN experiment of $B_{\text{det}} = 1.0$ T, the maximum allowed energy surplus of electrons inside the MS with full transmission can be increased from $E_{\text{surplus}} = 7.3$ keV for the current max. LFCS setting, to $E_{\text{surplus}} = 11.4$ keV for increasing B_{MS} by a scaling factor of $\text{TF} = 1.5$ and $E_{\text{surplus}} = 14.9$ keV by a scaling factor of $\text{TF} = 2$. The best transmission is achieved for $B_{\text{det}} = 0.5$ T and $\text{TF} = 2$, where the retarding potential can be lowered to $qU = 1.2$ kV. For this setting one is able to look 17.4 keV into the energy spectrum of the tritium β -electrons, such that for the keV-scale sterile neutrino search the mass range of $m_s \in [0, 17.4]$ keV can be covered.

5. Transmission Study

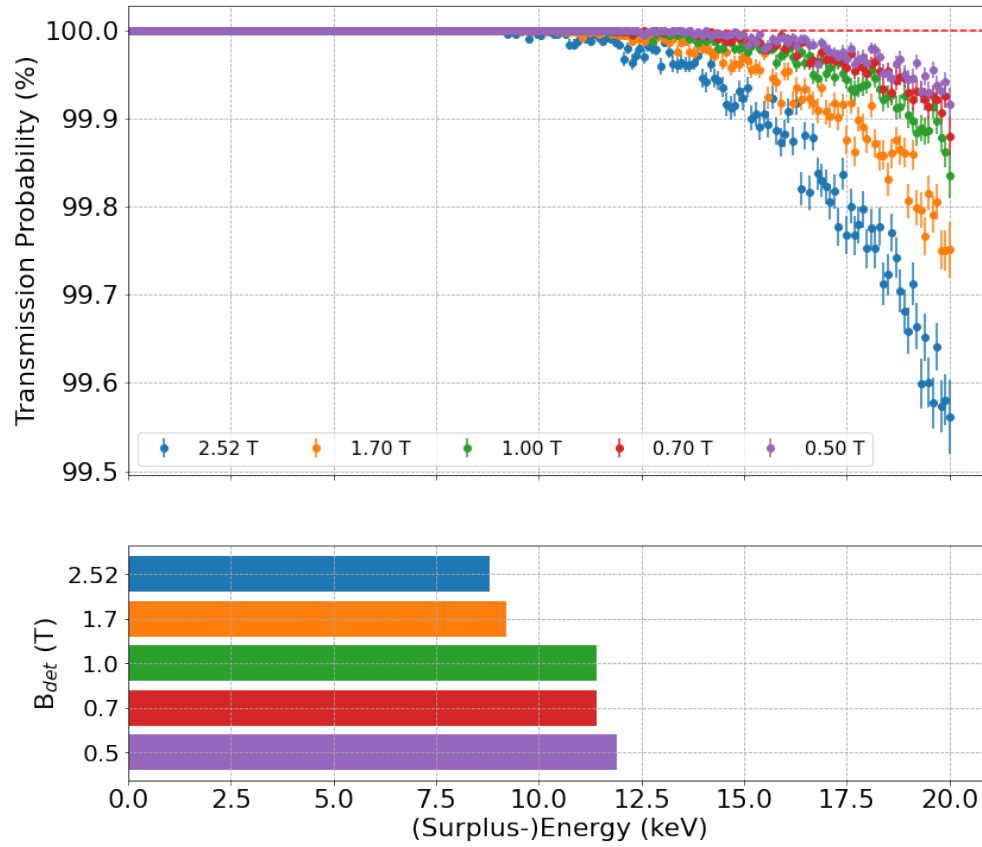


Figure 5.26: (Top) Transmission probability as a function of the initial kinetic energy for the studied values of B_{det} for $TF = 1.5$. (Bottom) Corresponding maximum energy surplus of the electrons inside the MS for a full transmission.

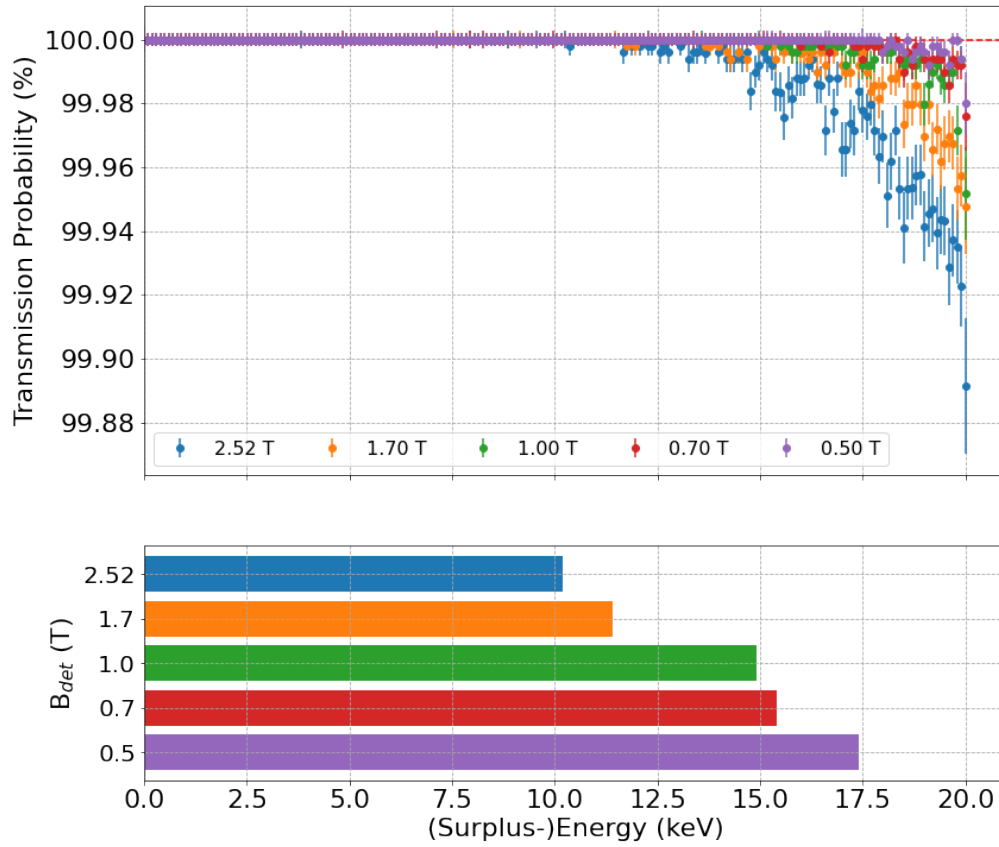


Figure 5.27: (Top) Transmission probability as a function of the initial kinetic energy for the studied values of B_{det} for $\mathbf{TF} = 2$. (Bottom) Corresponding maximum energy surplus of the electrons inside the MS for a full transmission.

5.4. Conclusion

The simulations have shown that electrons with a high initial kinetic energy, large initial radial position and/or initial polar angle are more prone to undergo a non-adiabatic change of their polar angle such that they are reflected back to the point of origin. It can be concluded, that a higher magnetic field inside the MS, decreases the field gradient along the electron's trajectories, while also the distance of the signal electrons to the symmetry axis inside the MS is reduced. The entrance radius of the signal electrons can be lessened by a lower detector magnetic field strength. Therefore, the more inner part of the fluxtube is projected onto the detector. The highest electron transmission is achieved by combining an increased magnetic field inside the MS with a reduced detector magnetic field. In Fig. 5.28, the total transmission, integrated over the full initial energy, radial position and polar angle ranges, is shown as a function of B_{det} on the left and the scaling factor TF on the right. Although, a weaker B_{det} or an increased B_{MS} significantly improve the transmission independently, a combination of both approaches seems to be more effective.

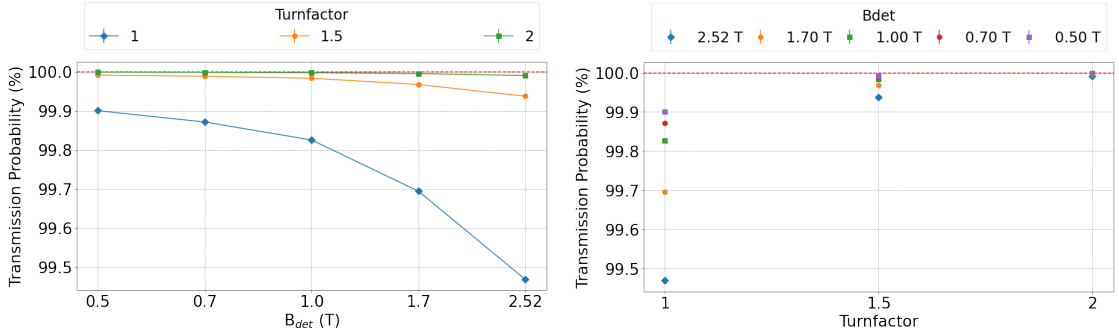


Figure 5.28: (Left) Total transmission probability as a function of B_{det} for different magnetic field settings inside the MS. By only decreasing B_{det} , the total transmission can be improved by approximately 0.5%. This effect becomes less eminent for a stronger B_{MS} . (Right) Total transmission probability as a function of the scaling factor TF, that increases the magnetic field strength inside the MS, for different settings of B_{det} . A stronger B_{MS} improved the total transmission drastically.

Of greater importance than the total transmission is the allowed energy surplus of the electrons inside the MS for a full transmission. The limit on the energy surplus for each setting is shown in Fig. 5.29. When only decreasing B_{det} the limit can be extended from 5.8 keV for the reference setting to 7.9 keV for $B_{\text{det}} = 0.5$ T. Focusing on the currently planned value for $B_{\text{det}} = 1.0$ T for the TRISTAN project, the retarding potential inside the MS can be lowered such that an energy surplus of 11.4 keV for TF = 1.5 and 14.9 keV for TF = 2 can be achieved. Almost the full β -electron energy spectrum can be investigated for $B_{\text{det}} = 0.5$ T and TF = 2, where the maximum $E_{\text{surplus}} = 17.4$ keV. However, increasing the current of the LFCS aircoils or the number of coils by such a high factor as TF = 1.5 or 2 comes with technical challenges and

limitations. Therefore, a possible solution would be to consider only inner pixels in the analysis, where only electrons close to the symmetry axis are mapped onto the detector. In Fig. 5.25 it was shown, that for inner radial ranges a full transmission can be achieved. Hence, when considering the central pixels, only the inner radial ranges are considered for the analysis. This allows to further decrease the retarding potential inside the MS, by still obtaining a full transmission of electrons up to a certain radial threshold, which can be determined for the pixel selection.

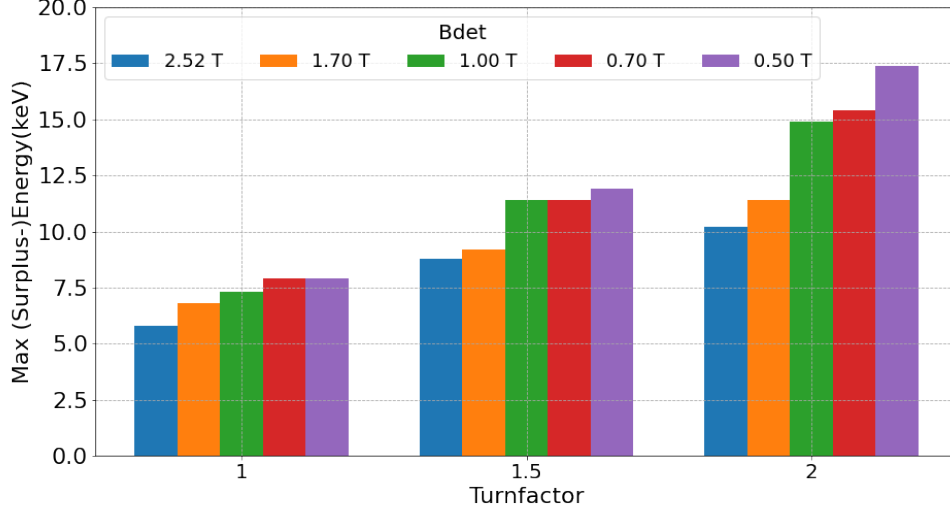


Figure 5.29: Maximum surplus energy of electrons inside the MS for a full transmission for all studied settings. By only decreasing B_{det} the retarding potential can be lowered such that the allowed energy surplus from 5.8 keV for the reference setting can be improved to 7.9 keV for $B_{\text{det}} = 0.5$ T. For $B_{\text{det}} = 0.5$ T and an increased B_{MS} by the scaling factor of $\text{TF} = 2$, the retarding potential can be lowered in order that the accessible mass range for the search of the keV-scale sterile neutrino can be extended to 17.4 keV.

6. Condensed $^{83\text{m}}\text{Kr}$ Measurement & Simulation

The simulation results, presented in Chapter 5, have shown that the initial energy surplus, the radial distance to the symmetry axis and the polar angle to the guiding magnetic field line of the electrons have a significant impact on the transmission. Moreover, a key aspect is the magnetic field strength inside the volume, which the electron transverses. Exploiting the unique decay properties of the meta-stable $^{83\text{m}}\text{Kr}$, by using it as source, placed inside the CPS, one is able to measure the transmission properties and probability as a function of electron's energy surplus by changing the applied retarding potential inside the MS. By further moving the source in the y -direction, the radial dependence of the electron transmission can be estimated. Additionally, for each radial position, measurements at different magnetic field setting inside the MS have been performed.

First, this chapter introduces the $^{83\text{m}}\text{Kr}$ source and then shows the result of the krypton measurements from October 2022. A first approximation of the pile up rates expected during the measurement has been made with a Monte Carlo simulation. Furthermore, the measurement has been simulated with KASSIOPEIA and the results are compared to the measured data.

6.1. Condensed $^{83\text{m}}\text{Kr}$ Source

$^{83\text{m}}\text{Kr}$ is produced by the electron capture decay of ^{83}Rb with a half-life of 86.2 d. The decay scheme of ^{83}Rb into the stable isotope ^{83}Kr is shown in Fig. 6.1. With a branching ratio of 75 %, ^{83}Rb decays into the meta-stable isomeric state $^{83\text{m}}\text{Kr}$, the second excited state of ^{83}Kr with spin-parity $\frac{1}{2}^-$ and excitation energy of 41.56 keV [64]. The metastable isotope $^{83\text{m}}\text{Kr}$, with the half-life of $\tau = 1.83$ h, provides a suitable source for the energy calibration and systematic studies of the KATRIN experiment due to its unique decay properties. Via a cascade of two electromagnetic transitions with the energies of 32.15 keV and 9.41 keV, it decays into the ground state, releasing many mono-energetic conversion electrons with suitable energies. For the KATRIN energy calibration the γ -32 keV K-line yields a good reference as the conversion electrons possess energies 760 eV less than the tritium endpoint. In order to measure the impact of non-adiabaticity on electrons with high energy surplus, the focus here lies on the L-lines, as these provide a sufficient number of electrons with a high kinetic energy.

6. Condensed $83m\text{-Kr}$ Measurement & Simulation

The exact values for the released energy and intensity of the decays are listed in Tab.6.1. A great advantage of the short life-time is the exclusion of long term contamination of the KATRIN components.

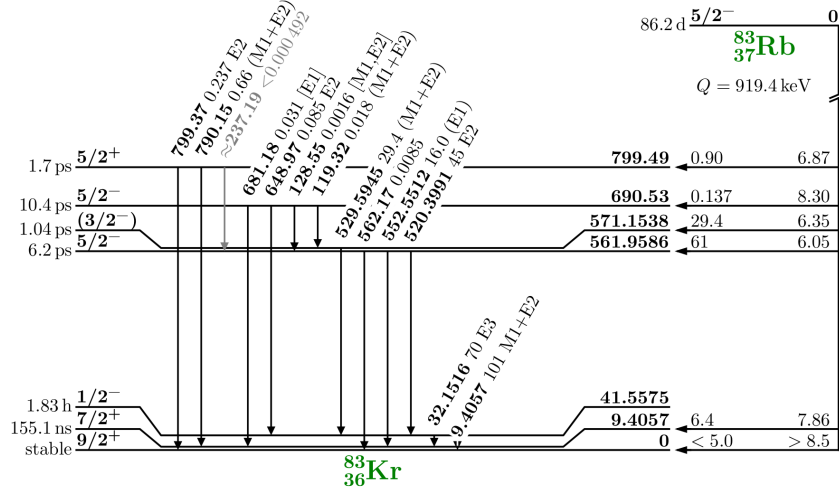


Figure 6.1: Decay scheme of ^{83}Rb into stable ^{83}Kr . With a branching ratio of 75 % ^{83}Rb decays into the meta-stable isomeric state ^{83m}Kr . Via a cascade of two electromagnetic transitions the meta-stable state decays into the ground state. The mono-energetic conversion electrons released by this de-excitation are a useful source for calibrations or the study of the non-adiabatic impact on the electron transmission. This figure is taken from [65].

The theoretical differential and integral energy spectra for these mono-energetic conversion electrons is shown in Fig. 6.2. No systematic effects are considered on these plots. In the experiment electrons lose energy in the source due to scattering processes, which results in broadened energy peaks. Further, detector systematics such as pile-up, backscattering and charge sharing have to be included. In the differential spectrum one can see the mono-energetic lines of the conversion electrons. KATRIN measures in the integral mode, i.e. the detector counts the impinging electrons and the energy resolution is performed with the help of the retarding potential inside the MS. However, the KATRIN FPD is able to resolve the energy of the electrons to some extent. Generally, the differential is translated into the integral spectrum as follows: for lower retarding voltages (qU) than the first energy line (K-32 line), all electrons are transmitted to the detector. This is visible in the first plateau. When the qU value exceeds the energy of the K-line, all K-32 electrons are stopped. Consequently, the plateau falls about the amount of the K-32 intensity. The second plateau stays constant until the next energy line is passed, and so forth.

Line	Energy E_{ce} (eV)	Intensity I_{ce} per decay (%)
K	17824.2(5)	24.8(5)
L ₁	30226.8(9)	1.56(2)
L ₂	30419.5(5)	24.3(3)
L ₃	30472.2(5)	37.8(5)
M ₁	31858.7(6)	0.249(4)
M ₂	31929.3(5)	4.02(6)
M ₃	31936.9(5)	6.24(9)
M ₄	32056.4(5)	0.0628(9)
M ₅	32057.6(5)	0.0884(12)
N ₁	32123.9(5)	0.0255(4)
N ₂	32136.7(5)	0.300(4)
N ₃	32137.4(5)	0.457(6)

Table 6.1: Properties for the γ -32 keV conversion lines [65]. Listed are the conversion lines with their energy and intensity.

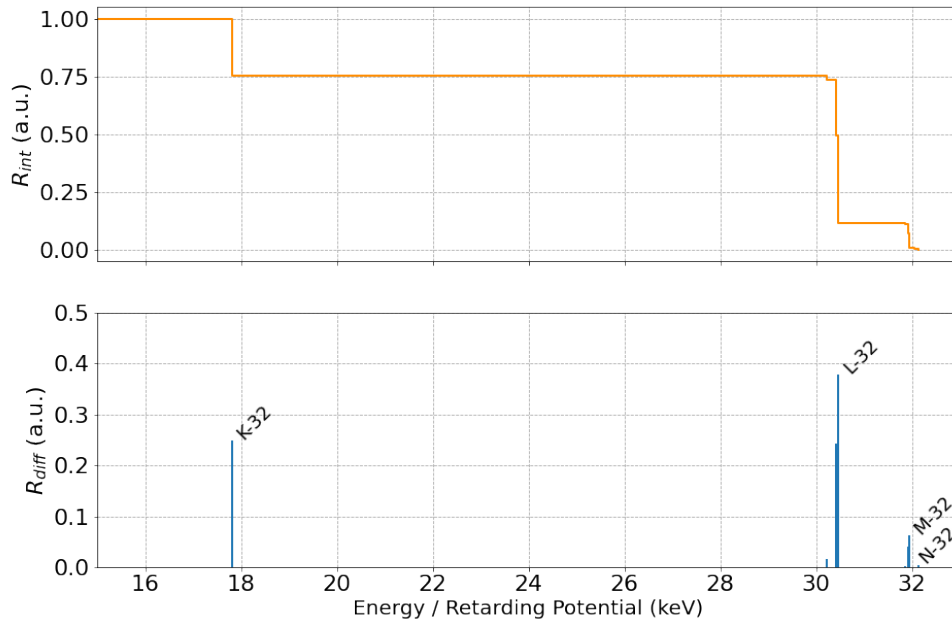


Figure 6.2: The differential (bottom) and integral (top) energy spectra for the ^{83m}Kr γ -32 keV electron conversion lines, assuming no systematic effects.

6.2. Measurement

The *Kr* substrate is an highly oriented pyrolytic graphite (HOPG) square of the size 2×2 cm. First, a thin film of a few 10 nm of stable krypton is frozen on top of the HOPG substrate. Then the meta-stable krypton is condensed on top. The source is placed between the CPS coils, where the initial magnetic field strength is approximately $B_i = 0.9$ T.

For the measurement of the transmission properties with the condensed krypton (CKr) source the following settings were considered:

- All beamline magnets are operated at their nominal field strength (70%), see Tab. A.2.
- The source was positioned at three radial positions: central, intermediate, outer position, respectively corresponding to a source position of $y_{\text{source}} = 4$ mm, 44 mm and 73 mm. Therefore, the electron beam was focused onto the pixels 2, 31 and 103, as shown in Fig. 6.3.
- The magnetic field inside the MS B_{MS} was set to a low, intermediate and high value, respectively corresponding to $B_{\text{MS}} = 6, 8$ and 20 G.
- Step size: the retarding voltage was varied between 10 – 30.0 kV in steps of 2 kV and two extra points were included close to the K-32 and L-32 line at 17.5 kV and 30.5 kV.
qU = 10, 12, 14, 16, 17.5, 18, 20, 22, 24, 26, 28, 30, 30.5 (kV)
- Measurement Time Distribution: each qU point was measured for 60 s.

In order to estimate the impact on the electron transmission due to non-adiabatic effects, the measured rate at the detector was compared for different radial positions of the source and different magnetic field configurations inside the MS. Thus, with the resulting 9 settings the dependence on the initial radial position of the electrons and on different magnetic field of the electron transmission can be determined. The transmission loss, $1 - T(qU)$, caused by non-adiabatic electron motion can be estimated by taking the relative difference $\Delta R(qU)$ between the rate R_{max} of the respective 'best' scenario, i.e. central position and highest magnetic field strength inside MS, and the rate R_i of the varied parameter i for each retarding voltage. Additionally, the systematic effects are assumed to cancel by first order approximation for the relative difference, when considering the same retarding voltage set point.

$$1 - T(qU) = 100 \cdot \Delta R(qU) \quad (6.1)$$

$$\Delta R(qU) = \frac{|R_i(qU) - R_{max}(qU)|}{R_{max}(qU)} \quad (6.2)$$

The statistical uncertainty for each voltage set point is determined by $\sigma_R = \sqrt{R(qU)}$. Therefore, the statistical uncertainty for the transmission loss for each point follows the formula for the error propagation for division

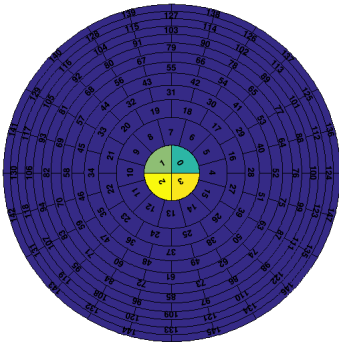
$$\sigma_{1-T}(qU) = (1 - T) \sqrt{\left(\frac{\sigma_i}{R_i}\right)^2 + \left(\frac{\sigma_{max}}{R_{max}}\right)^2}. \quad (6.3)$$

In Fig. 6.3, the FPD map and the total counts per pixel for all three source positions for $B_{MS} = 20$ G are shown. On the FPD map the pixels that have received the highest rates are highlighted in yellow. One can see that the adjacent pixels also detected a higher rate. This results mostly from the spacial expansion of the source.

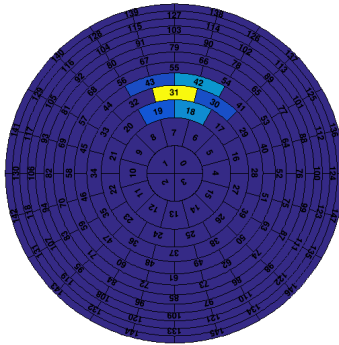
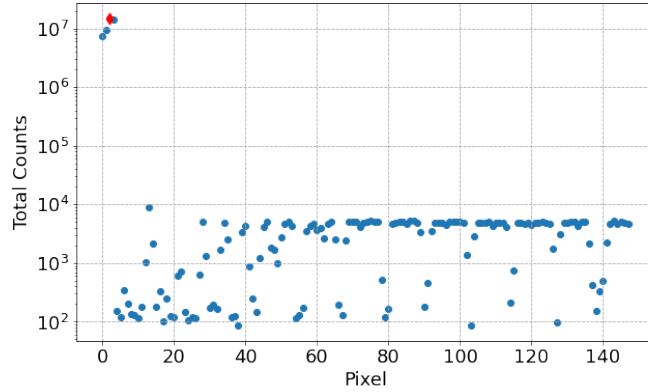
The integral spectra obtained for the three source positions and for the three magnetic field settings inside the MS are shown in Fig. 6.4 and Fig. 6.5. As expected, a greater transmission loss is observed for a larger initial distance to the symmetry axis of the electrons at the source and/or a weaker magnetic field strength inside the MS. Further, an increase of transmission loss towards low retarding voltages, i.e. high energy surplus of the electrons becomes apparent. When the source is located at the central position, no transmission loss was observed for $B_{MS} = 8$ G with respect to the max LFCS setting of $B_{MS} = 20$ G. For the weakest magnetic field setting $B_{MS} = 6$ G, a maximum transmission loss of 2.8% was measured. By further moving the source away from the symmetry axis to the intermediate position, up to 14.5% and 24.2% of the electrons were lost for $B_{MS} = 8$ G, or $B_{MS} = 6$ G respectively. The highest transmission loss is observed for the outer position, here up to 30.0% (44.1%) of the electrons are lost for the intermediate (weak) setting of B_{MS} . In order to estimate the transmission loss resulting from

6. Condensed 83m-Kr Measurement & Simulation

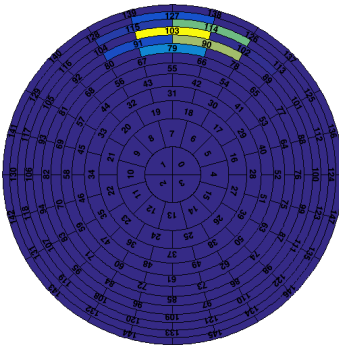
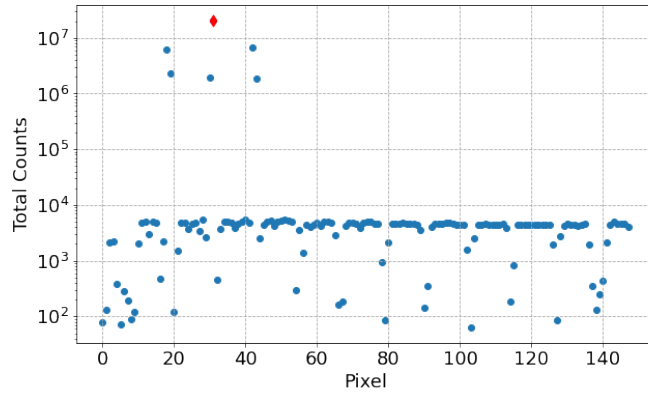
the radial position of the source, the relative ratio is taken between the central and the intermediate/outer position for a fixed magnetic field setting inside the MS. Therefor, a maximum transmission loss of 2.7% and 7.9% are observed at $B_{\text{MS}} = 20\text{ G}$ for the intermediate and outer position of the source. A higher transmission loss of maximum 15.9% or 35.1% was measured for the intermediate and outer radial initial position at the intermediate magnetic field setting. For the weakest B_{MS} up to 23.2% (47.2%) of the electrons are lost when the source was moved from the central to the intermediate (outer) position. One can conclude, that the measurement with CKr source has shown; the electron transmission is sensitive to both, the initial radial position and the magnetic field configuration inside the MS. Further, it was confirmed that the non-adiabatic impact on the electron transmission increases for a greater initial distance to the symmetry axis. A weaker MS magnetic field strength results in a high magnetic field gradient and larger distance of the signal electrons to the symmetry axis inside the MS, and hence leads to high loss of transmitted electrons. Therefore, the conducted experiment indicated that a high magnetic field configuration inside the MS together with an almost point-like source placed along the symmetry axis is mandatory for the keV-scale sterile neutrino search.



Central position



Intermediate position



Outer position

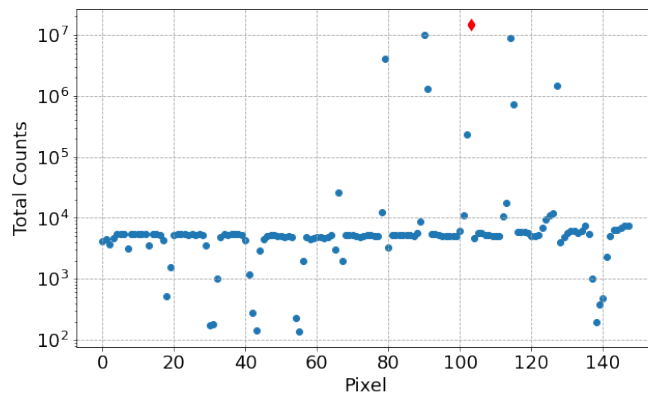


Figure 6.3: For each position of the source at $B_{MS} = 20\text{ G}$ the FPD map is shown on the left and the total counts per pixel integrated over all qU values on the right. The FPD map highlights the pixels with the maximum counts per second in yellow. The source was positioned such that, the signal electron beam is focused onto the respective pixel 2, 31 and 103. Due to spatial expansion of the source and transmission effects, the electrons are spread over all pixels with a maximum observed on the respective pixel. In the counts per pixel plots the red points indicate the pixel with the highest total rate.

6. Condensed 83m-Kr Measurement & Simulation

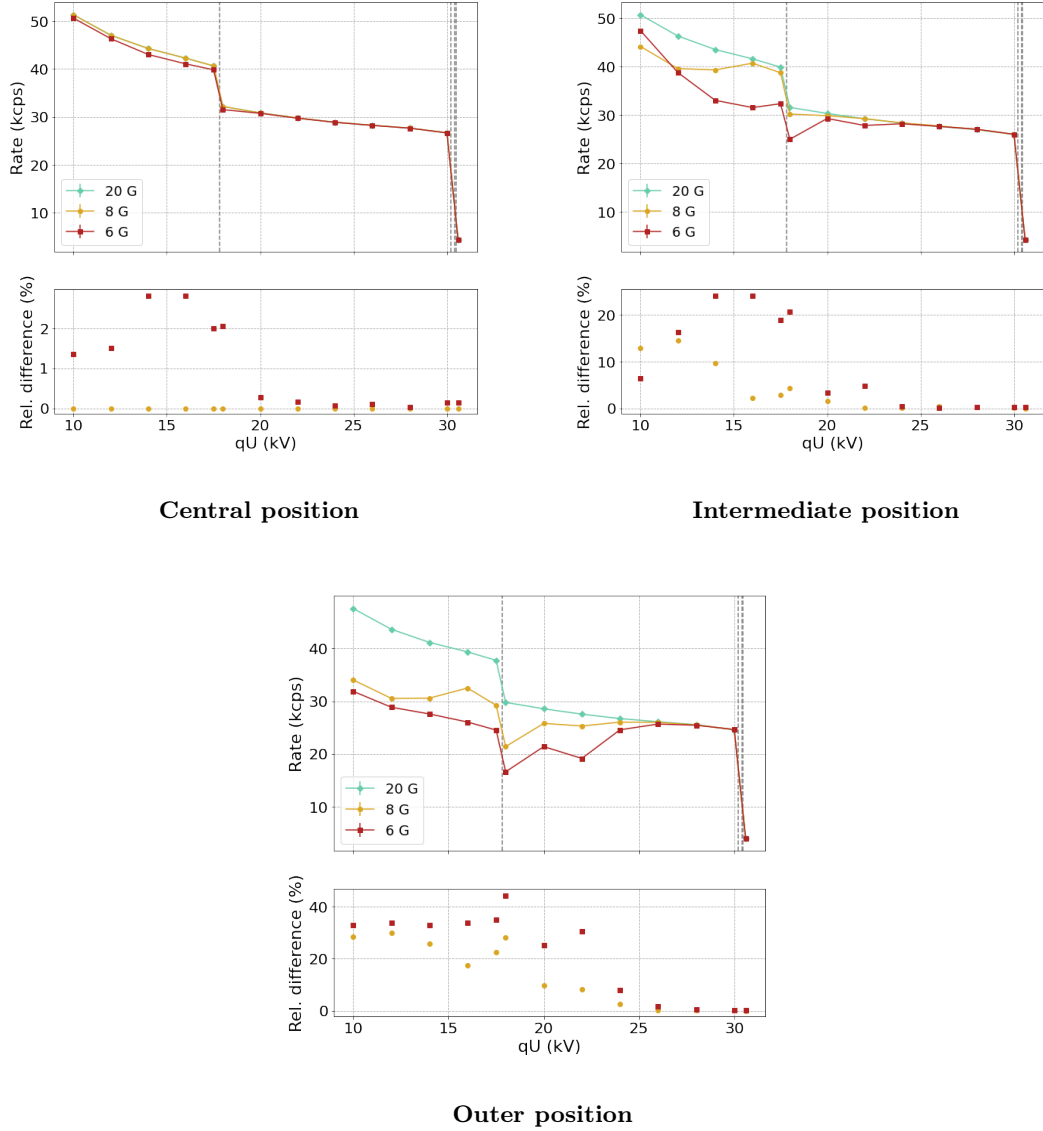


Figure 6.4: (Top) Integral spectra for the CKrS measurement for the three studied radial source positions; $y_{\text{source}} = 4, 44, 73$ mm. The transmission decreases significantly when the source is placed further away from the symmetry axis. The negative impact of a weaker MS magnetic field setting is intensified for a larger radial position of the source.

(Bottom) For the determination of the transmission loss the relative difference between the respective maximum with the intermediate/weak magnetic field setting is taken. It is assumed that systematic effects cancel by first order approximation. A clear decrease of the transmission can be seen for lower retarding voltages, i.e. higher energy surplus. For the central position a maximum transmission loss of 2.8% for $B_{\text{MS}} = 6$ G is observed. However, up to 44.1% of the electrons are not transmitted to the detector for the outer position and 6 G.

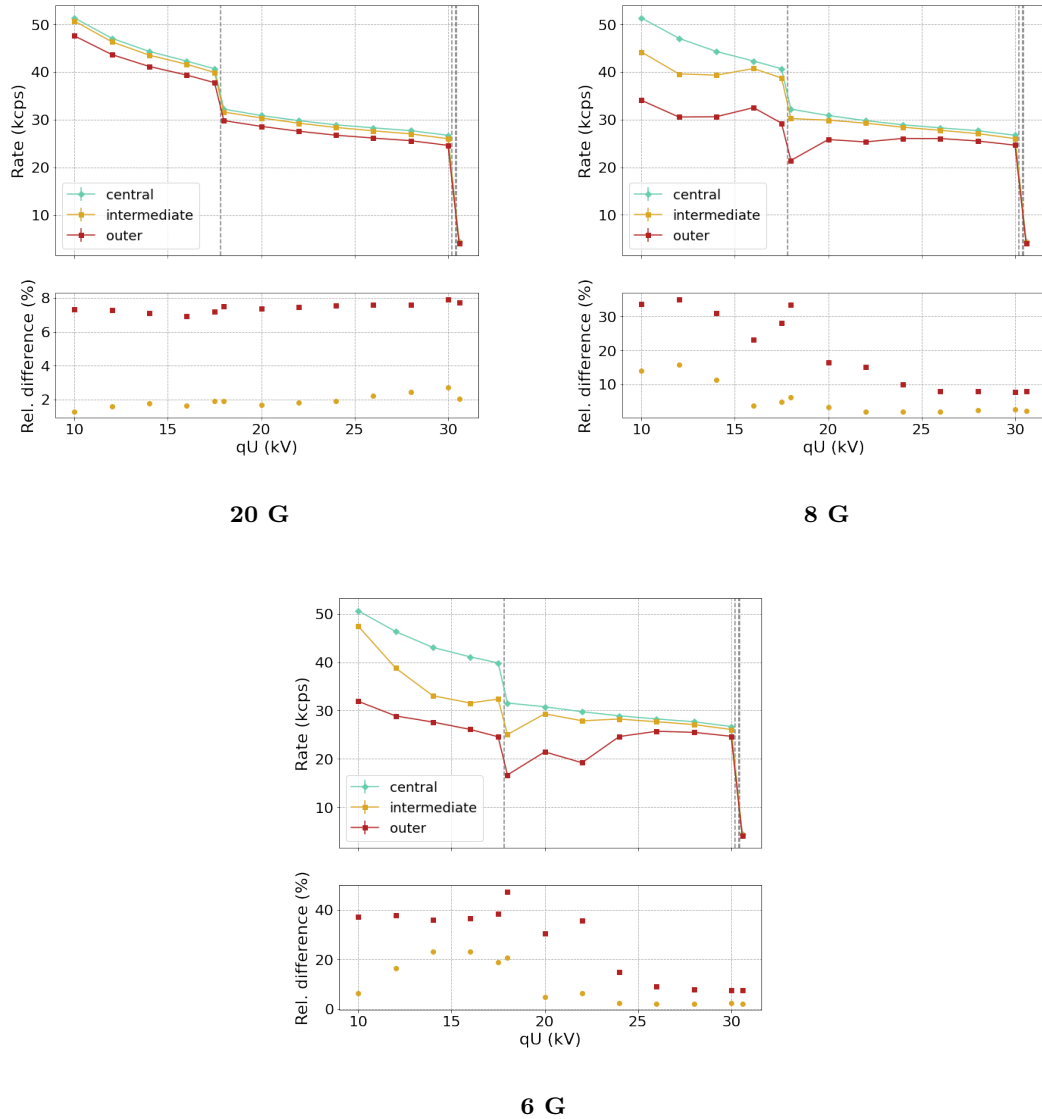


Figure 6.5: (Top) Integral spectra for the CKrS measurement for the three studied magnetic field settings inside the MS; $B_{MS} = 6, 8, 20$ G. A clear decrease of the transmission can be observed for a weaker magnetic field strength inside the MS. This effect is intensified for a greater radial position of the source.

(Bottom) The relative difference is calculated between the respective central and intermediate/outer source position in order to estimate the transmission loss. Systematic effects are assumed to cancel by first order approximation. A transmission loss of up to 7.9% is observed for $B_{MS} = 6$ G at the central position, whereas up to 47.2% of the electrons are lost for the same B_{MS} setting but the outer position.

6. Condensed 83m-Kr Measurement & Simulation

The differential spectra for the CKr measurement for different qU values at the central position and $B_{\text{MS}} = 20 \text{ G}$ are shown in Fig. 6.6. The systematic impact of electron backscattering at the detector is visible as a gradient tail towards lower energies, more prominent for lower values of qU. Electrons, which first deposit some of their energy at the detector and then are backscattered, can either be lost inside the MS when their energy is not sufficient anymore to overcome qU or can be backreflected to the detector and be detected with a smaller kinetic energy. The backreflected electrons can be double counted at lower energies, which results in the visible backscattering tail. Due to further scattering processes inside the source, electrons lose some of their kinetic energy. Therefore, not all electrons enter the MS with the fixed transition energy but with a smeared distribution with a maximum kinetic energy equal to the energy of the respective conversion line. This effect is also apparent in the integral spectra of Fig. 6.4 and 6.5, where the theoretical plateaus have a decreasing slope towards increasing qU values, i.e. decreasing energy surplus. Due to this energy distribution, some electrons are already stopped for lower qU values than the energy of the conversion line. The second systematic effect originates from the detector. If two or more electrons hit the same pixel in a smaller time window than the resolution time of the detector, the electrons are counted as a single electron with an energy between $E \in [E_1, \sum_i E_i]$ with E_1 the impinging kinetic energy of one electron and $\sum_i E_i$ the sum of all electrons involved in the pile-up event. For this reason, one can observe a rather constant rate at energies higher than the M- and N-lines of the γ -32 keV transition. As pile-up events are more likely to happen for higher rates at the detector, this effect is more dominant for lower qU values. From this follows for the differential and the integral spectra, that electrons are not detected at their initial energy or at all, which can cause a distortion of the spectra. Moreover, Fig. 6.6 shows that the pile-up region of the K-line overlaps with the backscattering tail of the L-line, which impedes the data correction for these two systematic effects.

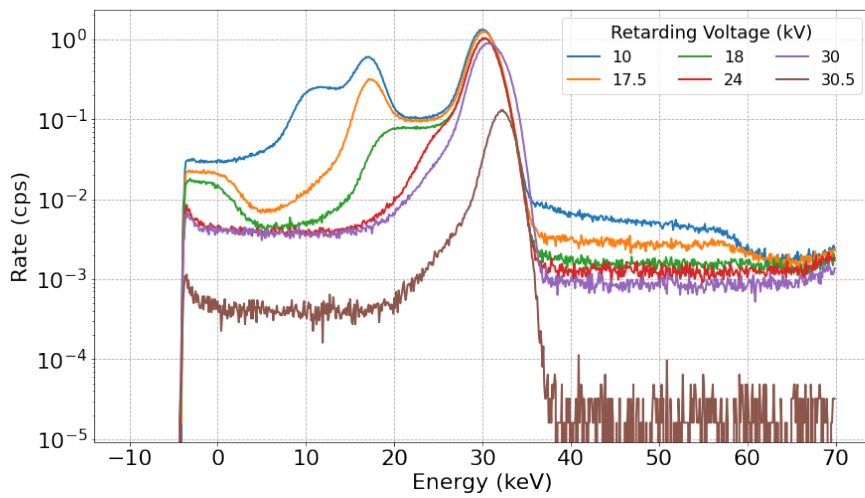


Figure 6.6: Differential spectra for the CKr source measurement for different qU values at the central position and $B_{MS} = 20$ G. Manly, two systematic effects are visible in the spectra; backscattering and pile-up at the detector. These effects result in a backscattering tail of the energy peaks towards lower energies and a rather constant plateau at energies higher than the conversion lines of the γ -32 keV transition.

6.3. Pile Up Estimation

One very important detector related effect is the pile up. When an electron hits detector wafer, it deposits charge in the wafer pixel. The deposited charge is processed by a charge-integrating preamplifier of the DAQ system. The step-like output with a rise-time of ~ 100 ns and a longer discharge time of 1 ms, is digitized and then processed by trapezoidal filters. In Fig.6.7 the working principle of these filters is illustrated. For a single electron event the step-like output of the charge preamplifier and the first trapezoidal filter is shown on the left. The trapezoidal filter consists of two integration windows of shaping length L (indicated by the blue and red bars in Fig.6.7) separated by a gap length G . Both, L and G are programmable and chosen to optimize the event reconstruction. The gap length of $G = 200$ ns is chosen to fully contain the rise-time. The height of the trapezoidal filter scales with the height of the step-like input and provides an energy estimation. In order to optimize the energy resolution of the wafers, the first trapezoidal filter has a shaping length of $L = 1.6 - 6.4$ μ s. If two or more electrons arrive at the same pixel within the shaping length, only one electron will be detected. This inaccurate electron counting is called pile up. In Fig.6.7 a pile up events of two electrons is shown on the right. Detailed information can be found in [66].

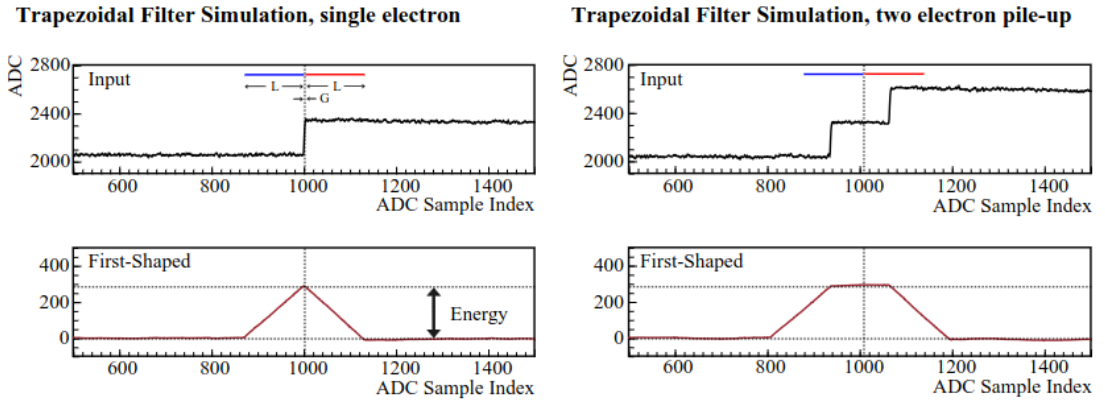


Figure 6.7: Illustration of the step-like output of the charge-integrating preamplifier and the first trapezoidal filter. On the left a single electron events is shown with the important adjustable parameters; the shaping length and gap length. On the right a pile up events consisting of two electrons is shown. This figure is taken from [66].

In KATRIN two approaches are commonly used to estimate the pile-up rate; the correction formula or the 2D pile-up map, which are explained in the following. Further, a very preliminary investigation has been conducted to see if the rate per pixel was high enough to be biased by pile-up events.

6.3.1. Correction Formula

The electron loss caused by pile up events can be corrected by an analytic correction formula. This formula was developed with a two-fold random coincidence model, where the electrons are assumed to arrive Poissonian random in time with the same energy [67]. This formula has been demonstrated to be valid for rates below 2 kcps,

$$\epsilon(R) = \left(1 - \frac{\alpha}{2}\right) \exp(-2WR) + \frac{\alpha}{2} [67] \quad (6.4)$$

with R the mean rate, $W = L + G + 26 \text{ ns}$ the event window length and the pile-up rejection ratio $\alpha = 0.215$. However, pixel rates ranging from 1.4 kcps to 18.3 kcps have been observed for the main pixel for the different measurements. Hence, this correction formula cannot be applied for the condensed krypton measurement, as the rates exceed the limit of validity and the K-32 and L-32 peaks are not well separated. Further, the rate per pixel not only depends on B_{MS} , the radial position of the source but also on the qU value. Hence, these effects are not expected to cancel completely when comparing the total detector rate between different settings for the same qU set point.

6.3.2. 2D Pile-Up Map

Another method to correct for the pile up is using a 2D cut based on the variables: Bipolar peak valley time and energy. The bipolar peak valley time is an unit to measure the time between the highest value of the accumulated charge and the full depletion for a semiconductor. As pile-up events resemble a different profile than single electron events, the events with different multiplicities, i.e. the number of electrons involved in the pile-up event, are in principle spatially separated in this plot.

$$\text{multiplicity} = \text{events}(\text{energy}, \text{BipolarPeakValleyTime}) \quad (6.5)$$

However, as shown in Fig. 6.8, this is not valid for the measurement with the CKr source. Due to the overlapping of the backscattering escape of the L-32 energy peak and the pile-up region of the K-32 peak, the characteristic regions are also overlapping in the 2D map and a clear distinction is not possible. Additionally a clear discrimination between a backscattering escape and a double backscattering is not possible.

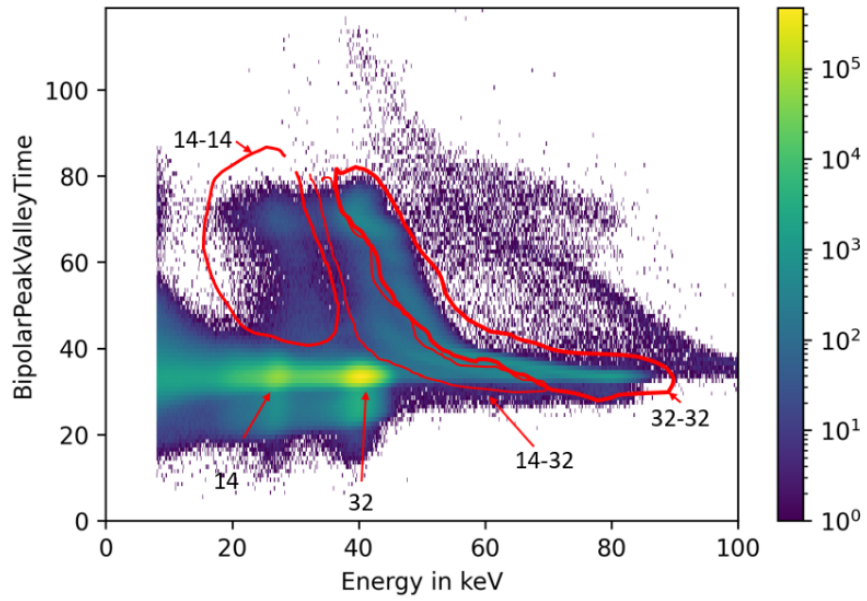


Figure 6.8: 2D pile-up map for the CKr measurement at $B_{MS} = 6$ G for the central source position. The energy is shifted by the value of the post acceleration electrode PAE $U_{PAE} = 10$ kV. The bipolar peak valley time is an unit to measure the time between highest value of the accumulated charge and the full depletion in a semiconductor material. As single electron events and pile-up events show different profiles, the multiplicity of the detected event can be determined via this method.

6.3.3. Monte Carlo Estimation

As the current available approaches for the pile-up correction are not applicable for the CKr measurement, a first order estimation has been conducted based on a Monte Carlo simulation. In the following a consciously slightly overestimating value for the event window $W = 6.6 \mu\text{s}$ [68] is assumed. Further, for this estimation only one pixel is considered. No additional detector systematic effects such as charge sharing and a pixel change for backscattered electrons are considered. For each impinging electron the electrons arriving within Δt smaller than the time window W , started by the initial electron, are counted. The probability for a pile-up event can be expressed mathematically by

$$P_{PU}(R) = \int_{\Delta t=0}^W R e^{-R\Delta t} d(\Delta t) = 1 - e^{-WR} \quad [68] \quad (6.6)$$

with R the rate in cps. In Fig. 6.9, the distribution of the time difference of two consecutive electrons per obtained multiplicity for an assumed rate $R = 10 \text{ kcps}$ and the event window W is shown. The correct detection of a single electron predominates pile-up events of two and three electrons together by approximately a factor 15.

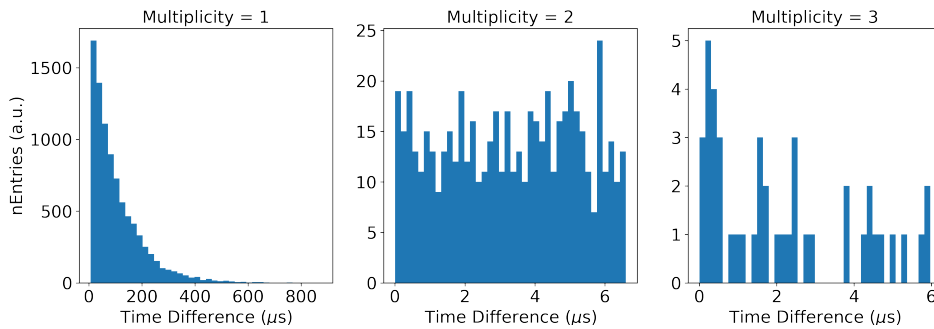


Figure 6.9: Distribution of the time difference between two consecutive electrons per obtained multiplicity for an assumed rate $R = 10 \text{ kcps}$ and event window $W = 6.6 \mu\text{s}$. The correct detection of a single electron predominates pile-up events by approximately a factor 15.

This simulation of 10.000 electrons arriving at the detector within one second was repeated 10.000 times. The average time difference obtained by these simulations is $\bar{t} = 99.99 \mu\text{s}$ and therefore much greater than W . Consequently, a single event is much more likely to happen, than a pile-up event of more electrons. The distribution of the average time difference is shown in Fig. 6.10.

The probability for each multiplicities from the MC simulation is shown in Fig. 6.11. As expected time distribution of the arriving electrons at the detector follows a Poisson distribution

$$P(X = k) = \frac{\lambda^k e^{-\lambda}}{k!} \quad (6.7)$$

with λ the mean value and k the number of occurrences. Here, the mean temporal distance for

6. Condensed 83m-Kr Measurement & Simulation

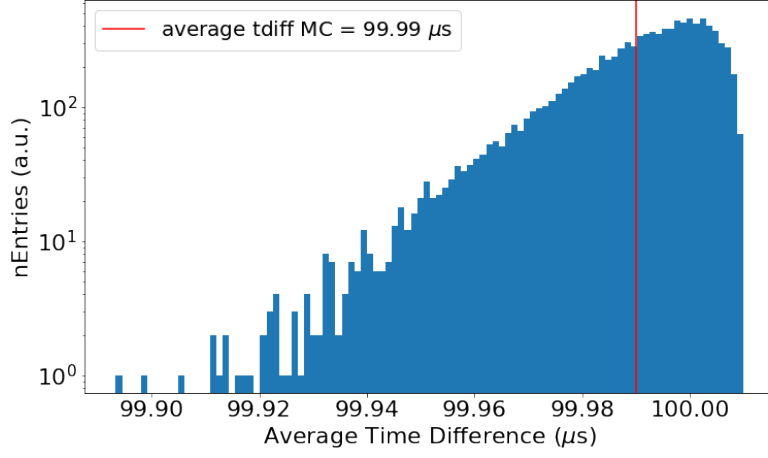


Figure 6.10: Distribution of the average time difference for 10.000 MC simulations for $R = 10$ kcps and $W = 6.6 \mu\text{s}$. The mean value is shown by the red vertical line. It shows that the average time difference is much greater than the assumed event window W . Consequently, the detection of a single electron predominated the occurrence of pile-up events.

the electrons, equals the product of the time window and the rate $\lambda = W \cdot R$. In Fig. 6.11 the Poisson distribution plotted by the black line. The obtained probabilities from the simulations match the predicted probabilities of the Poisson distribution.

As the first electron of each pile-up event is counted, the measured rate equals the sum of the number of occurrences of each multiplicity. Hence, one can find a relation between the measured rate and the true rate, i.e. the simulation input R . With a third order polynomial fit, the following relation was determined for a simulated rate at the detector of $R = 1, 2, 5, 7, 10, 12, 15, 18$ and 20 kcps and only one pixel

$$R_t = 5.69 \times 10^{-5} \cdot R_m^3 + 6.42 \times 10^{-3} \cdot R_m^2 + 1.00 \cdot R_m - 9.08 \times 10^{-4} \quad (6.8)$$

with R_t the true rate and R_m the measured rate. In Fig. 6.12 this relation is shown. The impact of pile-up on R_m for the different input rates R_t is shown in Fig. 6.13. As expected, the higher the rate at the detector, the more pile-up events occur. The preliminary estimation for the impact of pile-up shows that 0.65% of the electrons are not counted at the detector for $R_t = 1$ kcps. The impact of the pile-up rises significantly up to 11.66% for $R_t = 20$ kcps.

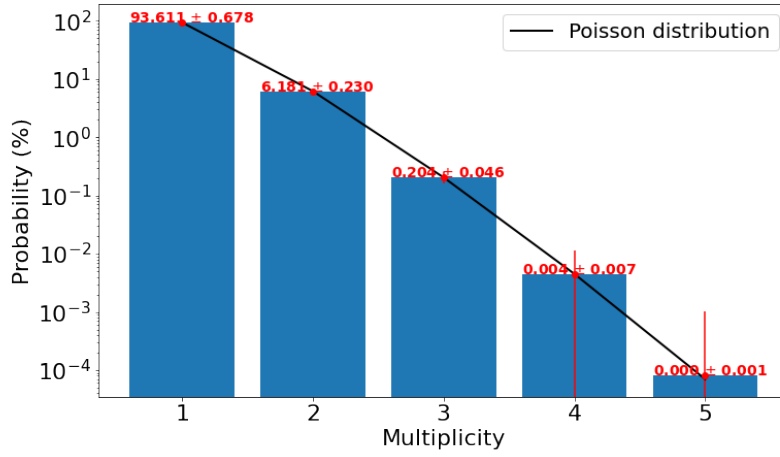


Figure 6.11: The probability and standard deviation for each multiplicity of the obtained multiplicities for 10.000 MC simulations for $R = 10$ kcps and $W = 6.6 \mu\text{s}$. The obtained probabilities from the simulations match the Poisson distribution, plotted by the black line, with the assumed mean value $\lambda = W \cdot R$.

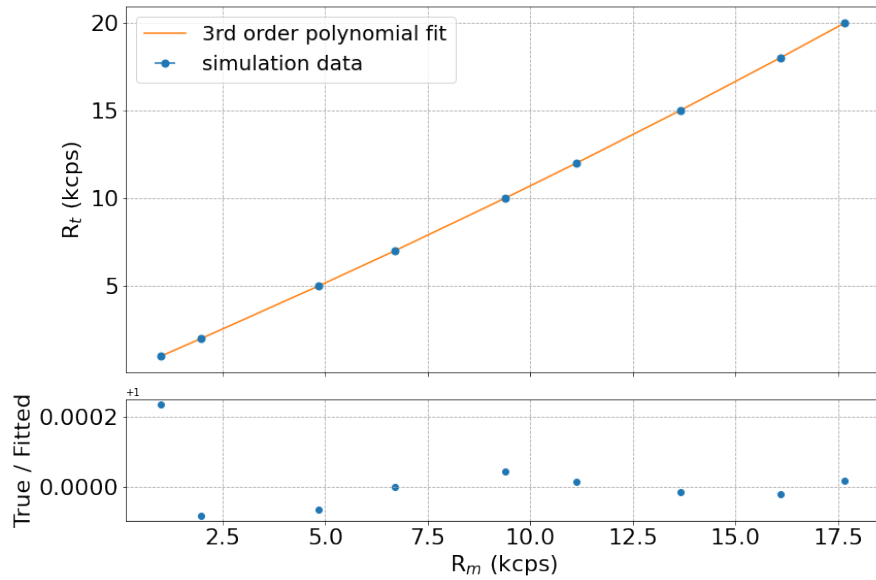


Figure 6.12: The true rate R_t at the detector as a function of the measured rate R_m in kcps. With a third order polynomial fit, the relation between the true and measured rate; $R_t = 5.69 \times 10^{-5} \cdot R_m^3 + 6.42 \times 10^{-3} \cdot R_m^2 + 1.00 \cdot R_m - 9.08 \times 10^{-4}$, was determined.

6. Condensed 83m-Kr Measurement & Simulation

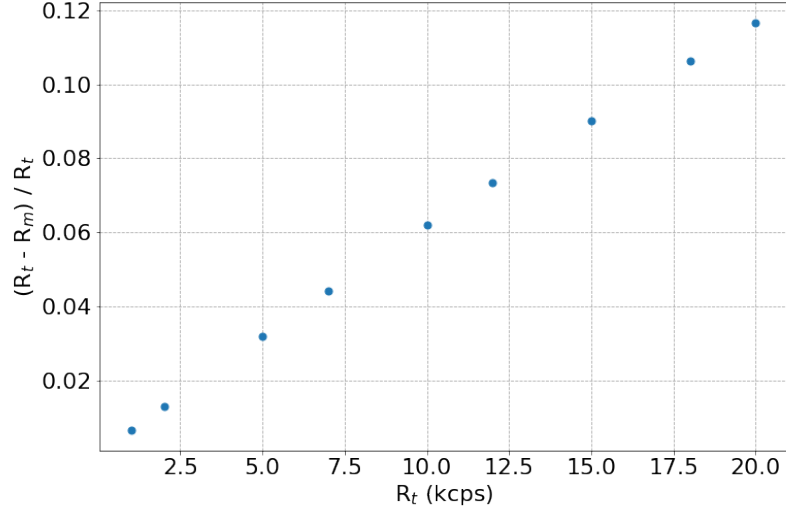


Figure 6.13: Electron loss caused by pile-up events as a function of the input rate R_t . It shows that the higher the rate at the detector, the more pile-up events occur and hence the more electrons are not counted at the detector. The preliminary estimation for the impact of pile-up shows that 0.65% of the electrons are not counted at the detector for $R_t = 1$ kcps. The impact of the pile-up rises significantly up to 11.66% for $R_t = 20$ kcps.

This first estimation for the impact of pile-up on the electron rate at the detector has shown, that especially for the points interesting for the study of non-adiabaticity, i.e. low qU value and hence a higher rate at the detector, a sophisticated pile-up correction is needed. The correction demands a precise model of the source and a method to distinguish pile-up from backscattering events. Further, all 148 pixels should be considered. When the energy and angular distribution of the electrons from inside the source to the MS and then to the detector can be described in detail, a pile-up model for the CKr source can be achieved with previous work conducted for the analysis of pile-up events.

6.4. Simulation with KASSIOPEIA

For the CKrS simulations conducted with KASSIOPEIA almost the same settings were used as for the transmission study, presented in Chapter 5. Only the source position in z - and y -direction and the magnetic field settings inside the MS were adjusted to match the conducted measurement. Further, every second qU set point was simulated with a total of 0.5×10^6 electrons for $B_{MS} = 6$ G and 20 G. The initial kinetic energy of the electrons is distributed according to the intensity of the conversion lines. The obtained integral spectra for all three source positions for $B_{MS} = 20$ G and $B_{MS} = 6$ G are shown in Fig. 6.14 and 6.15.

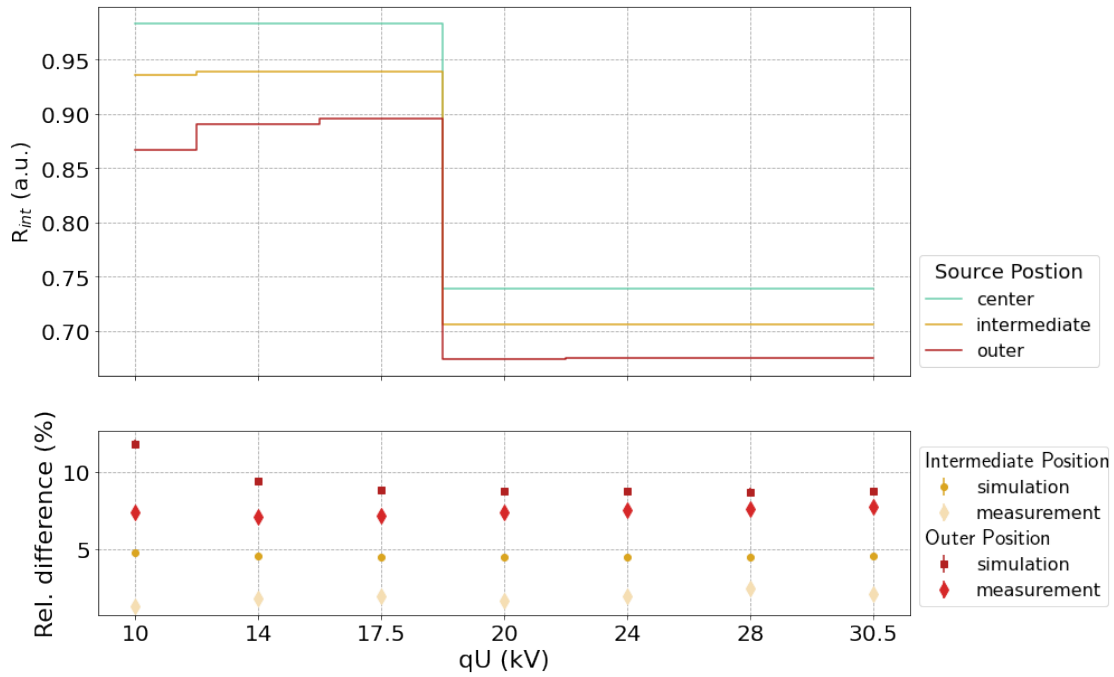


Figure 6.14: (Top) Simulated rate at the detector as a function of the retarding potential for three radial positions of the source for the max LFCS (20G) setting using KASSIOPEIA. (Bottom) The relative difference for the simulation and measurement for the 20G setting are shown. The simulated data shows an overestimation of the transmission loss.

6. Condensed 83m-Kr Measurement & Simulation

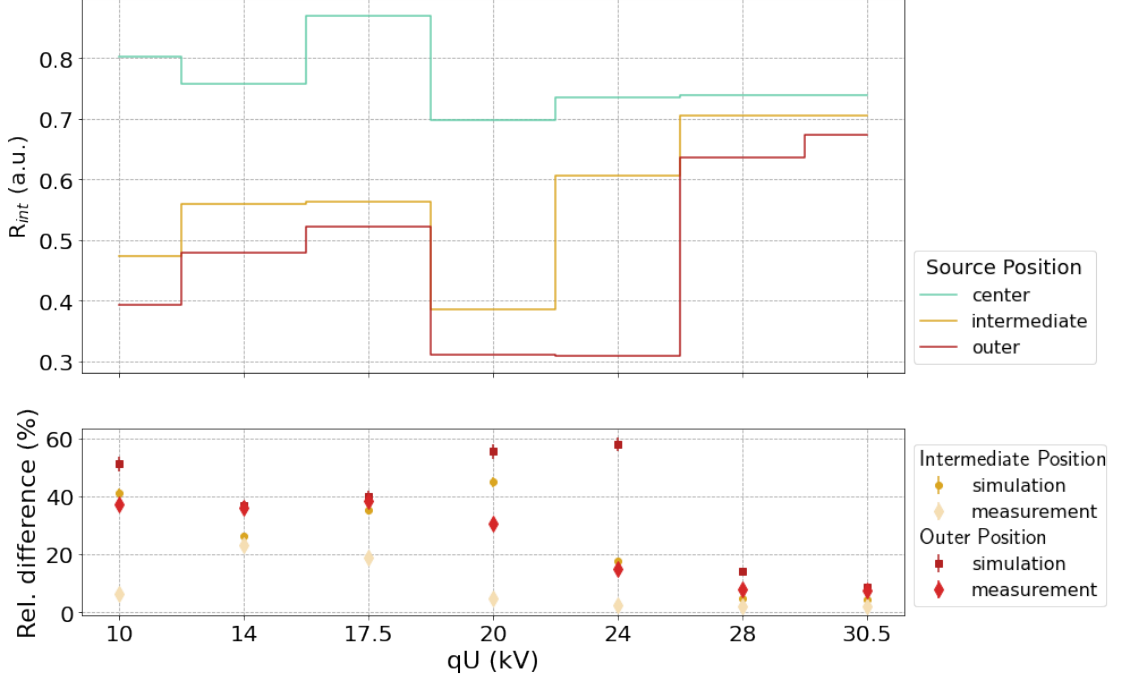


Figure 6.15: (Top) The simulated integral spectra for the three source positions; center, intermediate and outer position for the **6G** setting.

(Bottom) The relative differences for the simulation and measurement for the 6G setting are shown. Whereas for the most qU values the simulation is in good agreement with the measurement, there are some points with a very high discrepancy of up to 40 %.

For both MS magnetic field settings $B_{MS} = 6, 20$ G, the simulations show a higher transmission loss than the measured data. The greatest impact is believed to be the energy dispersal towards lower energies caused by source scattering processes. Because of the source scattering the energy surplus of the signal electrons is mitigated before entering the MS. For the simulation, the fixed energy from the mono-energetic conversion lines was considered. Further, no systematic effects were included in the simulations. For the measurement systematic effects are assumed to cancel by first order approximation used to calculate the electron loss. However, the investigated settings show different rates at the detector. Hence, the influence of the systematic effects are not the same. Mainly, these two effects; the energy dispersion due to source scattering processes and systematic effects at the detector, are assumed to cause the discrepancy between the simulated and measured data. Nevertheless, most qU points show for the measurement and simulation a decrease of transmission towards lower retarding voltages, i.e. high surplus energy. As for the measurement, the impact of high energy surplus on the electron transmission is more pronounced for electrons with a larger distance to the symmetry axis. Furthermore, also the simulations show that the MS magnetic field strength is a crucial factor for a good transmission.

Acknowledgments

First of all, I want to thank Prof. Susanne Mertens for the great possibility being part of her group. Without her knowledgeable and energizing compassion for physics together with her kind atmosphere, the work would never have been as wholesome and motivating for further interesting work in science.

I especially want to thank Ferenc Glück for all the help and time he has invested. Without all the discussions and comparisons of our simulations my work would have never been possible.

Further I want to thank

- my supervisor Anthony Onillon for his time and support.
- Anna Schubert and Florian Henkes for the motivational hugs and friendship.
- Xaver Stribl and Christian Forstner for the best atmosphere in the office.
- Matthias Meier for our nice journeys to TUM by bike.
- to the entire group for the warm atmosphere, discussions and coffee breaks.
- Brennan Hackett for her understanding and showing me a good example for being a great physicist and lovely person.
- Jan Behrens and Martin Descher for the introduction to *KASSIOPEIA* and some of their time.
- all the people at KIT and the *KATRIN* collaboration. It was always a very pleasant and instructive stay at the *KATRIN* site.
- all my friends that I am lucky to have.

Lastly, I want to thank my parents for the great support and love I have received throughout my entire life.

A. Appendix

A.1. Total Transmission Probability

TF	B _{det} (T)	Total P _{trans} (%)	Stat. Uncertainty (%)	Max E _{surplus} (keV)
1	2.52	99.469	0.0023	5.8
1	1.70	99.695	0.0017	6.8
1	1.00	99.826	0.0013	7.3
1	0.70	99.872	0.0011	7.9
1	0.50	99.901	0.0010	7.9
1.5	2.52	99.938	0.0008	8.8
1.5	1.70	99.968	0.0005	9.2
1.5	1.00	99.984	0.0004	11.4
1.5	0.70	99.989	0.0003	11.4
1.5	0.50	99.992	0.0002	11.9
2	2.52	99.991	0.0003	10.2
2	1.70	99.996	0.0002	11.4
2	1.00	99.998	0.0001	14.9
2	0.70	99.999	0.0001	15.4
2	0.50	99.99955	0.0001	17.4

Table A.1: Total transmission probability with the statistical uncertainty for each of the 15 settings after the cut on the initial polar angle was performed. For each setting 10×10^6 electrons were simulated. In order to correct for the dependence of the initial polar angle θ on the initial radial position, a cut was performed for the maximal allowed θ_{\max} . For $\theta \geq \theta_{\max}$ electrons are magnetically reflected at the pinch magnet. The table also includes the maximal allowed surplus energy to ensure complete electron transmission.

A.2. Slow Control Parameters

	Magnet	Current (A)	B (T)
	rscm_current	57.0	4.0
	wgts_current_M1M4M5	216.9	2.5
	wgts_current_M2M3	216.2	2.5
	wgts_current_M6M7	146.2	4.0
	dps_coil_1_current	56.8	4.0
	dps_coil_2_current	56.7	4.0
	dps_coil_3_current	56.7	4.0
	dps_coil_4_current	56.7	4.0
	dps_coil_5_current	56.9	4.0
	cps_coil_current	140.0	4.0
	ps_1_current	109.5	3.2
	ps_2_current	108.8	3.2
	pinch_magnet_current	60.9	4.2
	detector_magnet_current	39.3	2.52
	detector_magnet_current	26.5	1.7
	detector_magnet_current	15.6	1.0
	detector_magnet_current	10.92	0.7
	detector_magnet_current	7.8	0.5
	earth_magnetic_field_x	0.0	
	earth_magnetic_field_y	0.0	
	earth_magnetic_field_z	200.9e-7	

Table A.2: Values of the slow control parameters for the performed transmission study.

A.2. Slow Control Parameters

Coil Index	I_{\max} (A)		
	20G	8G	6G
1	120	100	50.8
2	120	45	0
3	120	41	44.6
4	120	33	45.4
5	100	33	24.6
6	100	35	37
7	100	49	14.7
8	100	53	52.8
9	100	53	34.9
10	100	52	38.7
11	100	53	9.2
12	100	50	35.9
13	120	52	92.7
14	120	60	13.2
15	120	60	0.0
16	120	60	0.0
17	120	0	0.0
18	120	0	0.0
19	120	-50	0.0
20	120	-110	0.0

Table A.3: Individual LFCS coil currents for the three magnetic field settings in the MS; 6G, 8G and 20G.

A.3. Polar Angle Correction - Cut Functions

TF	B_{det} (T)	a (deg/mm ²)	σ_a	b (deg/mm)	σ_b	c (deg)	σ_c	CF
1	2.52	1.917×10^{-4}	4.977×10^{-16}	-5.032×10^{-5}	8.451×10^{-13}	60.002	6.304×10^{-11}	0.9999968726224538
1	1.70	1.911×10^{-4}	2.301×10^{-16}	-2.808×10^{-5}	2.635×10^{-13}	60.089	1.325×10^{-11}	0.9999985687951463
1	1.00	1.906×10^{-4}	8.077×10^{-17}	-1.275×10^{-5}	5.440×10^{-14}	60.163	1.610×10^{-12}	0.9999995020353867
1	0.70	1.904×10^{-4}	3.987×10^{-17}	-7.496×10^{-6}	1.881×10^{-14}	60.194	3.900×10^{-13}	0.9999997550745934
1	0.50	1.903×10^{-4}	2.037×10^{-17}	-4.525×10^{-6}	6.859×10^{-15}	60.216	1.014×10^{-13}	0.9999998751459409
1.5	2.52	11.917×10^{-4}	4.975×10^{-16}	-5.032×10^{-5}	8.448×10^{-13}	60.001	6.301×10^{-11}	0.9999968730692567
1.5	1.70	1.911×10^{-4}	2.301×10^{-16}	-2.807×10^{-5}	2.634×10^{-13}	60.087	1.325×10^{-11}	0.999998568983527
1.5	1.00	1.906×10^{-4}	8.074×10^{-17}	-1.275×10^{-5}	5.438×10^{-14}	60.161	1.609×10^{-12}	0.9999995021003211
1.5	0.70	1.904×10^{-4}	3.986×10^{-17}	-7.495×10^{-6}	1.881×10^{-14}	60.193	3.899×10^{-13}	0.9999997551065128
1.5	0.50	1.903×10^{-4}	2.037×10^{-17}	-4.525×10^{-6}	6.857×10^{-15}	60.214	1.014×10^{-13}	0.9999998751622174
2	2.52	1.917×10^{-4}	4.974×10^{-16}	-5.031×10^{-5}	8.445×10^{-13}	59.999	6.300×10^{-11}	0.9999968734328215
2	1.70	1.911×10^{-4}	2.300×10^{-16}	-2.807×10^{-5}	2.633×10^{-13}	60.085	1.325×10^{-11}	0.9999985691596301
2	1.00	1.906×10^{-4}	8.072×10^{-17}	-1.275×10^{-5}	5.437×10^{-14}	60.159	1.609×10^{-12}	0.9999995021651324
2	0.70	1.904×10^{-4}	3.985×10^{-17}	-7.494×10^{-6}	1.880×10^{-14}	60.191	3.898×10^{-13}	0.9999997551384482
2	0.50	1.902×10^{-4}	2.036×10^{-17}	-4.524×10^{-6}	6.855×10^{-15}	60.212	1.014×10^{-13}	0.9999998751784996

Table A.4: Fit parameters and their statistical uncertainty for the maximal initial polar angle cut depending on the initial radial position for all studied magnetic field settings.

A.4. Run Numbers - CKrS Measurement

Position	Pixel	Source Displacement (mm)	B_{MS} (G)	Run Number
center	2	4	20	77811
			8	77812
			6	77810
intermediate	31	44	20	77760
			8	77761
			6	77759
outer	103	73	20	77757
			8	77758
			6	77756

Table A.5: Run numbers and source position for the CKrS measurement performed to investigate the non-adiabatic impact on the electron transmission.

Bibliography

- [1] Planck Collaboration. Planck 2018 results. vi.cosmological parameters. <https://arxiv.org/abs/1807.06209>, 2018.
- [2] ATLAS Collaboration. Observation of a new particle in the search for the standard model higgs boson with the atlas detector at the lhc. *arXiv:1207.7214*, 2012.
- [3] MissMJ and Cush. Pbs nova, fermilab, office of science, united states department of energy, particle data group. https://commons.wikimedia.org/wiki/File:Standard_Model_of_Elementary_Particles.svg. Accessed: 2023-04-20.
- [4] J.Chadwick. Intensitaetsverteilung im magnetischen spektrum der betastrahlen von radium $b + c$, 1914.
- [5] C.Cowan, F.Reines, F.Harrison, H.Kruse, McGuire, and A.D. Detection of the free neutrino: a confirmation. *Science*, 124, 1956.
- [6] G. Danby, J-M. Gaillard, K. Goulianos, L. M. Lederman, N. Mistry, M. Schwartz, and J. Steinberger. Observation of high-energy neutrino reactions and the existence of two kinds of neutrinos. *Phys. Rev. Lett.*, 9, 1962.
- [7] M.L. Perl et al. Evidence for anomalous lepton production in $e^+ - e^-$ annihilation. *Phys. Rev. Lett.*, 35, 1975.
- [8] K.Kodama. Observation of tau neutrino interactions. *Physics Letter B.*, 504, 2001.
- [9] ALEPH Collaboration, DELPHI Collaboration, L3 Collaboration, OPAL Collaboration, SLD Collaboration, LEP Electroweak Working Group, and heavy flavor groups SLD electroweak. Precision electroweak measurements on the z resonance. *arXiv:hep-ex/0509008v3*, 2006.
- [10] S.Gariazzo, P.F. de Salas, and S.Pastor. Thermalization of sterile neutrinos in the early universe in the 3+1 scheme with full mixing matrix. *arXiv:1905.11290 [astro-ph.CO]*, 2019.
- [11] K.Akita and M.Yamaguchi. A review of neutrino decoupling from the early universe to the current universe. *arXiv:2210.10307v2*, 2022.
- [12] J.Froustey et al. Neutrino decoupling including flavour oscillations and primordial nucleosynthesis. *JCAP*, 12, 2020.

Bibliography

- [13] R.Davis. A review of the homestake solar neutrino experiment. *Progress in Particle and Nuclear Physics*, 32, 1994.
- [14] W.Hampel et al. Gallex solar neutrino observations: Results for gallex iv, 1999.
- [15] J.Abdurashitov et al. Measurement of the solar neutrino capture rate with gallium metal. iii: Results for the 2002–2007 data-taking period. *Phys. Rev. C*, 80, 2009.
- [16] Inverse beta processes and nonconservation of lepton charge. *Zh. Eksp. Teor. Fiz.*, 1957.
- [17] S.Sakata et al. Remarks on the unified model of elementary particles. *Progress of Theoretical Physics*, 49, 1973.
- [18] Q. R. Ahmas. Direct evidence for neutrino flavor transformation from neutral-current interactions in the sudbury neutrino observatory. *Phys. Rev. Lett.*, 89, 2002.
- [19] Y. Fukuda et al. Evidence for oscillation of atmospheric neutrinos. *Phys. Rev. Lett.*, 81, 1998.
- [20] J.N.Bahall et al. New solar opacities, abundances, helioseismology, and neutrino fluxes, 2005.
- [21] P.F.de Salas et al. Status of neutrino oscillations 2018: 3σ hint for normal mass ordering and improved cp sensitivity. *Phys. Rev. Lett.*, 782, 2018.
- [22] P.A. Zyla et al. (Particle Data Group). Neutrino masses, mixing, and oscillations. *Prog. Theor. Exp. Phys.*, 2020.
- [23] M.Drewes et al. A white paper on kev sterile neutrino dark matter. *JCAP*, 01, 2017.
- [24] C.Forstner. Characterization of a TRISTAN Silicon Drift Detector Array with a Laser System.
- [25] R.L.Workman et al. (Particle Data Group). Review of Particle Physics, 2022. 083C01.
- [26] KATRIN Collaboration. Direct neutrino-mass measurement with sub-electronvolt sensitivity. *Nat. Phys.*, 18, 2022.
- [27] S.Dell’Oro, S.Marocci, M.Viel, and F.Vissani. Neutrinoless double beta decay: 2015 review. *Advances in High Energy Physics*, 2016, 2016.
- [28] Final results of gerda on the search for neutrinoless double- β decay. *Phys. Rev. Lett.*, 125:252502, 2020.
- [29] LEGEND Collaboration. The large enriched germanium experiment for neutrinoless double beta decay (legend). *AIP Conference Proceedings*, 1894, 2017.
- [30] M.Goldhaber et al. Helicity of neutrinos. *Phys. Rev.*, 109, 1958.

- [31] T.Asaka, S.Blanchet, and M.Shaposhnikov. The numsm, dark matter and neutrino masses. *arXiv:hep-ph/0503065*, 2005.
- [32] K. N. Abazajian et al. Light sterile neutrinos: A white paper. 2012.
- [33] S.Palomares-Ruiz, S.Pascoli, and T.Schwetz. Explaining lsnd by a decaying sterile neutrino. *JHEP0509*, 048, 2005.
- [34] V.V.Barinov et al. Search for electron-neutrino transitions to sterile states in the best experiment. *Phys. Rev. C*, 105:065502, 2022.
- [35] M.Aker et al. Improved ev-scale sterile-neutrino constraints from the second katrin measurement campaign. *Phys. Rev. D*, 105:072004, 2022.
- [36] E.Bulbul, M.Markevitch, A.Foster, R.K.Smith, M.Loewenstein, and S.W. Randall. Detection of an unidentified emission line in the stacked x-ray spectrum of galaxy clusters. *The Astrophysical Journal*, 789(1):13, 2014.
- [37] F Bezrukov. ν msm and its experimental tests. *Journal of Physics: Conference Series*, 110(8):082002, 2008.
- [38] S.Mertens. Analysis of first tritium data of the katrin experiment. 2018.
- [39] M.Aker et al. First operation of the katrin experiment with tritium. *Eur.Phys.J. C*, 2019.
- [40] KATRIN Collaboration. Katrin design report 2021, 2021.
- [41] M.Babutzka et al. *New Journal of Physics*, 14, 2012.
- [42] A.Jansen. The cryogenic pumping section of the katrin experiment - design studies and experiments for the commissioning. 2015.
- [43] C.Karl. First sub-electronvolt direct neutrino mass measurement with the katrin experiment.
- [44] F.Fraenkle. Penning discharge in the katrin pre-spectrometer. *JINST*, 9, 2014.
- [45] F.Glück, G.Drexlin, B.Leiber, S.Mertens, A.Osipowicz, J.Reich, and N.Wandkowsky. Electromagnetic design of the katrin large-volume air coil system. *New Journal of Physics*, 15(8):083025, 2013.
- [46] A.Huber. Analysis of the first katrin data and searches for kev-scale sterile neutrinos.
- [47] J.Schwarz. The detector system of the katrin experiment - implementation and first measurements with the spectrometer, 2014.
- [48] J.F.Amsbaugh et al. Focal-plane detector system for the katrin experiment. *Nucl. Instrum. Meth.*, 778, 2015.

Bibliography

- [49] S.Mertens et al. Sensitivity of next-generation tritium beta-decay experiments for kev-scale sterile neutrinos. *Journal of Cosmology and Astroparticle Physics*, 2015, 2015.
- [50] A.Onillon. Neutrino mass measurement and sterile neutrinos search with the katrin experiment.
- [51] S.Mertens et al. A novel detector system for katrin to search for kev-sterile neutrinos. *J. Phys. G: Nucl. Part. Phys.*, 46, 2019.
- [52] TRISTAN group. Conceptual design report: Katrin with tristan modules.
- [53] P.Lechner et al. Silicon drift detectors for high resolution room temperature x-ray spectroscopy. *Nuclear Instruments and Methods in Physics Research*, A 377, 1996.
- [54] F.Edzards, D.Siegmann, K.Urban, and S.Mertens. Understanding and characterization of silicon drift detectors for applications in astroparticle physics. *FOPRA-Versuch 109*.
- [55] S Mertens et al. Characterization of silicon drift detectors with electrons for the tristan project. *Journal of Physics G: Nuclear and Particle Physics*, 48(1):015008, 2021.
- [56] The tristan experiment.
- [57] Ferenc Glück, Guido Drexlin, Benjamin Leiber, Susanne Mertens, Alexander Osipowicz, Jan Reich, and Nancy Wandkowsky. Electromagnetic design of the large-volume air coil system of the katrin experiment. *New Journal of Physics*, 15(8):083025, aug 2013.
- [58] F.Glück. Axisymmetric magnetic field calculation with zonal harmonic expansion. *Progress in Electromagnetics Research B*, 32, 2011.
- [59] J.Behrens. Kassiopeia: A modern, extensible c++ particle tracking package. *arXiv:1612.00262*, 2006.
- [60] M. Kleesiek, J. Behrens, G. Drexlin, K. Eitel, M. Erhard, J. A. Formaggio, F. Glück, S. Groh, M. Hötzel, S. Mertens, A. W. P. Poon, C. Weinheimer, and K. Valerius. beta-decay spectrum, response function and statistical model for neutrino mass measurements with the katrin experiment. *arXiv:1806.00369*, 2018.
- [61] T.Ullrich and Z.Xu. Treatment of erros in efficiency calculations. *arXiv:physics/0701199*, 2007.
- [62] J.W.Liu. Total cross section for high-energy electron scattering by h2, 1987.
- [63] M.Prall. Background reduction of the katrin spectrometers, 2011.
- [64] M.Slezak. Monitoring of the energy scale in the katrin neutrino experiment, 2015.
- [65] D.Vénos et al. Properties of 83m-kr conversion electrons and their use in the katrin experiment.

- [66] KATRIN Collaboration. The design, construction, and commissioning of the KATRIN experiment. *Journal of Instrumentation*, 16(08):T08015, 2021.
- [67] Sanshiro Enomoto. Fpd systematics model for knm4. 2021.
- [68] Sanshiro Enomoto. Detector count corrections for first tritium. 2019.

List of Figures

1.1.	Illustration of the Standard Model of Particles.	2
1.2.	The measured hadron production cross-section around the Z-resonance.	6
1.3.	Representation of the solar neutrino flux as a function of energy.	8
1.4.	Illustration of the mass distribution for the fermion masses.	11
1.6.	The current parameter space of a sterile neutrino with exclusions from various experiments.	17
2.1.	Illustration of the impact of a massive neutrino on the differential β -electron spectrum close to the endpoint.	20
2.2.	Illustration of the full KATRIN beamline.	21
2.3.	Illustration of the working principle of the MAC-E filter.	23
2.4.	Schematic view of the upgraded KATRIN main spectrometer and the air coil system.	26
2.5.	Schematic depiction of the focal plane detector (FPD) of the KATRIN experiment.	27
2.6.	Measured count rate for each retarding potential for the first two KATRIN measurement campaigns KNM1 and KNM2 and the results for the neutrino mass of past experiments and the KATRIN experiment.	28
2.7.	Tritium decay spectrum without and with the presence of a sterile neutrino with a mass of $m_4 = 10$ keV and an unphysical large mixing angle.	30
3.1.	Sensitivity of KATRIN equipped with TRISTAN modules to the sterile neutrino parameter space.	32
3.2.	Schematic drawing of a SDD TRISTAN detector cell.	34
4.1.	Depiction of the parameters for the zonal harmonic expansion.	38
4.2.	The two computation modes for the particle tracking.	40
4.3.	Schematic depiction of the constituents for a simulated run.	41
5.2.	Simulated transmission probability for electrons of $E = 0 - 20$ keV with the KATRIN 70% beamline setting together with the current maximal LFCS setting.	46
5.3.	Statistical uncertainty in relation to the total number of electrons for different transmission probabilities.	47
5.4.	The total number of electrons required to achieve a statistical uncertainty for a specific transmission probability.	47
5.5.	The exact (left) and approximated (right) orbital magnetic moment of an electron.	49

List of Figures

5.6. Increase of the polar angle versus the magnetic field strength for different initial polar angles.	49
5.7. Illustration of the relation between the magnetic field strength and the step size controlled via the cyclotron radius.	50
5.8. Illustration of the position distribution of the electrons along the x-y axis for a small survey of 0.5 million electrons.	52
5.9. Illustration of the source distribution radial-angular plane for the 70 % KATRIN beamline setting together with the max LFCS configuration and 10 million electrons.	53
5.10. Depiction of four different electron paths inside the MS.	54
5.11. Total length distribution for transmitted and reflected electrons for the 70% KATRIN beamline setting together with the max LFCS configuration.	55
5.12. Inelastic scattering probability for electrons with residual gas atoms inside the MS.	56
5.14. Computation time per electron for ZH 2 and ZH 3 for each of the four scenarios.	60
5.15. Maximal initial radii for the different detector magnetic field settings considered.	61
5.16. This figure shows the determination of the radial dependence of the magnetic field strength and the resulting cut function for $\theta_{max}(r)$ for the simulated electrons for the reference KATRIN setting, i.e. 70 % beamline setting together with the max LFCS setting.	62
5.17. Visible fluxtube radius inside the MS for different detector magnetic field settings.	63
5.18. KASSIOPEIA simulation showing the magnetic field strength along the z-axis inside and close to the MS for different turnfactors of the LFCS coil current.	65
5.19. Transmission probability for each of the three initial parameters for the reference setting.	68
5.21. Transmission probability as a function of the initial kinetic energy for different magnetic field settings at the detector for the maximum LFCS setting (TF=1).	71
5.23. Transmission probability as a function of the initial kinetic energy of the electrons for different magnetic field strength inside the MS for the nominal detector magnetic field strength.	73
5.24. Transmission probability as a function of the initial kinetic energy for different magnetic field settings inside the MS and for the nominal detector magnetic field strength.	74
5.25. Depiction of the fluxtube area at the source for constant $B_{det} = 2.52$ T and different scaling factors of the magnetic field strength inside the MS.	75
5.26. Transmission probability as a function of the initial kinetic energy for the studied values of B_{det} for TF = 1.5.	76
5.27. Transmission probability as a function of the initial kinetic energy for the studied values of B_{det} for TF = 2.	77
5.29. Maximum surplus energy of electrons inside the MS for a full transmission for all studied settings.	79

6.1. Decay scheme of 83-Rb into stable ^{83}Kr	82
6.2. The differential and integral energy spectra for the $^{83\text{m}}\text{Kr}$ γ -32 keV electron conversion lines, assuming no systematic effects.	83
6.3. For each position of the source at $B_{\text{MS}} = 20$ G, the FPD map and the total counts per pixel are shown.	87
6.4. Integral spectra for the CKrS measurement for the three studied radial source positions.	88
6.5. Integral spectra for the CKrS measurement for the three studied magnetic field settings inside the MS.	89
6.6. Differential spectra for the CKr source measurement for different qU values at the central position and 20G.	91
6.7. Illustration of the step-like output of the charge-integrating preamplifier and the first trapezoidal filter.	92
6.8. 2D pile-up map for the CKr measurement at $B_{\text{MS}} = 6$ G for the central source position.	94
6.9. Distribution of the time difference between two consecutive electrons per obtained multiplicity for an assumed rate $R = 10$ kcps and event window $W = 6.6$ μs	95
6.10. Distribution of the average time difference for 10.000 MC simulations for $R = 10$ kcps and $W = 6.6$ μs	96
6.11. The probability and standard deviation for each multiplicity of the obtained multiplicities for 10.000 MC simulations for $R = 10$ kcps and $W = 6.6$ μs	97
6.12. The true rate R_t at the detector as a function of the measured rate R_m in kcps.	97
6.13. Electron loss caused by pile-up events as a function of the input rate R_t	98
6.15. Integral spectra for the three source positions at the MS 6G setting for the simulated condensed krypton source.	100

List of Tables

5.1. Summary of the important initial simulation parameters for the studied scenarios.	51
5.2. Different source radial parameters and their distribution for the four scenarios. . .	57
5.3. Transmission probability with the statistical uncertainty in percent for ZH 1, ZH 2 and ZH 3 for all four scenarios.	59
6.1. Properties for the γ -32 keV conversion lines.	83
A.1. Total transmission probability with the statistical uncertainty for each of the 15 settings after the cut on the initial polar angle was performed.	103
A.2. Values of the slow control parameters for the performed transmission study. . . .	104
A.3. Individual LFCS coil currents for the three magnetic field settings in the MS. . .	105
A.4. Fit parameters and their statistical uncertainty for the maximal initial polar angle cut depending on the initial radial position for all studied magnetic field settings.	106
A.5. Run numbers and source position for the CKrS measurement performed to inves- tigate the non-adiabatic impact on the electron transmission.	107